Dottorato di Ricerca in Scienze Ambientali:

tutela e gestione delle risorse naturali

XVII ciclo

Numerical predictions of the Adriatic Sea circulations
and its coastal areas regimes

Presentata dal

Dott. Paolo Oddo

Centro Interdipartimentale di Ricerca per le Scienze Ambientali

Università degli Studi di Bologna

Ravenna

Tutore
Prof. Nadia Pinardi

Cordinatore
Prof. Carlo Ferrari

Tutore aggiunto
Dr. Marco Zavatarelli

Acknowledgements

There are a number of people who have contributed to this thesis. I am grateful to my advisor Prof. Nadia Pinardi. She introduced me to the subject of ocean numerical models. I enjoyed learning from her. Dr. Marco Zavatarelli has my sincere thanks for his continuous effort and collaboration.

I enjoyed working with the members of the SiNCEM lab. In particular the essential help of Dott. Luca Giacomelli for his every day friendship is greatly acknowledged.

I am also pleased to acknowledge the useful scientific collaborations with Prof. A. Robinson, Dr. Pierre F. J. Lermusiaux, Dr. Patrick J. Haley, Mr. Wayne G. Leslie and the entire Prof. Robinson group at the Harvard University.

This work was partially funded by the Italian Ministry for the Environment and Territory (Adricosm project) through the University of Bologna, Centro Interdipartimentale per le Ricerhce di Scienze Ambientali, Ravenna. We would like also to thank the MAT and the ADRICOSM projects and the NATO SACLANT Undersea Research Centre for making available data.

Contents

List of Figures……………………………………………………………..vii

List of Tables…………………...……………………………………..xv

Chapter 1

Introduction……………………..…………………………………...1

Chapter 2

A Numerical Study of the Interannual Variability of the Adriatic Sea (2000-2002)…………………………………………..5

2.1 Introduction ……………………………………………..………..5

2.2 Model design……………………………………………...............8

2.2.1 Surface and lateral boundary conditions………………………………..10

2.2.2 Simulation experiments design ……………………………………….12

2.3 Model simulations…………………………………………………13

2.3.1 Diagnosed surface fluxes……………………………………………….14

2.3.2 The structure of the circulation in the different years………………….17

2.3.3 Comparison between observations and model results …………………26

2.4 Discussion and Conclusions…………………………………..…33

Chapter 3

The Adriatic Basin Forecasting System…………………...……37

3.1 Introduction……………………………………………………………...37

3.2 Methodology and system description……………………………40

3.3 Po runoff sensitivity studies…………………………………..…42

3.4 Analysis of hindcast quality and forecast accuracy…………….45

3.4.1 Hindcast quality……………………………………………………….….45

3.4.2 Forecast accuracy………………………………………………….....51

3.5 Conclusions…………………………………………………………….53

Chapter 4

Lateral Open Boundary Conditions for Nested Limited Area Model: Process selective approach……………...……..57

4.1 Introduction…………………………………………………..……….57

4.2 The lateral boundary condition formalism……………...……..59

4.**2.1 Relaxation**……………………………………………………………………59

4.2.2 Advective conditions……………………………………………...…60

4.2.3 Radiation Conditions……………………………………………….….61

4.2.4 Mass conservation equation: the Flather condition…………………..…63

4.2.5 The scale selective lateral boundary condition………………………..…64

4.2.6 A special case: Rigid lid-free surface nesting (tested)………………..…68

4.3 Model configuration for lateral boundary conditions nesting.69

4.4 Experiments design……………………………………………...…71

4.5 Results and discussion…………………………………………………73

4.7 Summary and Conclusions……………………………………...83

Chapter 5

Interannual variability hindcast experiments of the Adriatic Sea circulation (2000-2002)……………………...…..85

5.1 Introduction……………………………………………………..….85

5.2 Methodology…………………………………………………………...87

5.3 Results and Discussion…………………………………..………88

5.3.1 Comparison between model results and observations…………………96

5.4 Summary and Conclusions………………………………...……99

Chapter 6

A High Resolution Multi-Model Comparison Study: The Northern Adriatic Sea Experiment………………….………..103

6.1 Introduction……………………………………………………….103

6.2 Methodology……………………………………………………….105

6.2.1 Models……………………………………………...…………….105

6.2.2 Experiments set-up…………………………………………………107

6.3 Results and Discussion…………………………………...……..109

6.4 Summary and Conclusions……………………………….………119

Bibliography……………………………………………………....121

List of Figures

Fig. 2.1 Bathymetry of the Adriatic Sea. The sub-basins studied in the paper are defined. The location of the MAT transects are also indicated (letters A and C in the northern sub-basin). Depths are given in meters. ......…………………6

Fig. 2.2 AREG and OGCM models domains. The horizontal resolution of both grids is undersampled. ……………………………………………………12

Fig. 2.3 Time series of the Po river runoff (m^3/s) for the model simulation period (2000-2002). …………………………………………………………………14

Fig. 2.4 Temporal evolution of the basin averaged (a) total heat fluxes ($W\ m^{-2}$), (b) wind stress curl ($dynes\ cm^{-3}$) for the model simulation period (2000-2002). ………………………...………………………………………………15

Fig. 2.5 Temporal evolution of the basin and surface averaged scalar proprieties (solid lines) and the corresponding anomaly (dash lines). A) Mean volume temperature (°C). B) Mean surface temperature (°C). C) Mean volume salinity (psu). D) Mean surface salinity (psu). …………………………………….17

Fig. 2.6 Near surface (2m depth) temperature (°C) and velocity (m/s) fields for: (a) winter 2000; (b) winter 2001; (c) winter 2002. …………………………….19

Fig. 2.7 Near surface (2m depth) temperature (°C) and velocity (m/s) fields for: (a) summer 2000; (b) summer 2001; (c) summer 2002. …………………….20

Fig. 2.8 Temporal evolution of the total amount of waters having sigma-theta >29.2 $kg\ m^{-3}$ in the three sub-basins (m^3). …………………………………….22

Fig. 2.9 Meridional transport stream function (Sv) winter mean for: (a) year 2000; (b) year 2001; (c) year 2002. ………………………………………………….25

Fig. 2.10 Vertical temperature distributions (°C) along the transect A for the simulated winters. (A-B-C) 2000, 2001 and 2002 winters means from observations. (D-E-F) 2000, 2001 and 2002 winters means from model results. The position of the transect is reported in Figure 2.1. …………………….28

Fig. 2.11 Vertical salinity distributions (psu) along the transect A for the simulated winters. (A – B - C) 2000, 2001 and 2002 winters means from observations. (D - E- F) 2000, 2001 and 2002 winters means from model results. ……………………………………………………………29

Fig. 2.12 Differences between climatological salinity (Artegiani *et al*. 1897 a, b) and MAT project data along the transects A and C. **A** winter 2000, **B** winter 2001, **C** winter 2002, along transect A. **D** winter 2000, **E** winter 2001, **F** winter 2002, along transect C. ………………………………………………………30

Fig. 2.13 Vertical temperature distributions (°C) along the transect C for the simulated springs. (A-B-C) 2000, 2001 and 2002 springs means from observations. (D-E-F) 2000, 2001 and 2002 springs means from model results. The position of the transect is reported in Figure 2.1. …………………….31

Fig. 2.14 Vertical temperature distributions (°C) along the transect C for the simulated summers. (A-B-C) 2000, 2001 and 2002 summers means from observations. (D-E-F) 2000, 2001 and 2002 summers means from model results. ……………………………………………………………32

Fig. 2.15 Vertical temperature distributions (°C) along the transect A for the 2000 and 2001 autumns. (A-B) 2000 and 2001 autumns means from observations. (C-D) 2000 and 2001 autumns means from model results. …………………….33

Fig. 2.16 February 2001 monthly mean near surface (5m depth) temperature (°C) from (a) ADRIA01 observations and (b) model results. …………………….34

Fig. 3.1 The Adriatic Sea coastal and bottom morphology. The figure shows also the locations of the river mouths discharging into the basin, the islands retained in the AREG model geometry, the track of the VOS XBT observational program and the location of its open boundary (AREG O.B.). Redrawn with modifications from Zavatarelli and Pinardi, 2003). …………………………………………….39

Fig. 3.2 Time line of hindcast-forecast procedure. The arrows indicate the external data collected on Tuesday (J) and used for the model simulations. The analysis data span the period starting from noon of the previous Tuesday (J-7) to noon of the current Tuesday (J). The forecast data span the period from 6.00 p.m. of the current Tuesday (J) to Thursday of the next week. …………………………….42

Fig. 3.3 Example of Po runoff forecasts for the week from January 29th 2002 to February 5th 2002. The diamond indicates the last available Po data. In blue the observed runoff is reported. Green, Red and Yellow indicate the results of the different forecast methods tested**.** …………………………………………….43

Fig. 3.4: Time series of the RMS error computed between observed Po runoff values and different forecast methods. The variance of the Po runoff computed using 10 years of daily data is also given. In the legend the annual mean for each forecast method is given. ……………………………………………………44

Fig. 3.5 Seasonally averaged near surface (2m depth) velocity field. Winter from January to April; Spring May and June; Summer from July to October; Autumn November and December. The seasons definition was first proposed by Artegiani (1997 a,b). ……………………………………………………………………46

Fig. 3.6 A: 2003 annual cycle of the basin averaged SST. The dashed line indicates the model hindcast; the solid line, the mean of satellite SST observations. **B:** Time series of the basin averaged RMS difference computed using the observed SST. ………………………………………………….47

Fig. 3.7 Spatial distribution of the annually averaged hindcast RMS error computed using the (remotely) observed and hindcasted SST. Units are °C. ….49

Fig. 3.8 RMS error computed using the VOS XBT data collected along the track indicated in figure 3.1 and the corresponding hindcasted temperature. **A:** Vertically averaged RMS error. **B:** Seasonally averaged vertical profiles of RMS error. ……………………………………………………………………50

Fig. 3.9 Horizontal maps of near surface (2m depth) hindcasted, forecasted temperature and differences. The second, fourth and seventh days of the simulations are shown. ………………………………………………….52

Fig. 3.10 A: RMS time series between hindcasted, forecasted and persisted SST. **B:** RMS time series between hindcasted forecasted and persisted SSS. ……..53

Fig. 3.11 Horizontal map of the time averaged SST RMS error between hindcasted and forecasted SST. Units are °C. …………………………….54

Fig. 3.12 Horizontal map of the time averaged Sea Surface Salinity (SSS) RMS error between hindcasted and forecasted SSS. Units are PSU. ……………..55

Fig. 4.1 Schematic map of the Adriatic Sea circulation. The green line indicates the model southern boundary. The yellow lines indicate the permanent (with seasonally variability) circulation pattern. The red lines indicate the current directly affected by the lateral boundary conditions implementation. ……..71

Fig. 4.2 Vertical profiles of RMS error and XBT cruises tracks are given. Each upper subplots show the vertical profiles of RMS error for the different sampling date. Red lines indicate Exp1, dark lines indicate Exp2 and blue lines indicate the Exp3. The lower subplots show the position of the sampling for each cruise. ...74

Fig. 4.3 Schematic layout of the maps reported in Fig.4.4 Fig.4.5 Fig.4.6 and Fig.4.8. Panels A B and C barotropic velocity for the Exp1 Exp2 and Exp3 respectively. Panels D E and F surface elevation field for Exp1 Exp2 Exp3 respectively. ……………………………………………………………………75

Fig. 4.4 Horizontal maps of barotropic velocity and surface elevation for the three experiments. The fields have been obtained averaging the model results from 4 to 6 April. ……………………………………………………………………77

Fig. 4.5 Horizontal maps of barotropic velocity and surface elevation for the three experiments. The fields have been obtained averaging the model results from 30 to 31 October. ………………………………………………………………78

Fig. 4.6 Horizontal maps of barotropic velocity and surface elevation for the three experiments. The fields have been obtained averaging the model results from 2 to 3 December. ……………………………………………………………………79

Fig. 4.7 Vertical profiles of RMS error and CTD sampling positions are given. The left panel shows the vertical profiles of temperature RMS error for the different experiments. The central panel shows the vertical profiles of salinity RMS error for the different experiments. The right panel shows the samplings positions. Blue lines indicate Exp1, red line indicate Exp2 and dark line indicate the Exp3. ……………………………………………………………………81

Fig. 4.8 Horizontal maps of barotropic velocity and surface elevation for the three experiments. The fields have been obtained averaging the model results from 5 to

6 February. ……………………………………………………………………82

Fig. 5.1 Space-Time diagram showing some physical processes. The rectangular areas indicate the scales resolved by the ocean circulation models (Red the Regional model, Green the Global Models). …………………………………….86

Fig. 5.2 Temporal evolution of the basin averaged (a) total heat fluxes (W m^{-2}), (b) wind stress curl (dynes cm^{-3}) for the model simulation period (2000-2002). The red line indicates the 5KAM results; the dark line indicates the 3KAM results. ……………………………………………………………………89

Fig. 5.3 Temporal evolution of the basin and surface averaged scalar proprieties. The dark line indicates the 3KAM results; the red line indicated the 5KAM results. A) Mean volume temperature (°C). B) Mean surface temperature (°C). C) Mean volume salinity (psu). D) Mean surface salinity (psu). ……………..90

Fig.5.4 3KAM near surface (2m depth) temperature (°C) and velocity (m/s) fields for: winter 2000 (A); winter 2001 (B); winter 2002 (C). …………………….91

Fig.5.5 3KAM near surface (2m depth) temperature (°C) and velocity (m/s) fields for: summer 2000 (A); summer 2001 (B); summer 2002 (C). ……………..92

Fig. 5.6 Temporal evolution of the total amount of waters having sigma-theta >29.2 kg m^{-3} in the three sub-basins (m^3). The dark lines indicate the 3KAM results; the red lines indicate the 5KAM results. …………………………….93

Fig. 5.7 3KAM meridional transport stream function (Sv) winter mean for: (a) year 2000; (b) year 2001; (c) year 2002. …………………………………….95

Fig. 5.8 Vertical temperature distributions (°C) along the transect A for the simulated winters. (A-B-C) 2000, 2001 and 2002 winters means from observations. (D-E-F) 2000, 2001 and 2002 winters means from 3KAM results. The position of the transect is reported in Figure 2.1. …………………….97

Fig. 5.9 Vertical salinity distributions (psu) along the transect A for the simulated winters. (A-B-C) 2000, 2001 and 2002 winters means from observations. (D-E-F) 2000, 2001 and 2002 winters means from 3KAM results. …………………….98

Fig. 5.10 Vertical temperature distributions (°C) along the transect A for the 2000 and 2001 autumns. (A-B) 2000 and 2001 autumns means from observations. (C-D) 2000 and 2001 autumns means from 3KAM results. …………………….99

Fig. 5.11 February 2001 monthly mean near surface (5m depth) temperature (°C) from 3KAM. ……………………………………………………………..100

Fig. 6.1 Model Domain and Bathymetry are shown. The depth is given in meters**.** ……………………………………………………………..108

Fig. 6.2 Time series of wind stress [dynes/cm^2] and Po River runoff [m^3/s]. ……………………………………………………………..110

Fig. 6.3 (A) Sea surface Temperature [°C] and velocity initialization fields. **(B)** **S**urface salinity [psu] initialization field. …………………………………...111

Fig. 6.4 Sea surface Temperature [°C] and velocity fields [m/s]. **(A)** HOPS day 10; **(B)** POM day 10; **(C)** HOPS day 20; **(D)** POM day 20; **(E)** HOPS day 25; **(F)** POM day 25. ……………………………………………………………..112

Fig. 6.5 Sea surface Salinity [psu]. **(A)** HOPS day 10; **(B)** POM day 10; **(C)** HOPS day 20; **(D)** POM day 20; **(E)** HOPS day 25; **(F)** POM day 25. ……114

Fig, 6.6 Temperature [°C] transects for the 1st, the 7th, and 23rd day of integrations.

In the abscissa the distance from the first station is reported in degree, the Y axis indicates the depth in meters. The first column indicates the observation; the second column indicated the HOPS results and in the third column the POM results are reported. The location of the transects are reported in the last column. ……………………………………………………………..116

Fig. 6.7 Salinity [psu] transects for the 3rd, the 13th, the 17th and 20th day of integrations. In the abscissa the distance from the first station is reported in degree, the Y axis indicates the depth in meters. The first column indicates the observation; the second column indicated the HOPS results and in the third column the POM results are reported. The location of the transects are reported in the last column. ………………………………………………………..117

Fig. 6.8 Daily averaged RMS error computed between models results and observation from CTD. The solid line indicates the POM model error, the dash line indicates the HOPS model error. In the x axis the days are reported, the y axis indicates the RMS error values. (A) RMS for temperature. (B) RMS error for salinity. ……………………………………………………………..118

List of Tables

Table.2.1 Heat flux (W/m^2) and its differences (%) with the climatology computed by Maggiore *et al.* (1998). The difference is defined as: [(model-climatology)/climatology]*100. Seasonal and annual means are reported. …...16

Table 2.2 Presence/Absence of dense waters (σ_θ > 29.20 kg m^3) in the MAT dataset used in this study. ……………………………………………………23

Table 2.3 Dates of the MAT samplings in the three years of the project (columns) sorted according to the seasons definition of Artegiani *et al.* (1997 a, b) (rows). ………………………………………………………………....27

Table 4.1 The boundary conditions set-up used in the three experiments. U and V indicate the barotropic velocity, u and v the total velocity and T and S indicate Temperature and Salinity respectively. ……………………………………73

Table 6.1 Basic equations for the HOPS model. Where r is the earth's radius, Ω the earth' rotation rate, ρ_0 is a constant density value, A_h , A_v the constant eddy viscosity coefficients, K_h , K_v the constant eddy diffusivity coefficients, δ the parameterization of convective adjustment and $\vec{u} = (u, v, w)$ the three dimensional velocity vector. …………………………………………………………..106

Chapter 1

Introduction

Ocean science requires accurate knowledge of the time space evolution of the characteristics of the marine environment. Field estimation in the ocean is complex and data sets are generally sparse compared to requirements. This is for mostly due to a large range of interacting space and time scales characterizing oceanic phenomena. The coastal ocean is particularly challenging because of multiple forcings, complex geometries, and boundary interactions.

From basic conservation laws and principles, fundamental marine science formulates dynamical models which approximate the dynamics of the sea. Numerical simulations and direct measurements are used to gain insight into it.

The development of specific regional predictive capabilities must take into account regional phenomena and the intended applications of the system.

The overall goal of this thesis is to develop an adequate instrument for the predictions and the study of the Adriatic Sea circulations and its coastal areas regimes. Since the Adriatic Sea is known to be a complex system with large spatial and time variability, it is a particularly challenging environment for the development of such instrument. The results arising from an Adriatic Sea modeling effort finalized to forecasting can be considered to have general validity.

The thesis is organized as follows.

In Chapter 2 after a description of the known characteristics of the Adriatic Sea, a detailed explanation of the numerical models used to predict and study the circulation of the basin is given. The results of the simulation are used to study the interannual variability of the Adriatic Sea taking into account several processes as sea-atmosphere exchanges, the general surface circulation, the dense water formation and the thermohaline circulation. The obtained knowledge on the interannual variability is also validated by mean of a comparison with available observations.

In Chapter 3 the operational Adriatic basin forecasting system is described. The numerical model used is based on the one described and used in the study of the interannual variability of the Adriatic Sea. One of the main issues in forecasting the whole Adriatic is related to the Po river runoff. Since no hydrological forecasts for this river are available we tested and evaluated the performance of several simple extrapolation techniques. The characteristic of operational system are described and the hindcast-forecast behavior evaluated using remote and in situ collected data.

In Chapter 4 we define and investigate the role of the open boundary conditions specification for a semi-enclosed basin. After an overview of the most commonly used solutions to the problem a new, process based, approach is proposed. The model described in Chapter2 has been used in order to validate the proposed approach. Three different set of open boundary conditions have been implemented: the simple imposition of the external data that can be considered the crudest approach; a simplified physic approach based on the wave equation that is considered to be the state of the art; the new proposed process selective approach. The performances of these possible solutions have been evaluated by mean of a comparison of the obtained results with available observations.

In Chapter 5 the sensitivity of the numerical model results to the horizontal resolution and to a reduced rivers runoff is investigated. The reasons for this experiment derive from the model deficiencies found comparing the results of the interannual simulation with observations. This study mitigates same of the model imperfections and improves the general model behavior; it is also helpful in understanding the lines for the future work.

The Last Chapter (Chapter 6) of this work is dedicated to the Northern Adriatic. The capabilities in reproducing North Adriatic Sea dynamics of two different models are evaluated and a first attempt at understanding the needed resources for an accurate reproduction of this sub-basin is performed.

Note that the Chapter 2 is a co-authored paper with Prof. N. Pinardi and Dr. M. Zavatarelli entitled “A Numerical Study of the Interannual Variability of the Adriatic Sea (2000-2002)” submitted and accepted for publication in “Science of the Total Environment” MAT special issue. Chapter 3 is a co-authored paper with Prof. N. Pinardi and Dr. M. Zavatarelli entitled “The Adriatic Basin Forecasting System” submitted to “Acta Adriatica” ADRICOSM special issue.

Chapter 2

A Numerical Study of the Interannual Variability of the Adriatic Sea (2000-2002)

Note that this Chapter is a co-authored paper with Prof. N. Pinardi and Dr. M. Zavatarelli entitled “A Numerical Study of the Interannual Variability of the Adriatic Sea (2000-2002)” submitted and accepted for publication in “Science of the Total Environment” MAT special issue.

2.1 Introduction

The semi-enclosed Adriatic Sea extends in a NNW-SSE direction for about 770 kilometers, and has a mean width of about 160 kilometers. The basin is conventionally divided, on the basis of its bottom morphology into three sub-basins: the northern, the middle and the southern (Fig. .2.1). The northern basin with an average depth of 35 m has truly coastal characteristics. The middle Adriatic has depths increasing from north to south and is marked by two bottom depressions reaching about 250 m in depth. The transition from the middle to the southern sub-basin occurs with a sharp bathymetry gradient from about 200 m to depths exceeding 1000 m. Exchanges with the Ionian Sea occur through the Otranto Channel, the morphology of which is marked by a sill of about 900 m in depth.

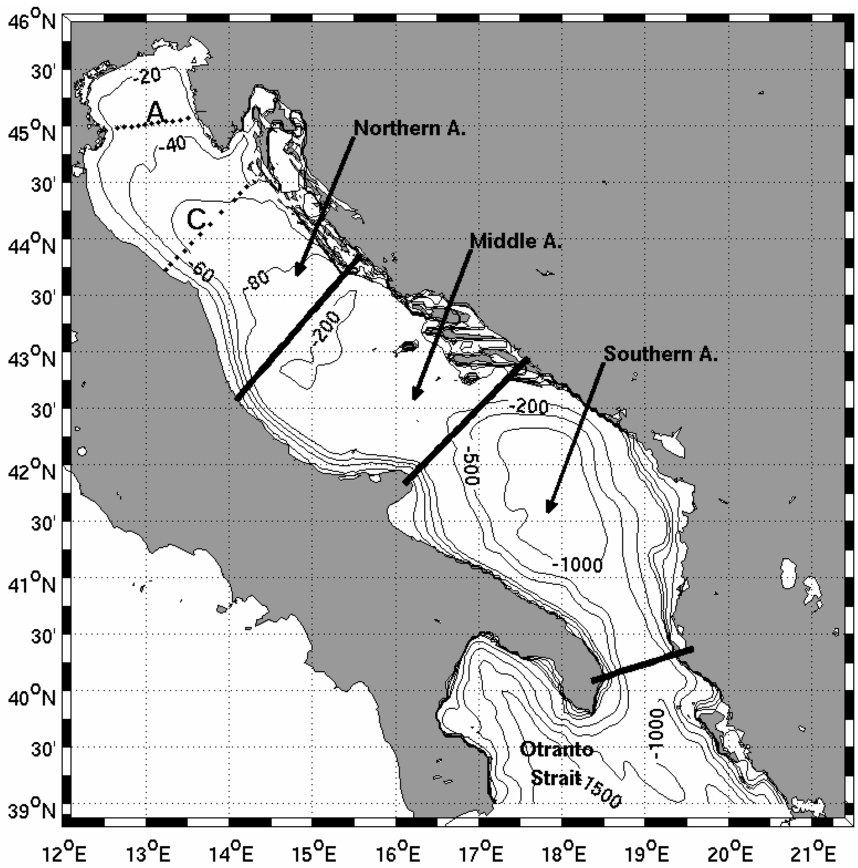

Figure 2.1 Bathymetry of the Adriatic Sea. The sub-basins studied in the paper are defined. The location of the MAT transects are also indicated (letters A and C in the northern sub-basin). Depths are given in meters.

The surrounding orography, basin morphology, atmospheric forcing, river runoff, and exchanges through the Otranto Channel constrain the Adriatic's general circulation. The two major wind regimes are the Bora (NNE) and the Scirocco (SE). The Bora blows over the Adriatic in intense episodic bursts. Its field over the Adriatic Sea is strongly influenced by the orography of the eastern Adriatic land margins (Vilibic, 2003), giving rise to a strong spatial variability (Orlic *et al.*, 1994). The Scirocco is connected with the passage of low pressure systems over the basin, causing the relative increase in sea level in this region due to the inverse barometer effect, and to the direct sea level set-up by the wind. This effect is particularly strong in the northern Adriatic (Orlic *et al*., 1992, Lascaratos and Gacic, 1990).

The river runoff is a significant component of the basin hydrological cycle and is responsible for the basin net fresh water gain (Raicich, 1994, 1996), implying an average estuarine thermohaline circulation. The freshwater discharge is particularly concentrated in the northern sub-basin, where the river Po constitutes the main freshwater source. However, in the southern basin, the ensemble of Albanian and Croatian rivers provides a significant fresh water input (Raicich, 1994).

The annual heat budget is negative at the climatological scale (-17, -22 Wm^{-2}, Artegiani *et al*., 1997a), but it is known to experience significant year-to-year variations sometimes being positive (Maggiore *et. al*., 1998, Cardin and Gacic, 2003, Chiggiato *et al*., this volume). The climatological negative heat budget implies the establishment of an antiestuarine thermohaline circulation, contrasting the effects of the freshwater flux. The basin is a well known site of dense water formation related to the winter surface heat losses, as well as to the ingression into the basin of Levantine Intermediate Water. Dense water formation processes occur in the northern shelf (Malanotte Rizzoli, 1991) and in the open Southern Adriatic (Ovchinnikov *et al*., 1987, Artegiani *et al*., 1989, Manca *et al*., 2002). The formation processes are known to be highly variable at the interannual time scales (Manca *et al*., 2002). The climatological circulation pattern is composed by well-known current and gyre structures (Artegiani *et al*., 1997b, Poulain, 2001, Zavatarelli *et al*., 2002, Zavatarelli and Pinardi, 2003), such as the three cyclonic gyres located in the southern, central and northern sub-basins, named respectively by Artegiani *et al.* (1997b) Southern (SAd), Middle (MAd) and Northern (NAd) Adriatic gyres. The three gyres are interconnected (with seasonally varying characteristics) by two coastal currents, one flowing southward along the whole western coast from the Po delta to the Otranto Strait (Western Adriatic Coastal Current or WACC), the other flowing northward from the Otranto Strait along the eastern coast and reaching the central Adriatic sub-basin (Eastern Southern

Adriatic Current or ESAC). However, the interannual variability of these circulation structures is still poorly known and understood.

This work starts to explore the Adriatic Sea circulation interannual variability connected to atmospheric forcing by means of numerical simulations of the general circulation. We concentrated on the period 2000-2002, during which the MAT project extensively monitored the northern and middle Adriatic Sea. The circulation is simulated by a three-dimensional model already used by Zavatarelli and Pinardi (2003) for climatological simulations of Adriatic Sea circulation. In order to reproduce the interannual variability, the model has been forced with atmospheric data obtained from the European Centre for Medium Range Weather Forecasts (ECMWF) analyses, daily Po discharges and lateral boundary conditions from a Mediterranean Sea general circulation model (Pinardi *et al.*, 2003). To our knowledge this is the first time that such an interannual variability simulation has been carried out and compared with data.

Section 2 gives a general description of the model implementation. Section 3 describes the model results and discusses the comparison with observed data. Conclusions are offered in the last section.

2.2 Model design

The numerical simulation of the Adriatic Sea general circulation has been carried out using the Adriatic Sea Regional Model (AREG) based on the Princeton Ocean Model, POM (Blumberg and Mellor, 1987) as implemented by Zavatarelli and Pinardi (2003). POM is a free surface, three-dimensional finite differences numerical model based on the primitive equations with Boussinesq and hydrostatic approximations. All the equations are written in rectangular coordinates and contain spatially and temporally varying horizontal eddy viscosity and diffusion coefficients. The model solves the following equations for the ocean velocity $U=(u, v, w)$, potential temperature θ and salinity S:

$$\nabla \cdot U = 0 \qquad \text{(eq. 2.1)}$$

$$\frac{\partial(u,v)}{\partial t}+U\cdot\nabla(u,v)+f(-v,u)=-\frac{1}{\rho_0}\left(\frac{\partial p}{\partial x},\frac{\partial p}{\partial y}\right)+\nabla_h\cdot\left[A_M\nabla(u,v)\right]+\frac{\partial}{\partial z}\left[K_M\frac{\partial(u,v)}{\partial z}\right] \quad \text{(eq. 2.2)}$$

$$\frac{\partial\theta}{\partial t}+U\cdot\nabla\theta=\nabla_h\cdot\left[A_M\nabla_h\theta\right]+\frac{\partial}{\partial z}\left[K_H\frac{\partial\theta}{\partial z}\right]+\frac{1}{\rho_0 C_P}\frac{\partial I}{\partial z} \quad \text{(eq. 2.3)}$$

$$\frac{\partial S}{\partial t}+U\cdot\nabla S=\nabla_h\cdot\left[A_M\nabla_h S\right]+\frac{\partial}{\partial z}\left[K_H\frac{\partial S}{\partial z}\right] \quad \text{(eq. 2.4)}$$

The eddy viscosity coefficient A_M is provided by the Smagorinsky (1993) parameterization implemented into POM according to Mellor and Blumberg (1985). The vertical mixing coefficients for momentum K_M and tracers K_H are calculated using the Mellor and Yamada (1982) turbulence closure scheme. The last term in (eq. 2.3) is the parameterization of the heat penetration in the water column (Pinardi *et al.*, 2003): ρ_0 is a reference density, Cp is the water specific heat and *I(z)* is defined according to:

$$I(z)=Tr\;Q_s e^{-\lambda z}$$

where Q_s is the short wave radiation flux and Tr and λ are the Jerlov (1976) transmission and absorption coefficients for which we adopted those corresponding to the "clear" water type.
Finally, the hydrostatic approximation yields,

$$\frac{\partial p}{\partial z}=-\rho(S,\theta,p)g \quad \text{(eq. 2.5)}$$

where ρ is the density calculated by an adaptation of the UNESCO equation of state devised by Mellor (1991).
AREG uses the Smolarkiewicz (1984) iterative positive definite advection scheme for tracers as implemented into POM by Sannino *et al*. (2002).

2.2.1 Surface and lateral boundary conditions

In order to parameterize the air-sea interaction processes, the wind stress, the heat fluxes and evaporation rate are computed by means of interactive bulk formulae making use of atmospheric data and the model predicted sea surface temperature. The resulting surface boundary conditions for momentum and tracers are:

$$\rho_0 K_M \frac{\partial(u,v)}{\partial z}\bigg|_{z=\eta} = \left(\tau_{wx}, \tau_{wy}\right) \quad \text{(eq. 2.6)}$$

$$\rho_0 K_H \frac{\partial\theta}{\partial z}\bigg|_{z=\eta} = \frac{1}{C_p}\left[(1-Tr)Q_S(C) - Q_B\left(T_a, \theta_{z=\eta}, C, rh\right) - Q_e\left(T_a, \theta_{z=\eta}, rh, \left|\overline{v_w}\right|\right) - Q_h\left(T_a, \theta_{z=\eta}, \left|\overline{v_w}\right|\right)\right]$$

(eq. 2.7)

$$K_H \frac{\partial S}{\partial z}\bigg|_{z=\eta} = S_{z=\eta}\left(E - P - R\right) \quad \text{(eq. 2.8)}$$

where η is the free surface elevation. The wind stress $\left(\tau_{wx}, \tau_{wy}\right)$ computation uses a drag coefficient computed according to Hellerman and Rosenstein (1983).

The surface boundary condition for temperature (eq. 2.7) involves the balance between surface solar radiation (Q_S), net long-wave radiation (Q_B), the latent and sensible heat fluxes (Q_e, Q_h). Solar radiation is dependent on cloud cover (*C*) and is computed by means of an astronomical formula (Reed 1975; 1977). The net long-wave radiation flux (May, 1986) is a function of air temperature (T_a), sea surface temperature ($\theta_{z=\eta}$), cloud cover C and relative humidity (rh). Sensible heat flux and latent heat flux are computed by classical bulk formulae parameterized according to Kondo (1975). Details on the bulk formulae used can be found in Maggiore *et al*. (1998) and Castellari *et al*. (1998).

Surface salinity flux in eq. 2.8 is given by the water balance E-P-R, where E is the evaporation (derived from the latent heat flux), P the precipitation and R the river-runoff multiplied by the model predicted surface salinity $S_{z=\eta}$ R is a non-zero value only at the “estuary” grid points.

POM traditionally uses only the kinematics vertical velocity boundary conditions, i.e.

$$w\big|_{z=\eta} = \left(\frac{\partial}{\partial t} + u\frac{\partial}{\partial x} + v\frac{\partial}{\partial y} \right)\eta$$

This means that in our model version the surface water flux does not produce volume changes but only salt changes.

Lateral open boundary conditions are defined through a simple off-line, one-way nesting technique. AREG is nested with the general circulation model of the Mediterranean Sea (OGCM) developed by Demirov and Pinardi (2002). In order to ensure that the volume transport across the open boundary of AREG matches the volume transport across the corresponding section of the OGCM, the total velocity component normal to the boundary was corrected on the basis of the differences between the volume transport computed on the AREG and on the OGCM grid (Pinardi *et al.*, 2003, Zavatarelli and Pinardi 2003). The vertically integrated velocity component normal to the boundary in AREG is defined as:

$$V_{AREG} = \left[\frac{H_{OGCM}}{(\eta + H_{AREG})} \right] V_{OGCM} \qquad \text{(eq. 2.9)}$$

where H_{OGCM} and H_{AREG} are the OGCM and AREG bottom depths along the open boundary, η is the AREG free surface elevation and V_{OGCM} is the OGCM vertically integrated velocity. Temperature and salinity on the outflow are locally resolved with an upwind scheme, while, if there is an inflow, they are prescribed from the OGCM. Differently from Zavatarelli and Pinardi (2003), in the AREG interior, immediately adjacent to the boundary, a nudging term was added (following Marchesiello *et al.*, 2001) to the right-hand side (r.h.s.) of the prognostic equations for tracers, as follows:

$$\frac{\partial \gamma}{\partial t} = r.h.s. - \frac{1}{\Gamma}\left(\gamma - \gamma^{OGCM}\right)$$

where γ can indicate temperature or salinity. Γ varies smoothly from few days at the boundary to (almost) infinity at a distance from the open boundary of approximately 50 km.

2.2.2 Simulation experiments design

AREG has been implemented on a regular horizontal grid with approximately 5 km resolution (the extension of the model domain is reported in Fig. 2.2) and 21 vertical sigma layers. The bathymetry has been obtained from U.S. Navy data (horizontal resolution: 1/60°), the minimum depth has been set to 10 m. The model has only one open boundary located south of the Otranto Channel where it is nested with the OGCM (Fig. 2.2).

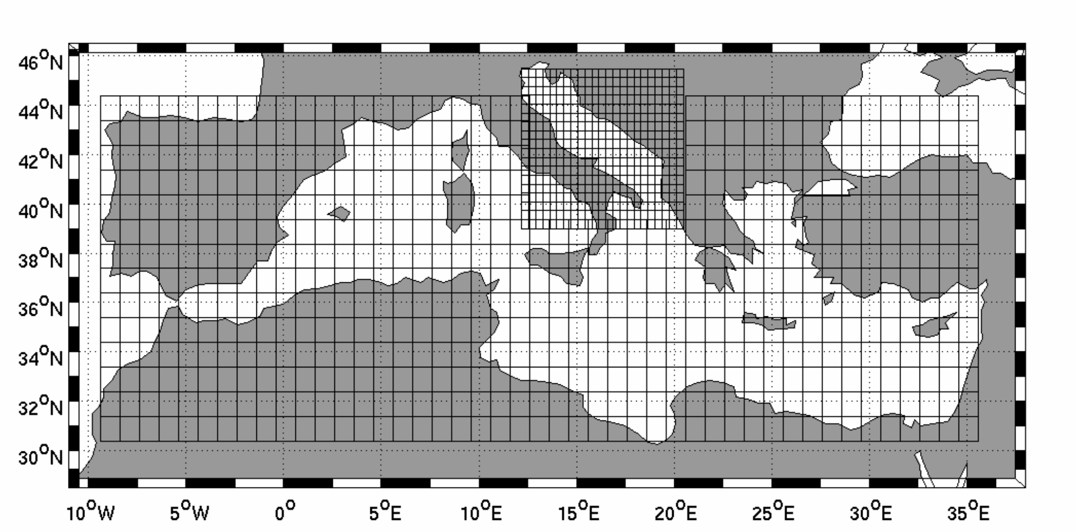

Figure 2.2 AREG and OGCM models domains. The horizontal resolution of both grids is undersampled.

Integration started at 00:00 on January 1st. As initial condition the fields from the climatological simulation of the Adriatic Sea circulation (Zavatarelli and Pinardi, 2003) were used. The atmospheric data for the computation of the surface forcing were obtained from the 6-hour, 0.5° horizontal resolution ECMWF surface analyses. The atmospheric fields used are air temperature, dew point temperature, wind velocity at 10m above sea level, mean sea level pressure and cloud cover. Precipitation data were obtained by interpolation of the 0.5° resolution Legates and Willmott (1990) climatological global, monthly averaged precipitation dataset into the model grid. The river runoff data for the major Adriatic Sea rivers, Po excluded, were obtained from the Raicich (1994) monthly climatology. The major Adriatic rivers were considered as point sources, while non point contributions were defined as an evenly distributed source along the pertinent portion of coastline. Po river runoff values are not climatological but we used the daily averages for the period 1999-2002 measured by the Po River Authority at the closing point of the drainage basin. The Po runoff is distributed over 6 grid points approximately representing the partitioning of the freshwater discharge through the mouths of the delta (Provini *et al*. 1992). The 2000-2002 time series of the Po river runoff is shown in Fig. 2.3. A large interannual variability is evident, marked mainly by three main events: a large maximum in autumn 2000, a sustained runoff for a large part of winter and spring 2001 and the absence of runoff maximum in autumn 2001.

2.3 Model simulations

In this section we describe the model simulation results for the period from January 2000 to December 2002. Results for year 1999 are not shown as the relative simulation is considered to represent the model spin up period.

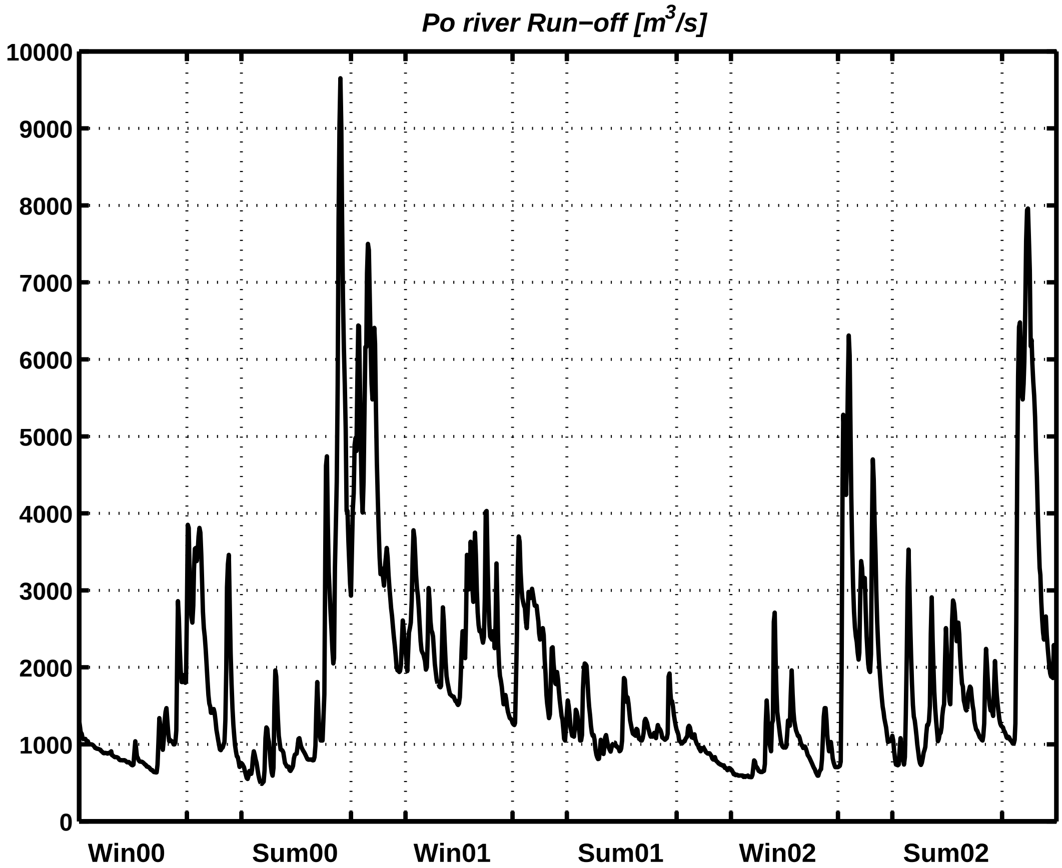

Figure 2.3 Time series of the Po river runoff (m3/s) for the model simulation period (2000-2002).

2.3.1 Diagnosed surface fluxes

Time series of the basin averaged daily mean heat flux and wind stress curl are shown in Fig. 2.4. The heat flux time series shows similar summer maximum values (about 200 W m^{-2}) and large differences in the minima (ranging from -380 W m^{-2} in autumn 2000 and 2002 to -600 W m^{-2} in 2001).

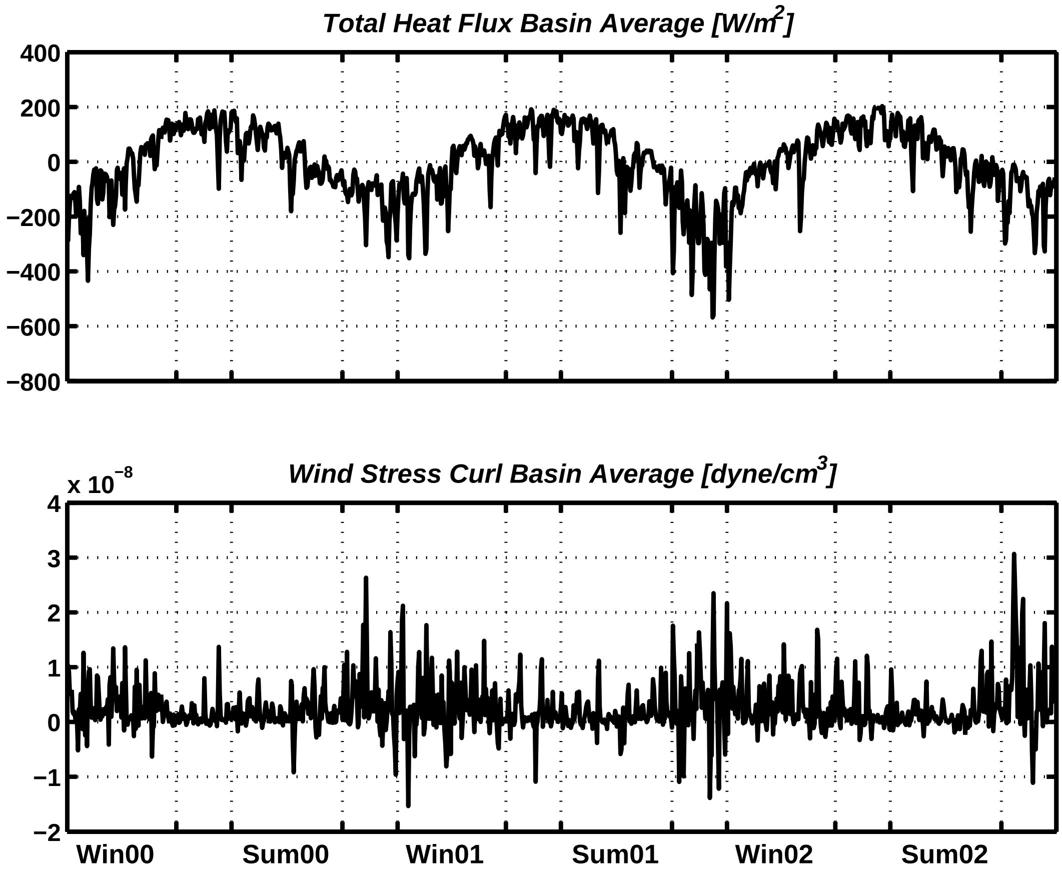

Figure 2.4 Temporal evolution of the basin averaged (a) total heat fluxes (W m^{-2}), (b) wind stress curl (dynes cm^{-3}) for the model simulation period (2000-2002).

The seasonally averaged heat fluxes are computed according to the season definition proposed by Artegiani *et al*. (1997 a): Winter; January to April, Spring; May and June, Summer; July to October, Autumn; November and December, and are reported in Table 2.1 along with the annual average and the anomalies (percentage values) from the climatology computed by Maggiore *et al*. (1998).

	Clim	2000	2000(%)	2001	2001(%)	2002	2002(%)
Winter	-75	-55	-26%	-40	-46%	-22	-70%
Spring	177	126	-28%	124	-29%	131	-25%
Summer	52	28	-46%	38	-26%	21	-59%
Autumn	-225	-132	-41%	-242	7%	-127	-43%
Annual	-17	-9	-47%	-18	5%	1	-105%

Table.2.1 Heat flux (W/m^2) and its differences (%) with the climatology computed by Maggiore *et al.* (1998). The difference is defined as: [(model-climatology)/climatology]*100. Seasonal and annual means are reported.

Previous computation of the climatological annual surface heat budget yielded values ranging between -17 and -22 W m^{-2} (Artegiani *et al.*, 1997a, Maggiore *et al.*, 1998; Cardin and Gacic, 2003). The annual average for year 2002 is instead weakly positive while the climatological value is met only in 2001. In general the spring-summer heat gain does not change significantly from year to year. On the contrary the autumn and winter cooling exhibits a strong interannual variability that is mainly due to the latent heat flux (not shown) component of the surface heat balance in eq. 2.7.

The time series of the basin averaged wind stress curl (Fig. 2.4) is predominantly positive, therefore implying a net cyclonic vorticity input into the basin with maxima in winter. The heat flux and the wind stress curl time series reveal a strong seasonal cycle, but the wind stress curl variability is clearly dominated by shorter time scale events determining the frequent change of the sign of the basin averaged wind stress curl. We know in fact that the wind stress curl spatial distribution is characterized by positive and negative lobes, due to the multiple jet structure of Bora winds (Orlic *et al.*, 1994). These short temporal and spatial scales are the main reason for the large interannual variability of Adriatic Sea circulation.

2.3.2 The structure of the circulation in the different years

In this section we analyze the model simulation and describe the interannual variability of Adriatic Sea circulation beginning with the analysis of the volume integrated scalar properties and ending with the comparison between model results and observations.

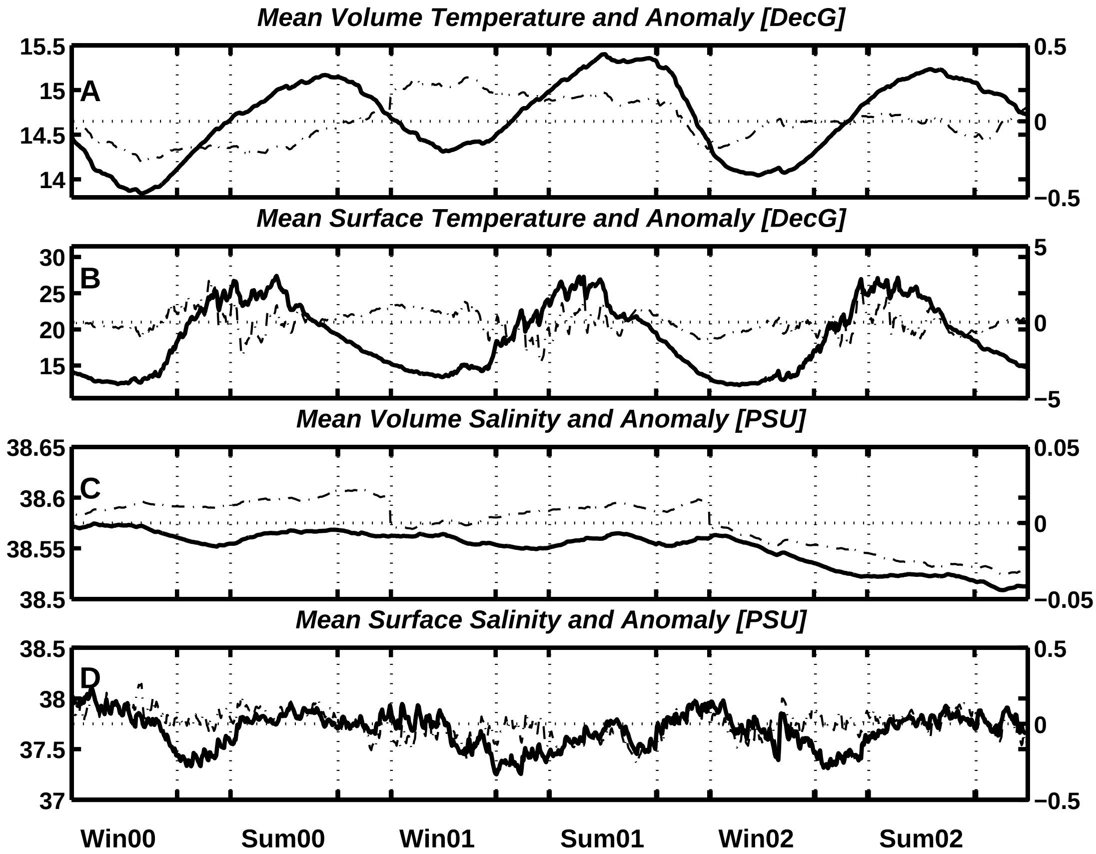

Figure 2.5 Temporal evolution of the basin and surface averaged scalar proprieties (solid lines) and the corresponding anomaly (dash lines). A) Mean volume temperature (°C). B) Mean surface temperature (°C). C) Mean volume salinity (psu). D) Mean surface salinity (psu).

The basin averaged temperature and the corresponding mean volume anomaly time series are shown in Fig. 2.5a and indicate a large interannual variability characterized by a maximum temperature value (15.50 ^{o}C) occurring in late summer 2001 and a minimum of about 13.80 °C in winter 2000. The former is probably a consequence of the mild autumn-winter 2000-2001 (confirmed also by the anomaly maximum occurring during winter 2001) and, similarly, the latter is influenced by the marked heat loss occurring during the winter 2000 (Fig. 2.4 and Table 2.1). The time series of the surface averaged temperature and its anomaly (Fig. 2.5b) show the same characteristics but with a less evident interannual signal during winter.

The basin averaged salinity (Fig. 2.5c) does not show the marked interannual variability affecting the temperature field, remaining approximately constant at 38.57 psu throughout almost the entire simulation. The only remarkable deviation can be noted for 2002, during which the basin undergoes a freshening of about 0.04 psu. Analysis of the salt flux through the model open boundary (not shown) seems to indicate that the freshening is due to a reduced salt flux into the basin rather than to a variation in the surface salt flux. In fact the time series of the surface averaged salinity (Fig. 2.5d) suggests an annual cycle for 2002 similar to that of previous years.

In Fig. 2.6 and 2.7 we show the winter and summer temperature and velocity near surface (2m depth) fields. A significant difference can be noted between 2001 (Fig. 2.6b) and both 2000 (Fig. 2.6a) and 2002 (Fig. 2.6c). The 2001 winter fields are characterized by a more energetic circulation pattern, with relatively high surface temperatures and a large and well defined MAd gyre. The larger kinetic energy of the circulation is evident in the stronger WACC and more intense MAd and SAd gyres. The reason for this increased strength of the circulation structures can be traced back to the relatively concurrent action of mild winter heat fluxes (Table 2.1), high Po runoff during winter-spring and strong wind stress curl over the basin (Fig. 2.4b). It is in fact known that large heat losses and thus cooler waters in the northern and western coastal areas contribute to a weaker WACC (Zavatarelli *et al.*, 2002); conversely the strong Po runoff and the large wind stress curl would enhance it. Under large positive wind stress curl conditions the MAd gyre is stronger as well as the SAd gyre and the ESAC.

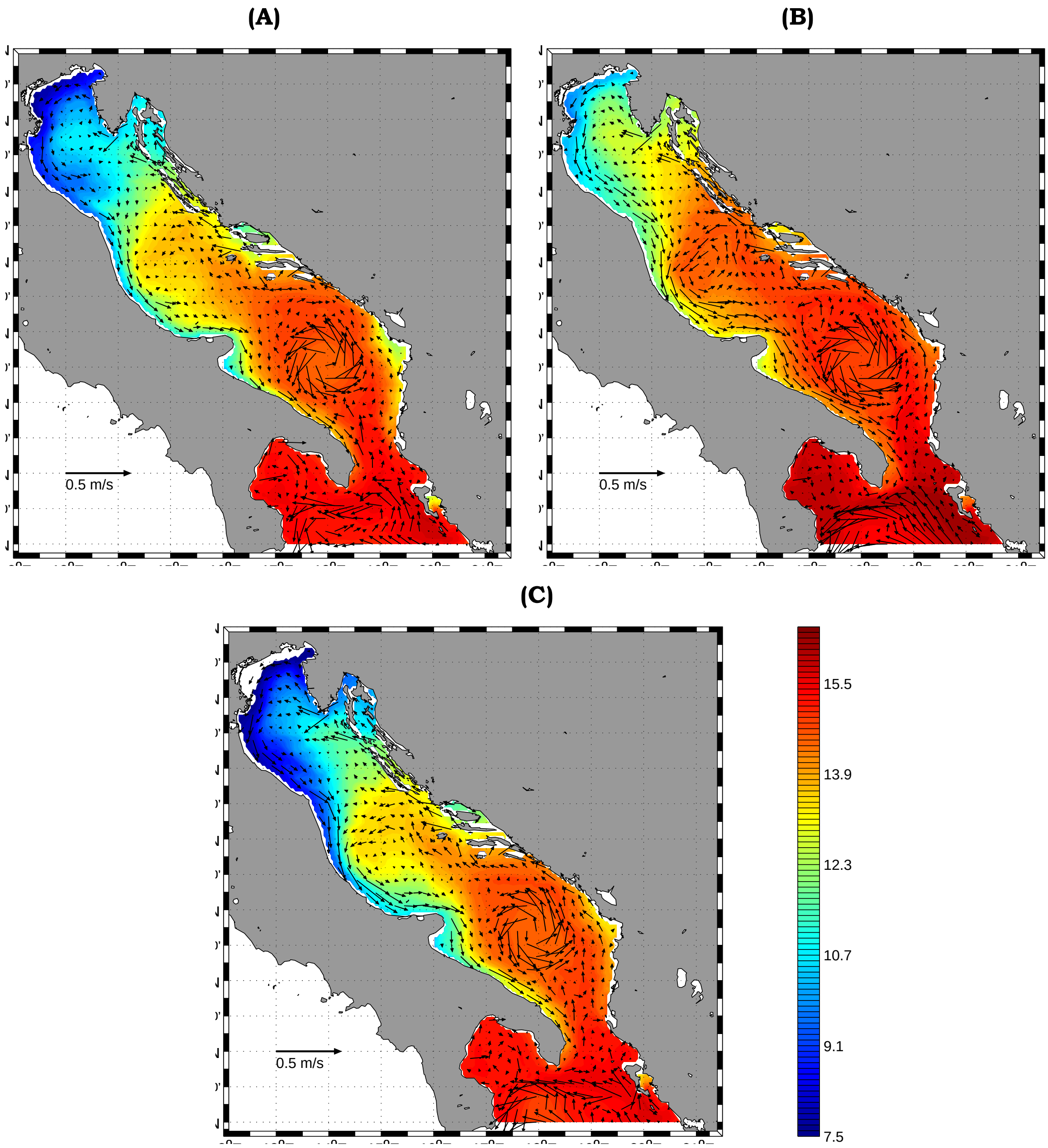

Figure 2.6 Near surface (2m depth) temperature (°C) and velocity (m/s) fields for: (a) winter 2000; (b) winter 2001; (c) winter 2002.

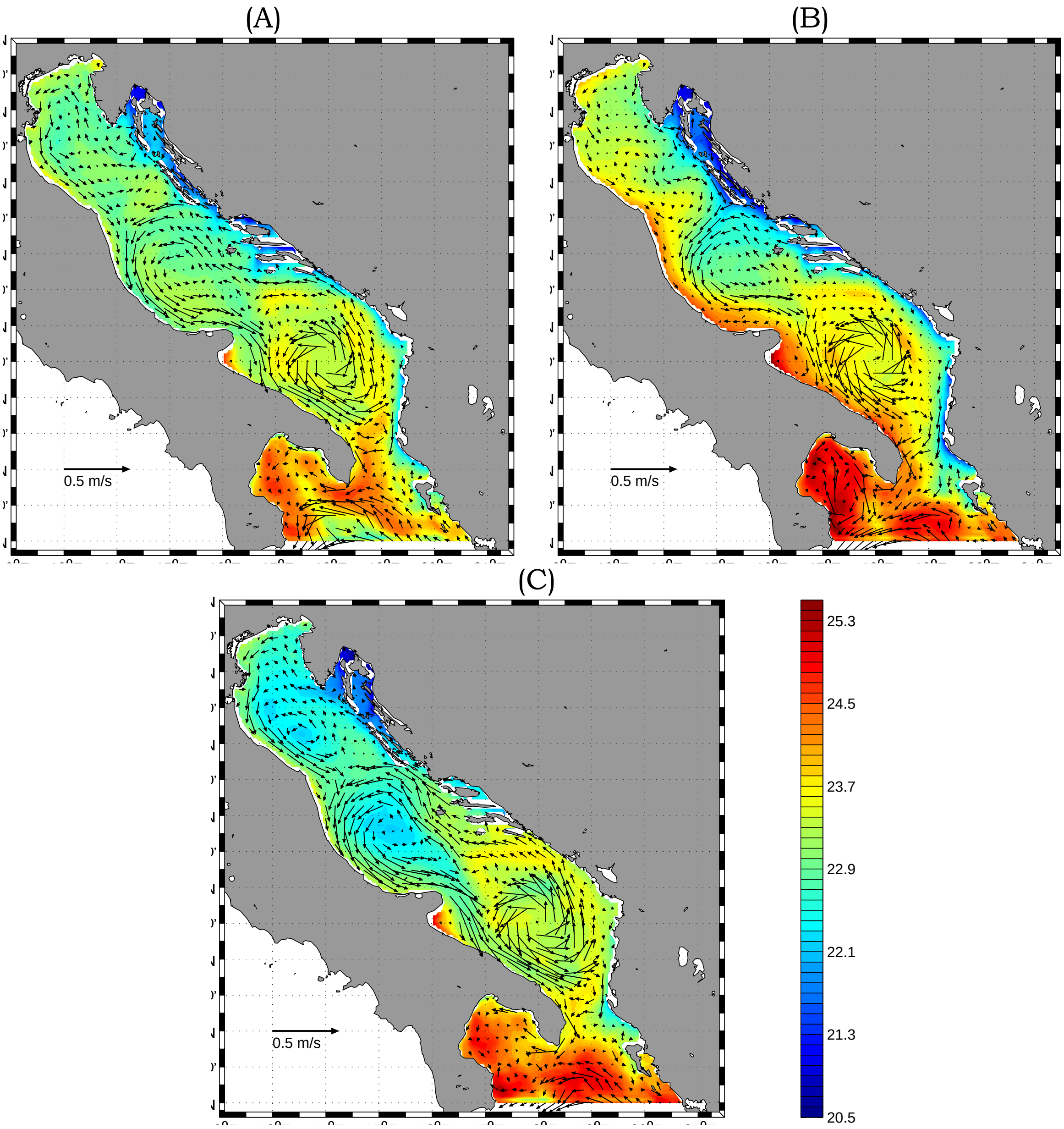

Figure 2.7 Near surface (2m depth) temperature (°C) and velocity (m/s) fields for: (a) summer 2000; (b) summer 2001; (c) summer 2002.

The cooler surface temperatures in the winter of 2000 and 2002 (Fig. 2.6a, c) are due to large heat losses in the winter of 2000 and autumn of 2001, therefore, the two similar surface temperature fields arise from different processes and forcings.

The three summers (Fig. 2.7a, b, and c) are characterized by well defined MAd and SAd gyres. The simulated cross shelf extension of the WACC is larger than in the winter, in agreement with observations (Poulain 2001). Differently from the winter fields (Fig. 2.6), the north-western shelves are characterized by warm temperatures on the westward side of the WACC due to downwelling motion. During winter the WACC transports cool waters formed in the northern Adriatic and the temperatures on the westward side of the WACC are at a minimum. During summer, coastal heating prevails and allows the downwelling regime to store heat.

Interesting differences in the circulation between the three summers are the position and intensity of the NAd gyre and the strong interannual variability of the circulation along the Istrian coast. The NAd gyre is evident in summer 2000 (Fig. 2.7a) and 2002 (Fig. 2.7c) although it is located farther to the south in 2002. On the contrary in summer 2001 (Fig. 2.7b) the NAd gyre almost disappears. Concurrent with the strong weakening of the gyre is the reversal of the coastal circulation along the Istrian peninsula. The appearance of a southward current in this region, named by Supic *et al*. (2000) the “Istrian Coastal Countercurrent, ICC”, has been already simulated at the climatological scale by Zavatarelli and Pinardi (2003). However, the appearance of the ICC only in 2001 seems to confirm the interannual nature of such circulation pattern as originally proposed by Supic *et al*. (2000). A small and weak ICC can be detected also in the summer of 2000 in the northernmost part of the Istrian peninsula. However, during 2001 the overall cyclonic circulation of the northern Adriatic is the weakest of the three years and the ICC develops more strongly. Our results show that it is very difficult to predict the changes in the circulation directly from the atmospheric and fresh water forcing variability since their concomitant effect is largely nonlinear in the Adriatic basin.

The variability of the dense water formation processes have been diagnosed from the model results by assessing the volume of water with σ_θ > 29.20 kg m^{-3} (in agreement with Artegiani *et al.* 1997b) for the three sub-basins. The daily averaged time series of water volumes are shown in Fig. 2.8.

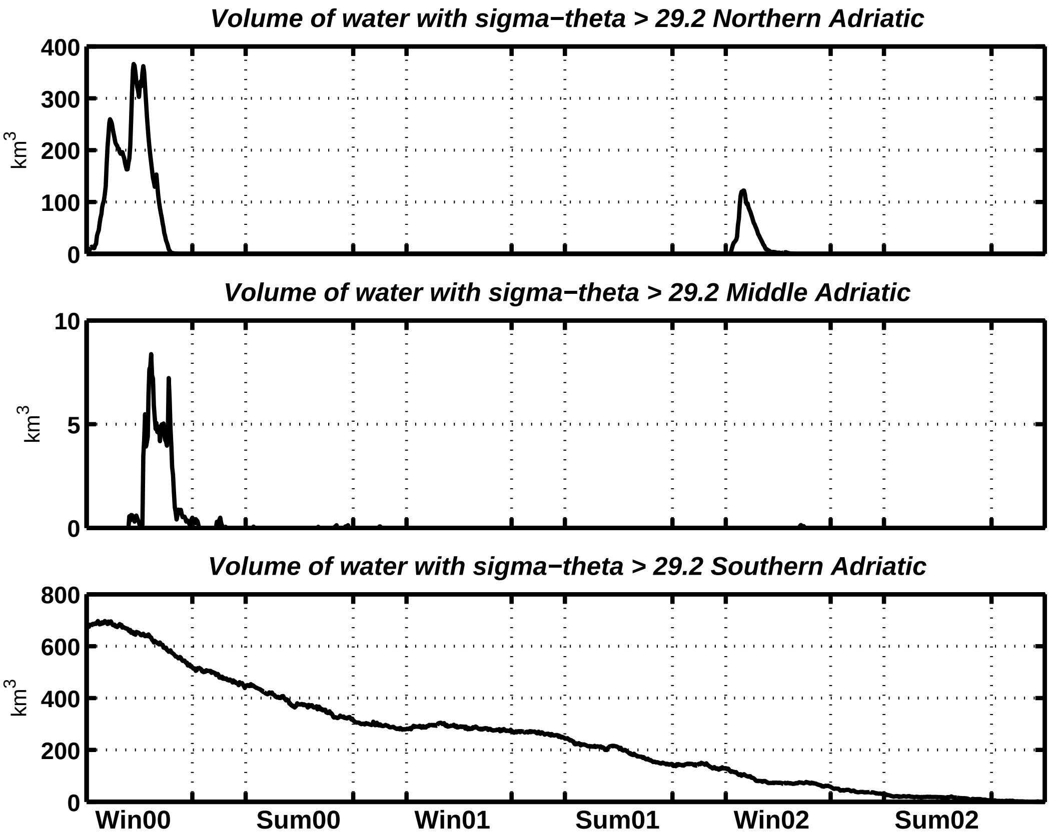

Figure 2.8 Temporal evolution of the total amount of waters having sigma-theta >29.2 kg m^{-3} in the three sub-basins (m^3).

It can be noted that the variability patterns in the three sub-basins have different temporal evolution. The time series of the northern sub-basin is characterized by the absence of dense waters in 2001. This confirms the different characteristics of this year with respect to 2000 and 2002. This absence is probably the consequence of the reduced cooling (Fig. 2.4) and strong river runoff (Fig. 2.3) occurred in autumn-winter 2000-2001. The middle Adriatic maximum value (Fig. 2.8 b) is reached later than the corresponding maximum in the northern area. Thus, we can conclude, in agreement with Artegiani *et al.* (1997 b), that a portion of northern

Adriatic dense water is advected southward toward the middle Adriatic depression. This advective process is not observed in 2002, probably because of the limited amount northern Adriatic winter dense water formed (Fig. 2.8b). The volume of the Southern Adriatic dense water is maximum in winter 2000 and progressively decreases in 2001 and 2002.

In order to validate the model's skill in reproducing the dense water formation process variability we computed the sigma-theta seasonal means along transects A and C (locations shown in Fig. 2.1) for the MAT observations. In Tab. 2.2 the presence/absence of waters with density values greater than the threshold value (29.20 kg m^{-3}) are reported. We must note that dense waters are present only during the winter and spring of 2000 and 2002 in partial agreement with the model results shown in Fig. 2.8. We have to point out that computing, from model results, the amount of deep waters on the same sections of the MAT observations we could not find the water masses. This is probably due to the general underestimation of the model salinity as further discussed in section 3.3. The amount of dense waters formed by the model is thus low than observed in the MAT dataset. A likely consequence is the absence of the residual dense water in spring, in contrast with the MAT dataset. Thus, the model solution is only in a qualitative agreement with the observations along the sections in terms of overall temporal variability.

	2000	***2001***	***2002***
Winter	Presence	Absence	Presence
Spring	Presence	Absence	Presence
Summer	Absence	Absence	Absence
Autumn	Absence	Absence	Absence

Table 2.2 Presence/Absence of dense waters (σ_θ > 29.20 kg m^3) in the MAT dataset used in this study.

In order to have a synthetic index of the Adriatic Sea thermohaline circulation variability, we computed the meridional transport streamfunction, Ψ , by integrating the total north-south transport across lines of constant longitude

(Peixoto and Oort 1992):

$$\Psi(z) = -\int_{x_0}^{x_1}\int_{H}^{z} v \; dxdz$$

With -H.< z < η. The velocity field is now tangent to the isopleths of Ψ and this is indicative of the vertical circulation in the basin. The negative values correspond to an estuarine cell turning cyclonically around the negative Ψ values, the positive Ψ values are indicative of an antiestuarine cell. In Fig. 2.9 the results of such computation are shown. The model solution appears as a complex system of estuarine and antiestuarine cells varying in intensity, vertical and horizontal extension. The first cell (E1) is surface intensified and it is estuarine or wind driven, extending from the northern to the southern regions and is connected to river runoff and Ekman pumping in the surface layers. The second estuarine cell (E2) is positioned at the bottom of the Southern Adriatic, leaning toward the Otranto Strait sill. This bottom intensified estuarine cell is totally new and might be connected to deep waters not locally produced but advected southward from the northern shelves of the basin.

In the southern Adriatic two large anti-estuarine cells (A1 and A2) are present at mid-depth, one positioned on the Otranto Strait and the other on the northern part of the Southern Adriatic depression. The anti-estuarine cells are connected to the dense water formation processes occurring on the downward branch of the cells and then forcing the return flow with a slow interior upwelling motion. The only period with weak anti-estuarine circulation is winter 2001 (Fig. 2.9 b) while the

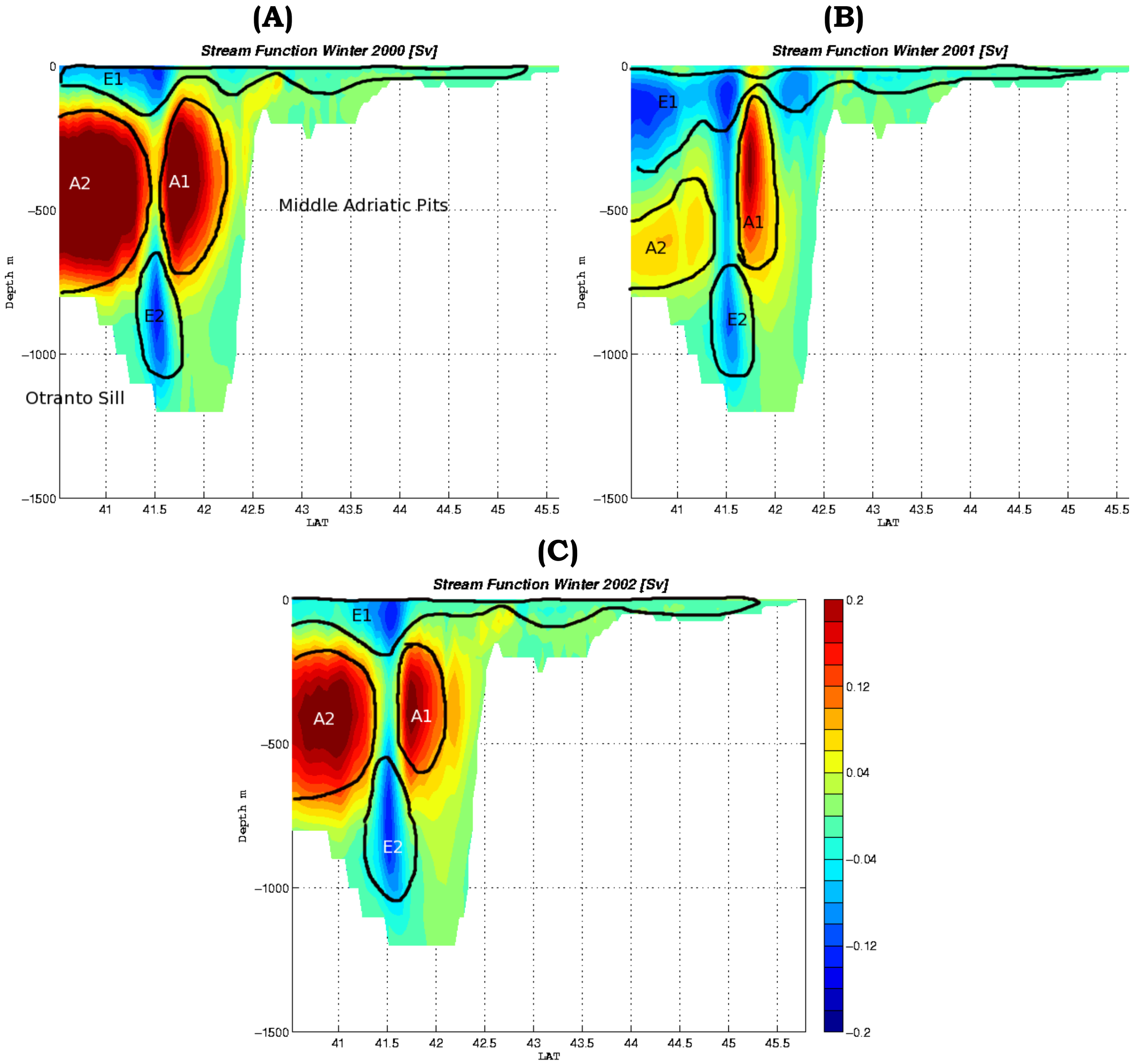

Figure 2.9 Meridional transport stream function (Sv) winter mean for: (a) year 2000; (b) year 2001; (c) year 2002.

other two winters show intensification of the anti-estuarine cells. In 2001 the E1 and E2 cells almost connect, hinting to the fact that in this year the estuarine character of the circulation is enhanced, due to the large Po runoff of autumn 2000 and winter 2001 and the weaker winter cooling affecting the amount of deep waters formed, as discussed above. The estuarine cell is clearly due to the large WACC extension and strength during 2001 reinforcing the outflow and southerly mass exchange.

The interface depth between estuarine and antiestuarine cells varies strongly with the years and the seasons, going from 100 m in winter 2000 and 2002, to 400 meters and deeper in the winter of 2001.

2.3.3 Comparison between observations and model results

Observational activities in the Adriatic Sea for the period 2000-2002 include surveys of the northern Adriatic carried out within the MAT Project, and the NATO-SACLANT ADRIA-01 cruise. In order to assess the model performance we have compared the model results with observations along two sampling transects of the MAT Project and with the basin wide observations from the ADRIA-01 data survey.

The MAT data considered for this comparison have been collected along the transects A and C shown in Fig. 2.1 with an approximate monthly frequency (see table 2.3 for a listing of the sampling dates). Samplings have been grouped by seasons and averaged. In order to carry out a consistent comparison with observations, model results corresponding to the MAT sampling dates have been similarly averaged. The observed and modeled winter temperatures distribution along the transect A are shown in Fig. 2.10. Observations for winter 2000 and 2002 (Fig. 2.10 a and c respectively) show a relatively well mixed area in the easternmost part of the section and stratification in the western. Winter 2001 (Fig. 2.10 b) appears quite different from the years described above, as the whole section is warmer and with very weak stratification. This different structure is due to the averaging of unevenly sampled data since year 2001 is biased towards the winter conditions (cf. Tab. 2.3). The difference in values is instead due to the interannual variability. The model reproduces the observed interannual variability, as the modeled winter 2001 is warmer than that of the years 2000 and 2002.

	2000	*2001*	*2002*
Winter	5-Jan 21-Feb 21-Mar 17-Apr	6-Feb 20-Feb 15-Mar	14-Jan 20-Mar 18-Apr
Spring	1-Jun 20-Jun	29-May 26-Jun	7-May 4-Jun 25-Jun
Summer	6-Jul 22-Jul 10-Aug 24-Aug 24-Oct	26-Jul 21-Aug 26-Sep 26-Oct	31-Jul
Autumn	5-Dec 14-Dec	22-Nov	

Table 2.3. Dates of the MAT samplings in the three years of the project (columns) sorted according to the seasons definition of Artegiani *et al.* (1997 a, b) (rows).

The agreement between spatial structures in the model and observations is less clear, as the model does not seem to reproduce the stratified structure in the western part of the section well, particularly in the years 2000 and 2002. For these years the model seems to be affected by excessive mixing processes that do not maintain the observed stratification structure in the WACC region.

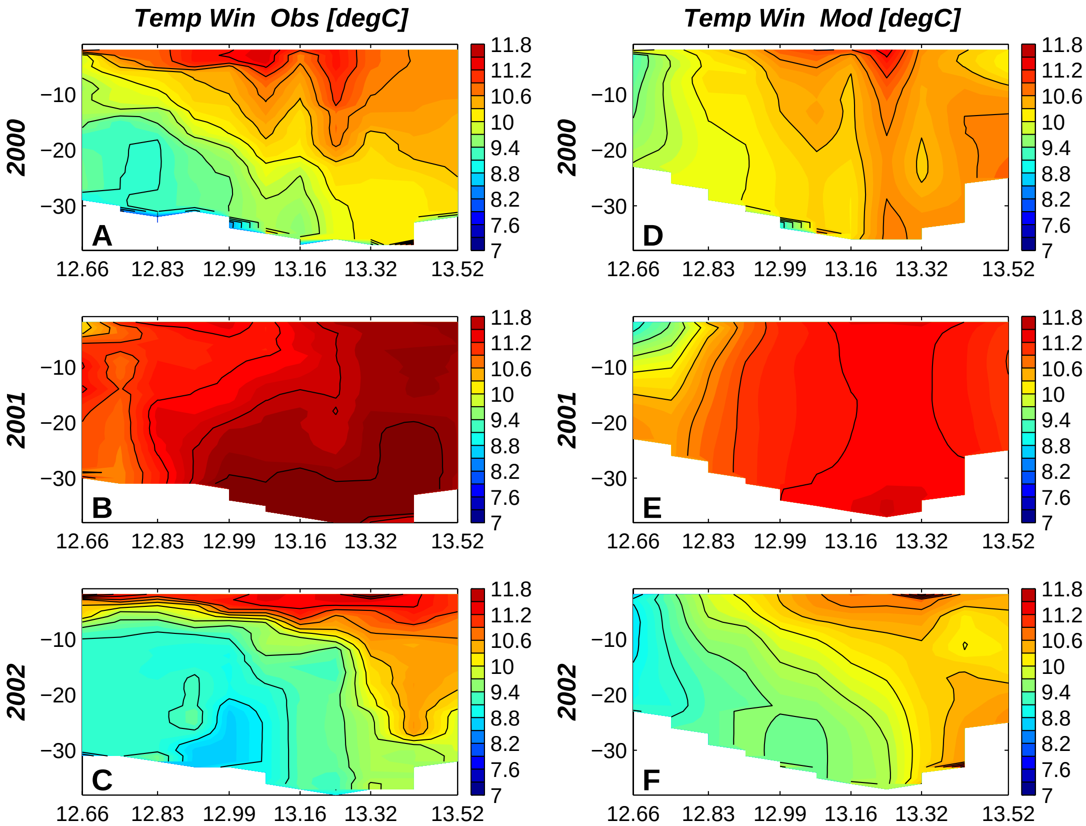

Figure 2.10 Vertical temperature distributions (°C) along the transect A for the simulated winters. (A-B-C) 2000, 2001 and 2002 winters means from observations. (D-E-F) 2000, 2001 and 2002 winters means from model results. The position of the transect is reported in Figure 2.1.

The observed and model predicted salinity sections for the same season are shown in Fig. 2.11. In addition to the mixing problem pointed out above, the model predicted salinity is lower than observed as a consequence of the missing inflow of very salty waters from the Ionian Sea and probably of an overestimation in the climatological river runoff from Adriatic rivers other than the Po. The differences between observed and climatological (Artegiani *et al.* 1997 a, b) salinity for transects A and C during winter are shown in Fig. 2.12. The positive anomalies indicate that in 2000 and 2002 waters of higher salinity values than the climatology intruded in the Adriatic Sea and reached the northernmost part of the basin (transect A). We argue that this is the signal of the Aegean intermediate waters formed during the Eastern Mediterranean transient (Klein *et al.,* 1999, Manca *et al.*, 2002). Unfortunately these waters are absent at the model open boundary in the Ionian Sea, thus giving rise to a large discrepancy between model solutions and observations.

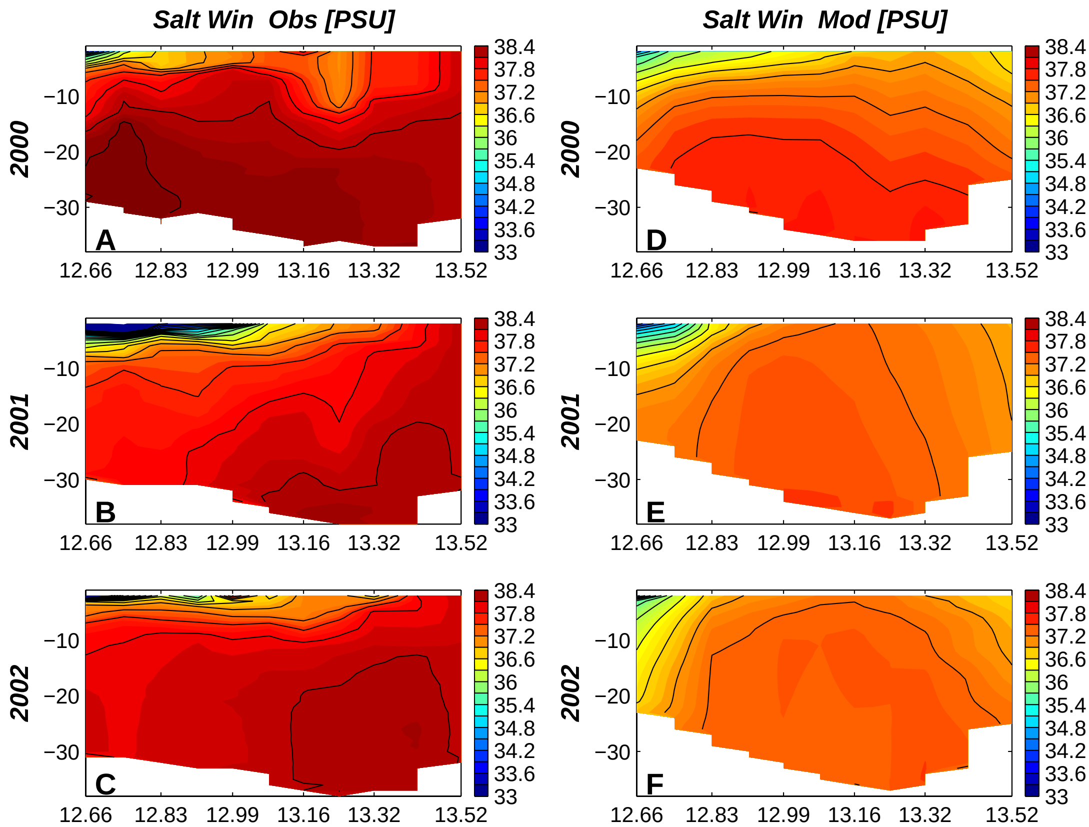

Figure 2.11 Vertical salinity distributions (psu) along the transect A for the simulated winters. (A-B-C) 2000, 2001 and 2002 winters means from observations. (D-E-F) 2000, 2001 and 2002 winters means from model results.

The spring surface thermal gains determine the onset of a strong vertical stratification that is reproduced in a satisfactory way by the model along section C (Fig. 2.13). The observed and simulated temperatures are in the range between 22.5°C near the surface and 11°C on the bottom.

During the summer, along section C, (Fig. 2.14) the temperature and the stratification strengthen and a strong thermocline on the 20 m depth appears in the observations. The surface heat gain determines temperatures higher then 23°C during all of the summers, with a minimum during 2001. The bottom cold waters are not influenced by the interannual variability of the seasonal warming and the temperature values are about 14°C in all of the years. The model solution has a weaker stratification and seems to match the observed interannual variability characterized by a warmer 2002 summer well.

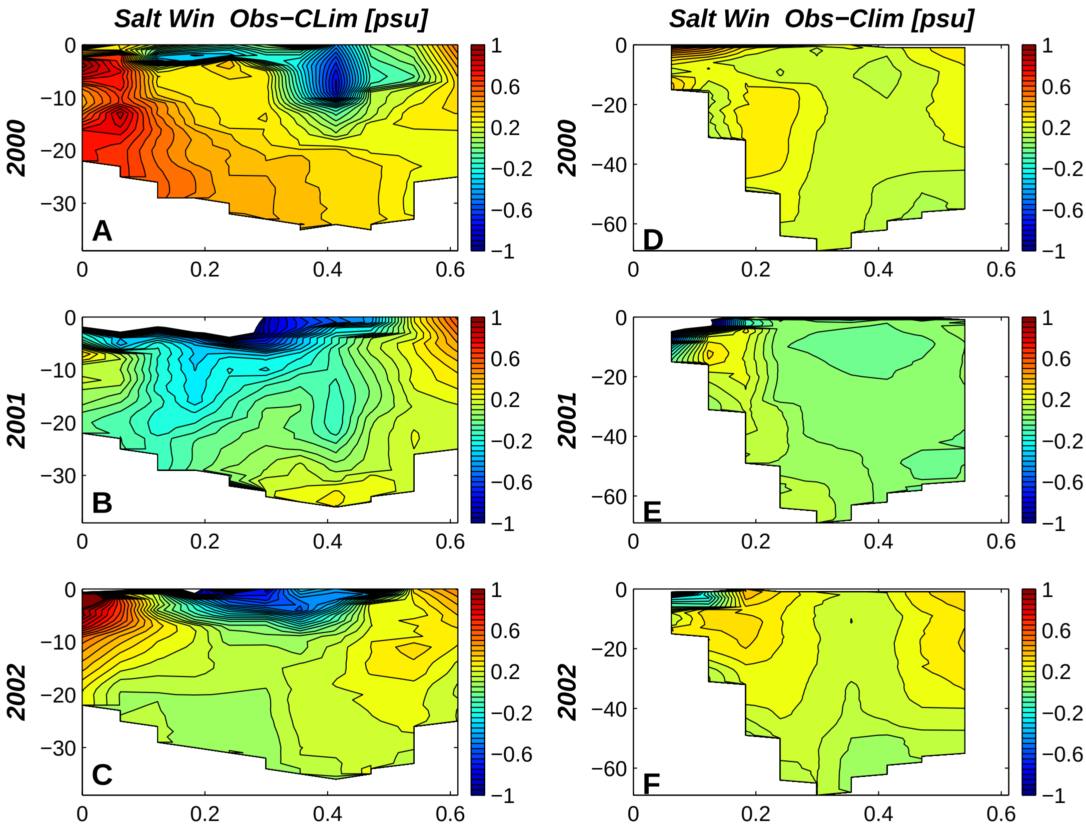

Figure 2.12 Differences between climatological salinity (Artegiani et al. 1897 a, b) and MAT project data along the transects A and C. A winter 2000, B winter 2001, C winter 2002, along transect A. D winter 2000, E winter 2001, F winter 2002, along transect C.

The two observed autumns of 2000 and 2001 (Fig. 2.15) along the section A are probably the seasons with the greatest signal of interannual variability. Modeled and observed autumns, along transect A of the year 2000, are characterized by high temperature and a stratification in the middle part of the section. In both the datasets the signal of the WACC cold waters is evident. During 2001 the observed and simulated temperatures are quite different and the vertical processes seem to have an important role in the dynamics.

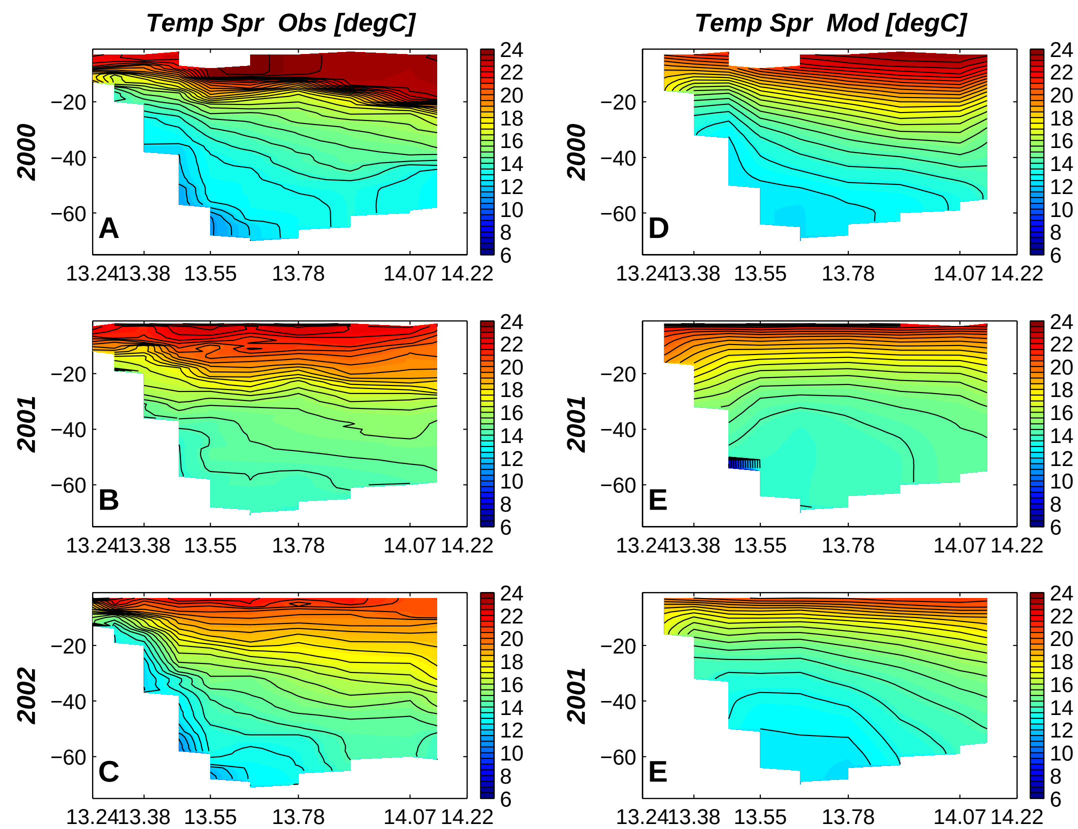

Figure 2.13 Vertical temperature distributions (°C) along the transect C for the simulated springs. (A-B-C) 2000, 2001 and 2002 springs means from observations. (D-E-F) 2000, 2001 and 2002 springs means from model results. The position of the transect is reported in Figure 2.1.

In order to gain a better insight of the model solution and its similarities with the observed data we present a comparison between a horizontal field obtained from ADRIA01 (Fig. 2.16a) dataset, covering the entire basin, and the model results (Fig. 2.16b).The ADRIA-01 data were collected during a period of about 20 days during February of 2001 and here they are considered synoptic and compared with the model predicted monthly mean for February 2001. The field of temperature at 5 m depth has been obtained applying an objective analysis scheme (Carter and Robinson, 1987) to the ADRIA01 dataset. The observed data shows a clear signal of the WACC and an inflow corresponding to the ESAC, carrying warm waters that reach the middle part of the basin. The simulated pattern of the WACC waters is wider and less intense than observed. In the southern part of the basin the model matches the west-east gradient found in the observed data. The difference between modeled and observed temperature around the latitude of 42 N (Gargano Peninsula) is probably related to the isotropic function used in the objective analysis.

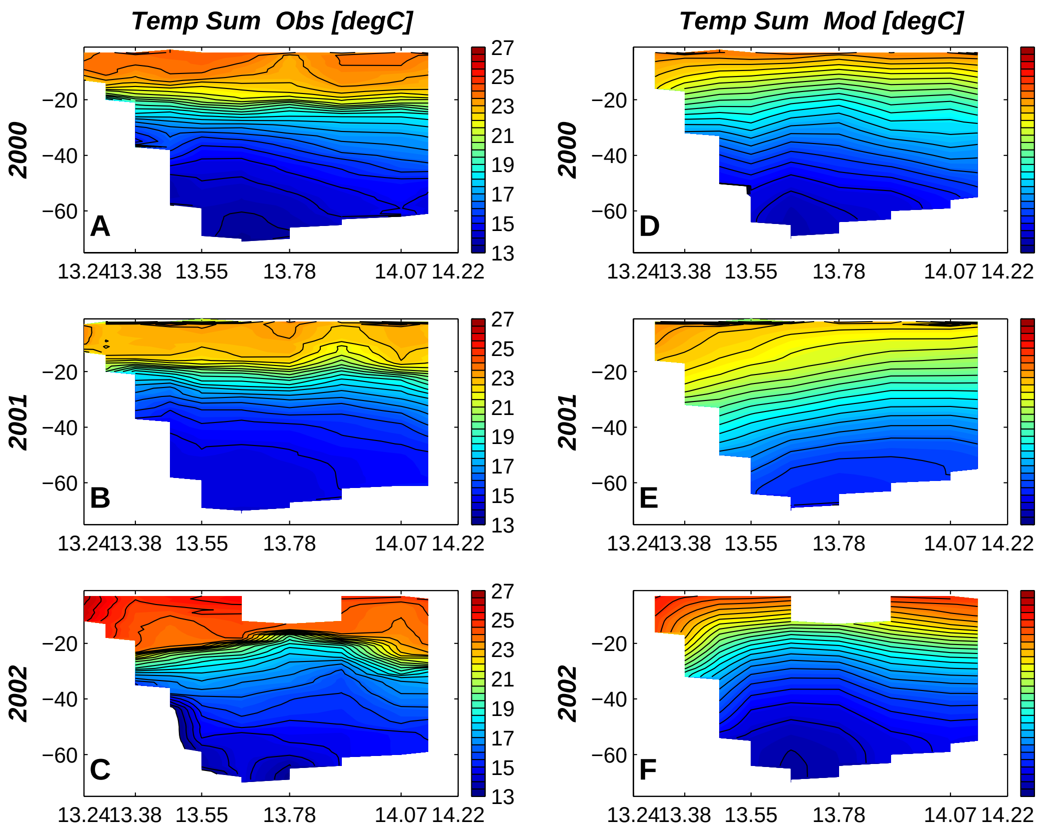

Figure 2.14 Vertical temperature distributions (°C) along the transect C for the simulated summers. (A-B-C) 2000, 2001 and 2002 summers means from observations. (D-E-F) 2000, 2001 and 2002 summers means from model results.

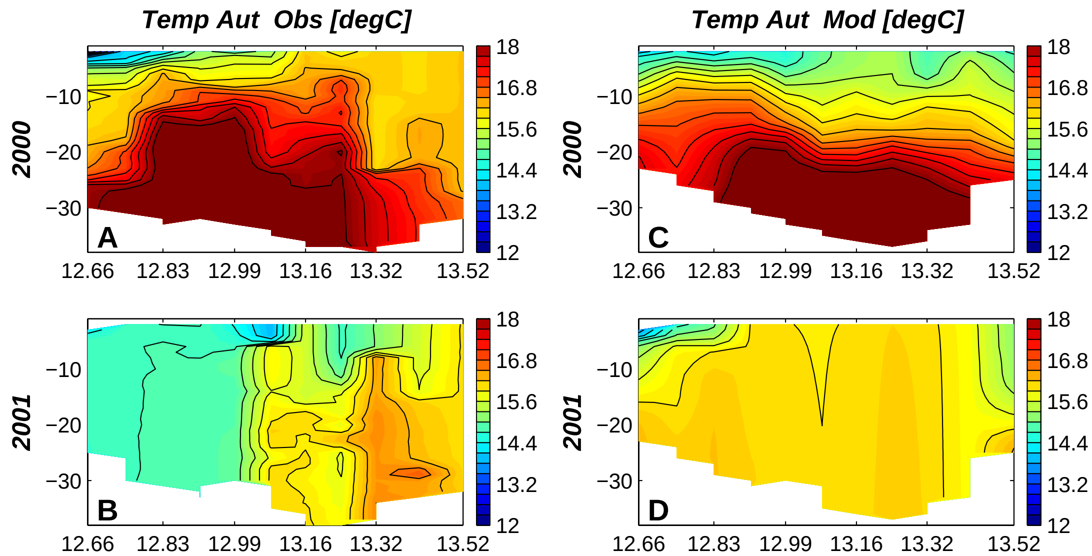

Figure 2.15 Vertical temperature distributions (°C) along the transect A for the 2000 and 2001 autumns. (A-B) 2000 and 2001 autumns means from observations. (C-D) 2000 and 2001 autumns means from model results.

2.4 Discussion and Conclusions

This paper has described the 2000-2002 interannual variability of the Adriatic Sea circulation from model simulations. The model results show a strong interannual variability in intensity and characteristics of all the known physical circulation structures. The WACC is most intense in winter while in summer detaches the coast and forms meanders and anticyclonic eddies (Fig. 2.7). The NAd gyre is well reproduced and is particularly strong in summer. Its position and shape varies interannually and his characterized by the southernmost extension in summer 2002. The structure of the surface currents in summer 2001 is marked by the presence of the Istrian Coastal Countercurrent (Supic *et al.*, 2000) even if, at this model resolution, the ICC is poorly resolved (Zavatarelli and Pinardi, 2003). The SAd gyre is well defined throughout the whole simulation period.

Overall, the years 2000 and 2002 are similar to each other, while 2001 is different mostly because of the characteristics of the autumn 2000 surface forcing and the winter-spring 2001 sustained freshwater Po runoff. The three sub-basins seem to be differently affected by the forcings functions. The dynamics of the northern

(A)

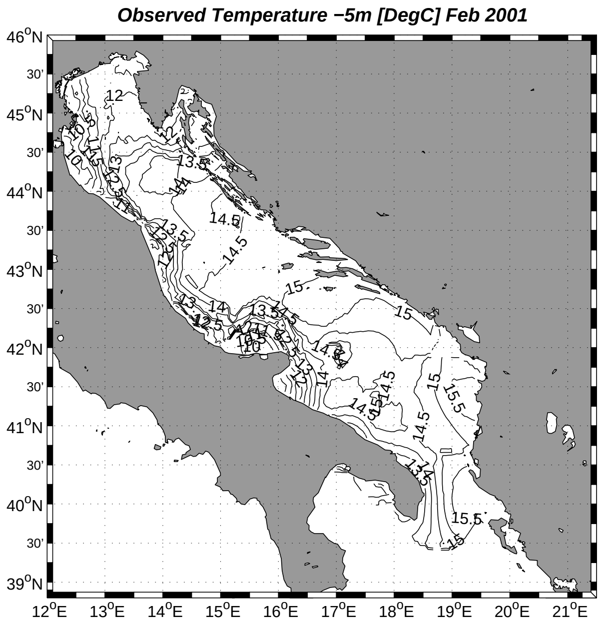

(B)

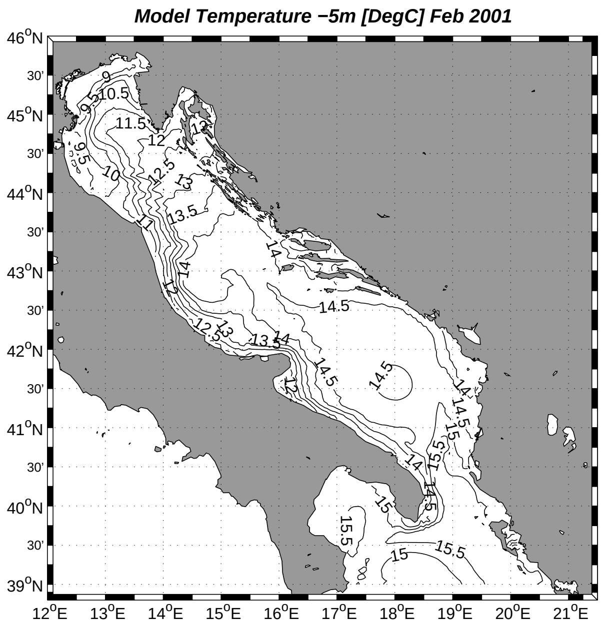

Figure 2.16 February 2001 monthly mean near surface (5m depth) temperature (°C) from (a) ADRIA01 observations and (b) model results.

and middle part of the basin are clearly the consequence of atmospheric forcing and the Po river runoff. The circulation in the southern part of the basin results from an equilibrium between atmospheric forcing and the inflow-outflow regime through the Otranto Strait. The most relevant atmospheric and river event observed during the studied period is the mild autumn-winter 2000-2001 with a large Po runoff producing no deep waters in the northern and middle Adriatic basins.

The basin thermohaline circulation has been diagnosed in terms of two estuarine and two anti-estuarine cells occupying different portions of the basin vertical and meridional extension. The surface is dominated by an estuarine cell that is very strong in 2001. The intermediate and deep waters in the southern Adriatic basin are dominated by two anti-estuarine cells connected to the local water formation mechanisms and inflow of LIW from Otranto.

The comparison with available observations shows a general overestimation in the vertical and horizontal mixing processes and a deficiency connected to the inflow of salty waters from the Ionian Sea. However, we noticed a good agreement between observed and simulated interannual trend. Future improvements involve the sensitivity to nesting boundary conditions, increase of the model resolution and data assimilation.

Chapter 3

The Adriatic Basin Forecasting System

Note that this Chapter is a co-authored paper with Prof. N. Pinardi, Dr. M. Zavatarelli and A. Coluccelli entitled “The Adriatic Basin Forecasting System” submitted for publication in “Acta Adriatica” ADRICOSM special issue.

3.1 Introduction

Ocean physical processes play an important role in governing and/or constraining marine acoustical, biological and sedimentological dynamics. Therefore, forecasting physical ocean fields can greatly contribute to the understanding of the functioning of marine sub-systems, as well as providing an efficient support tool for marine environmental management.

Numerical ocean models for forecasting started being developed at the beginning of the nineteen-eighties (Pinardi *et al.* 2002). The progress in computer power and efficient/accurate numerical techniques led to a progressive increase of numerical ocean models spatial resolution and overall quality, which now allows for the simulation of mesoscale and coastal dynamics.

Within the ADRICOSM (ADRIatic sea integrated COastal areaS and river basin

Management system) Pilot Project, a near real time monitoring system and a near real time basin-shelf marine forecasting system has been implemented and is now being used in operational mode for the Adriatic Sea.

The semi-enclosed Adriatic Sea (Fig. 3.1) is a particularly challenging environment for the development of such a system (Zavatarelli *et al*., 2002), as the bottom morphology, the surface forcing functions (highly variable at the interannual and seasonal scales) and the exchanges with the Mediterranean Sea through the Otranto Channel define a variety of oceanographic dynamical regimes, ranging from coastal (the northern part of the basin is entirely epicontinental and affected by strong riverine freshwater input), to open sea (the southern Adriatic basin is 1200 meters deep and interacts strongly with the Ionian open ocean waters). Moreover, the basin is also a well known site of dense water formation occurring, with different dynamics, on the northern and in the southern sub-basins (Artegiani *et al*. 1989; Ovchinnikov *et al*., 1997; Manca *et al*., 2002).

A forecasting system for a basin capable of dealing with these characteristics must include four interacting components (Pinardi *et al*., 2002): an atmospheric component, providing surface forcing functions from operational atmospheric analyses and forecasts; a remotely sensed and in situ ocean observing system capturing both the coastal and the open sea variability; a numerical ocean circulation model and a proper data assimilation scheme allowing for an efficient melding of the observations into the initial condition for the forecast.

In this paper we concentrate on the numerical model component of the forecasting system and we show results from the operational forecasting activity of the model, obtained without the data assimilation, and compare the forecast/simulations with independent observations in order to provide a first quantitative assessment of the model forecast skill. Preliminary considerations on the performance of the model with the active data assimilation procedure are instead described in Grezio and Pinardi (2005).

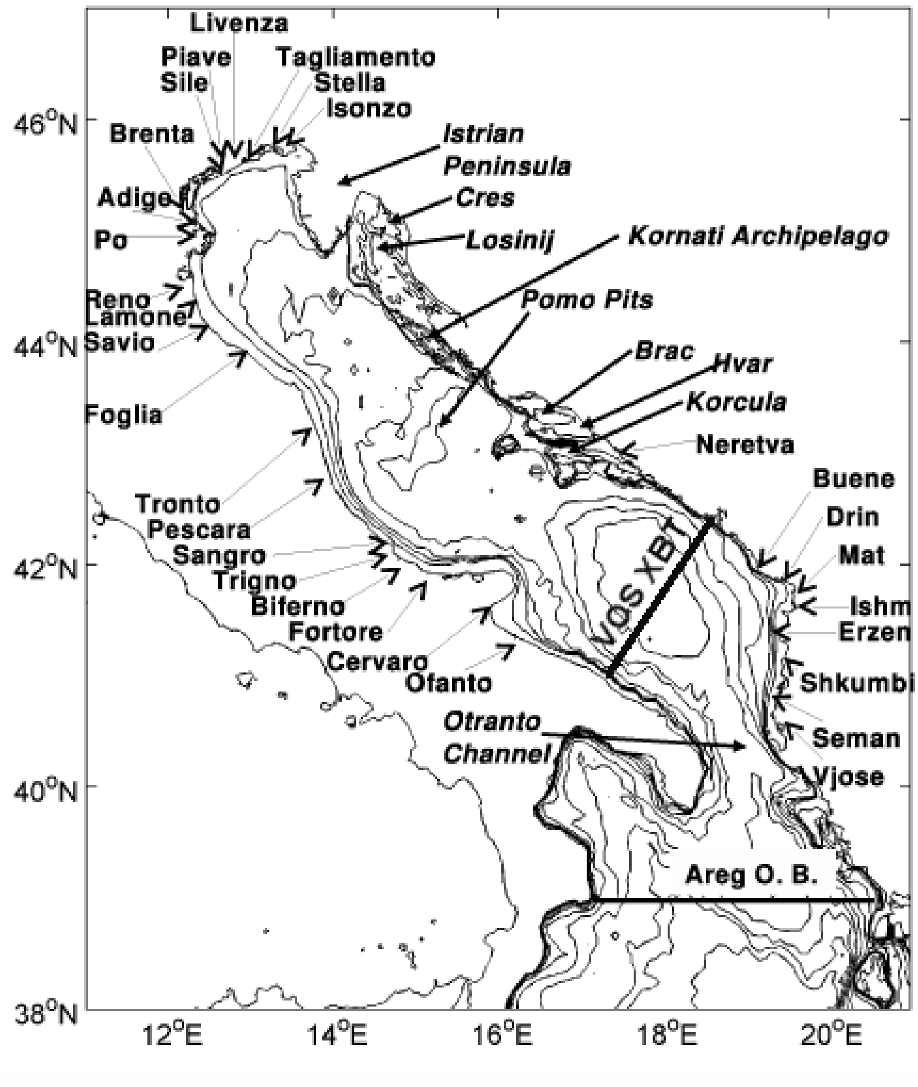

Figure 3.1 The Adriatic Sea coastal and bottom morphology. The figure shows also the locations of the river mouths discharging into the basin, the islands retained in the AREG model geometry, the track of the VOS XBT observational program and the location of its open boundary (AREG O.B.). Redrawn with modifications from Zavatarelli and Pinardi, 2003).

3.2 Methodology and system description

The Adriatic REGional model, hereafter called AREG, covers the entire Adriatic Sea basin and extends into the Ionian Sea (Fig. 3.1). The horizontal resolution is approximately 5.0 Km, while 21 σ (bottom following) layers define the vertical resolution. The model is based on the Princeton Ocean Model, POM (Blumberg and Mellor, 1987) as implemented in the Adriatic Sea by Zavatarelli and Pinardi (2003). The model contains an embedded second order turbulence closure scheme providing vertical diffusion coefficients (Mellor and Yamada, 1982). Horizontal diffusion is parameterized following the scheme of Smagorinsky (1993), as coded into POM by Mellor and Blumberg (1985). The current implementation makes use of an iterative advection scheme for tracers (Smolarkiewicz, 1984) implemented into POM following Sannino *et al*. 2002.

Surface boundary conditions are computed through standard bulk formulae parameterizations previously applied to the Adriatic (Maggiore *et al.*, 1998; Zavatarelli *et al*., 2002; Zavatarelli and Pinardi, 2003, Oddo *et al.,* 2005 see Chapter 2) and Mediterranean Sea (Castellari *et al.* 1998, Demirov and Pinardi, 2002). The surface fluxes computation has been carried out interactively, as the sea surface temperature (SST) field required by the bulk formula is provided, every time-step, by the model simulation.

The atmospheric data (air temperature, relative humidity, cloud cover and both the wind components) used to compute the surface heat and momentum fluxes have 0.5° horizontal resolution and 6hrs frequency and are provided by the European Centre for Medium Range Weather Forecast (ECMWF).

The water flux resulting from the equilibrium between evaporation minus precipitation and river runoff has been parameterized as a salt flux. The evaporation flux has been estimated from the interactively computed latent heat flux, while precipitation values have been obtained from the global climatological monthly means of Legates and Wilmott (1990). The crucially important river runoff data for all the Adriatic Sea rivers have been taken from the compilation by Raicich (1994) compilation of climatological monthly means relative to the Adriatic Rivers (in Fig. 3.1 the mouth location of all the Adriatic rivers considered in the model setup is reported), with the sole (and important) exception of the Po river discharge. The Po runoff is specified daily taking the values at the closing point of the drainage basin (Pontelagoscuro) and partitioned over six grid points approximately representing the proportion of the fresh water discharge through the mouth of the delta (Provini *et al*. 1992).

At the open boundary (Fig. 3.1) the model is one-way nested with the operational 1/8° resolution model of the entire Mediterranean (Pinardi *et al*., 2003) through the specification of daily averaged temperature, salinity and velocity fields. The definition of the nested open boundary conditions is based on Zavatarelli and Pinardi (2003), to which a nudging term for the scalar properties has been added in a limited area of the model domain immediately adjacent to the open boundary. The relaxation time for the nudging varies from 30 days, at the open boundary points, to 10 years, in the innermost area corresponding to the 10^{th} grid point. The forecasting system is operational since April 2003 and it releases 7-day forecasts and hindcasts every week. This paper evaluates the hindcast/forecast products for the period January 1^{st} 1999 – December 31^{st} 2003 in order to provide a first assessment of the model forecasting skill when used without any data assimilation. As initial condition (January 1^{st} 1999 at 00:00 GMT) the climatological temperature, salinity and velocity fields originated from the simulation of the Adriatic Sea circulation of Zavatarelli and Pinardi (2003) have been used.

The operational forecasting sequence is shown in Fig. 3.2. Every week the model is integrated for 7 days in hindcast mode from noon of the previous Tuesday (J-7) up to noon of the current week Tuesday (J), the starting time of the forecast. The numerical model is then integrated in forecast mode for 9 days (from J to J+9) using as initial condition the fields from the hindcast. The hindcast is forced by the ECMWF atmospheric analyses, uses the Mediterranean Forecasting System (MFS) analyses as lateral boundary conditions, and the observed daily Po run-off is imposed. For the forecast the model is forced instead by the atmospheric and lateral data from ECMWF and MFS forecasts.

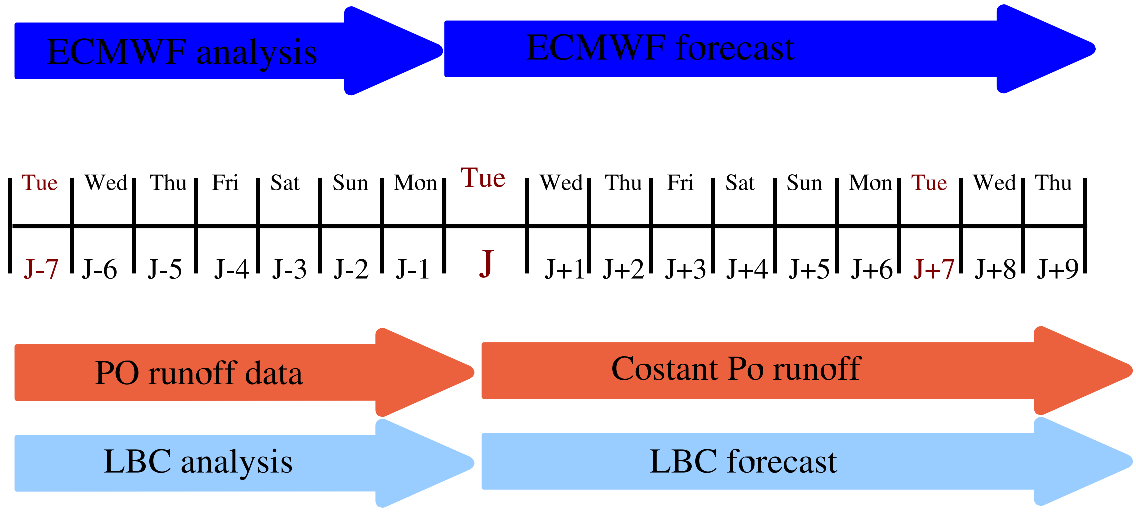

Figure 3.2 Time line of hindcast-forecast procedure. The arrows indicate the external data collected on Tuesday (J) and used for the model simulations. The analysis data span the period starting from noon of the previous Tuesday (J-7) to noon of the current Tuesday (J). The forecast data span the period from 6.00 p.m. of the current Tuesday (J) to Thursday of the next week.

3.3 Po runoff sensitivity studies

During the forecast, the most recent Po runoff daily value is persisted in time, since no forecasts of the runoff are presently available. This choice is motivated by the results of a sensitivity study done with simple and different forecasting methods of the Po runoff. This study has been performed with the Po river data for the year 2002. A 7-day forecast of the Po river discharge has been attempted using three different methods: persistence of the last available value; use of a climatological trend corrected on the basis of the last available data; forecast based on statistical extrapolation. For the second method a daily climatology has been previously obtained using a time series of daily Po runoff values spanning the period from 1991 to 2001. The result of such computation has been corrected on the basis of the anomaly between the last available data and the corresponding climatological value.

For the runoff forecast based on extrapolation, the coefficients of a polynomial of degree *n* are determined by linear methods from the fit of the observed data in a pre-defined *time window*. Different sensitivity experiments were carried out using different values for *n* and the *time window*. For all the tested cases a simple extrapolation gives high values of root mean square (RMS) error. For instance, using n=1 the obtained constant trend does not adequately predict the runoff because the natural variability of the Po river discharge is large even over a few days. Using *n* greater than 2 the resulting polynomial is not sufficiently constrained and the runoff forecast gives unrealistic extrapolated values. The best results have been obtained by fitting the coefficients of a polynomial of degree 3 (*n*) using a series of 22 values, where the first 15 values (*time window*=15) are the observations and the remaining data have been obtained persisting the last available value. An example of these computations is shown in Fig. 3.3.

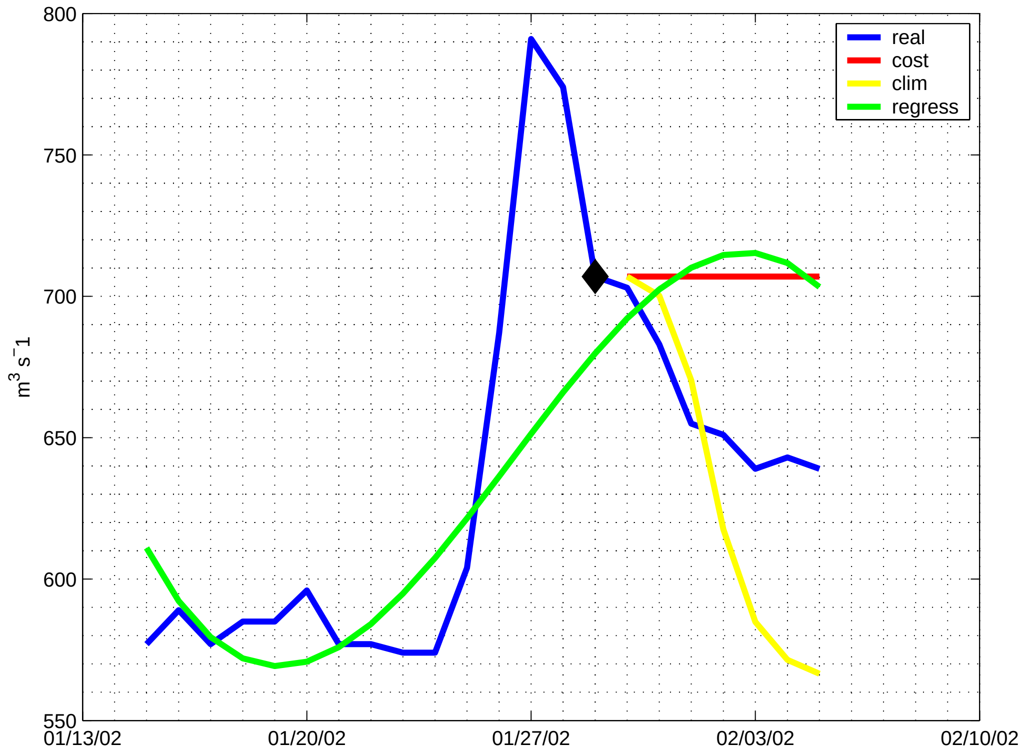

Figure 3.3 Example of Po runoff forecasts for the week from January 29th 2002 to February 5th 2002. The diamond indicates the last available Po data. In blue the observed runoff is reported. Green, Red and Yellow indicate the results of the different forecast methods tested.

The performance of the different Po forecast procedures has been assessed based on the RMS error between predicted and observed values. The time series of the RMS obtained using a constant value, a corrected climatology and the results of the polynomial approach are shown in Fig. 3.4 together with the variance of the Po runoff. The results of the three different approaches show similar RMS values and time evolution, moreover the "*constant*" approach has the lower annual mean RMS error.

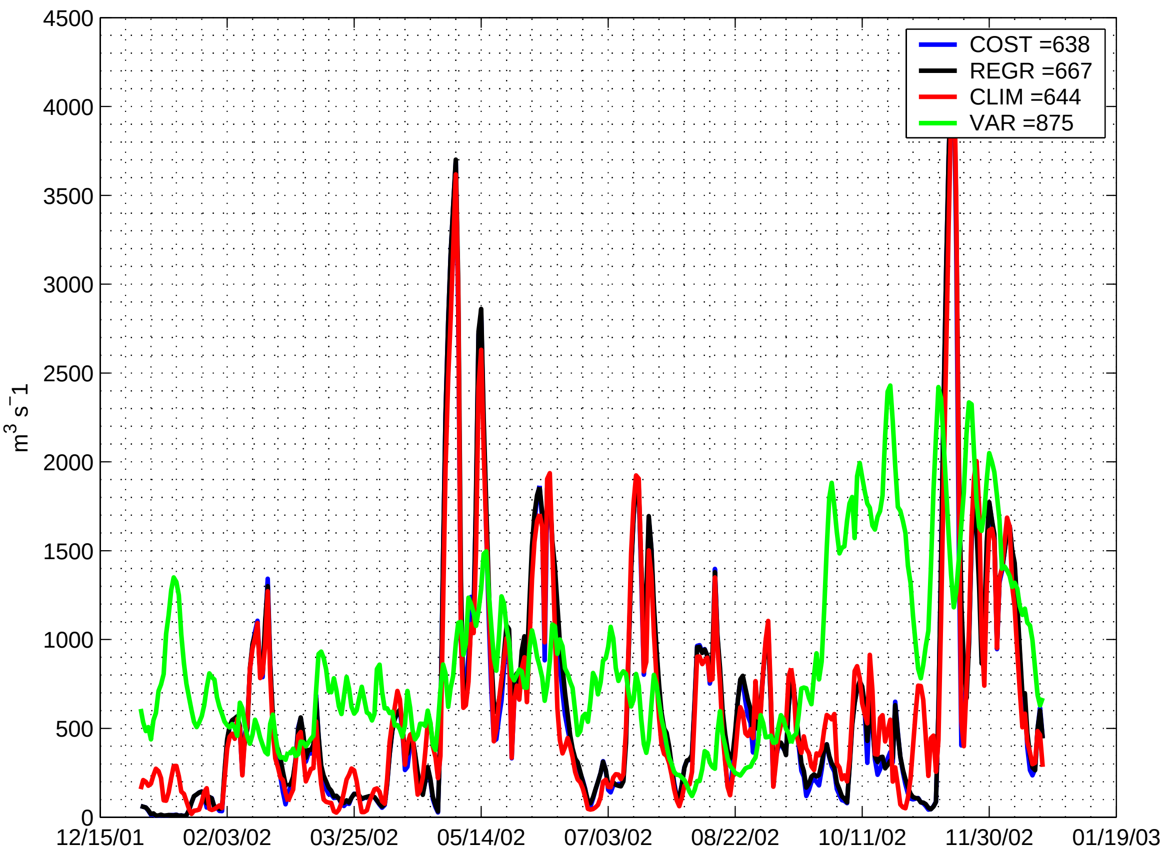

Figure 3.4 Time series of the RMS error computed between observed Po runoff values and different forecast methods. The variance of the Po runoff computed using 10 years of daily data is also given. In the legend the annual mean for each forecast method is given.

3.4 Analysis of hindcast quality and forecast accuracy

A detailed description and analysis of the 1999-2003 hindcast simulation, focusing on the interannual variability of the Adriatic Sea general circulation and on a comparison of the simulation results with in situ observations can be found in Oddo *et al*. (2005) (see Chapter 2).

In Fig. 3.5 the hindcasted seasonally averaged mean surface circulation for year 2003 is shown in order to provide an overall picture of the model behavior. We can note that the model successfully reproduces the well-known large scale circulation structure of the Adriatic Sea as well as its seasonal variability. Following the naming proposed by Artegiani *et al*. (1997a), the model simulates a well defined Western Adriatic Coastal Current (WACC) along the Italian coasts and the Eastern Southern Adriatic Current (ESAC), the intensity of which is seasonally modulated. The two coastal currents border the cyclonic gyres in the middle and southern Adriatic (middle, MAd, and southern, SAd, Adriatic gyres respectively), which are intensified in summer and autumn in accordance with the results of previous studies (Artegiani *et al*, 1997b, Poulain, 2001). The Northern Adriatic gyre is also well reproduced in the model results and its centre position shifts from season to season.

3.4.1 Hindcast quality

In Fig. 3.6a the comparison between the hindcasted basin averaged sea surface temperature (SST) and the corresponding averages from remotely sensed observations is shown. The satellite based SST daily fields are computed with a space/time objective interpolation scheme (Santoleri *et al*., 1991) on the AREG model grid filling also the cloud-covered areas. The comparison denotes a good overall qualitative and quantitative agreement between the hindcast and the remotely sensed SST for a large part of the annual cycle, with the notable exception of the summer period, during which the model seems to underestimate the surface temperature.

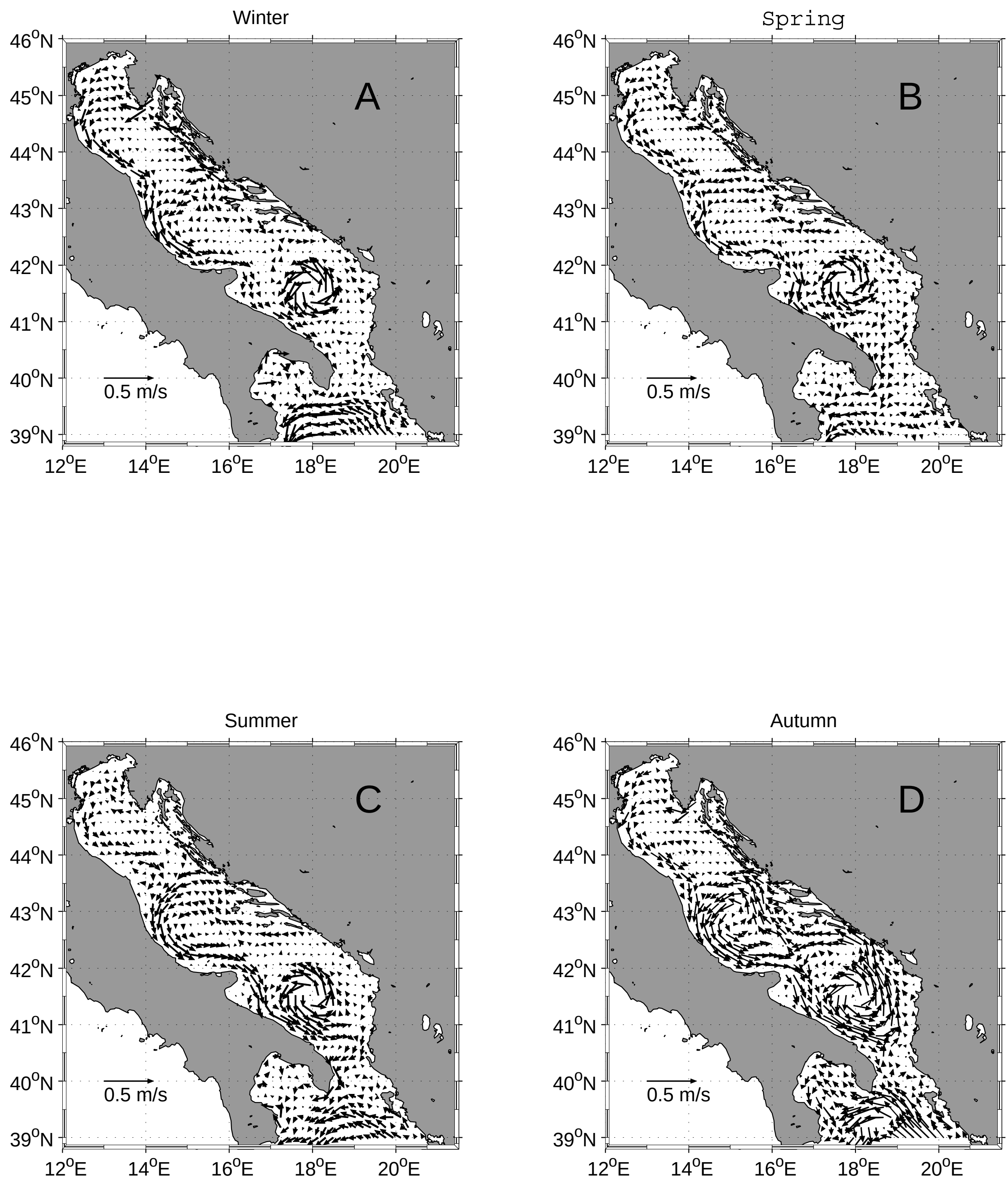

Figure 3.5 Seasonally averaged near surface (2m depth) velocity field. Winter from January to April; Spring May and June; Summer from July to October; Autumn November and December. The seasons definition was first proposed by Artegiani (1997 a,b).

A possible reason for this discrepancy has been discussed in Oddo *et al.* (2005) (see Chapter 2) and tentatively identified with the overestimation of the vertical mixing processes occurring in summer, determining the lower model surface temperature through mixing with subsurface water.

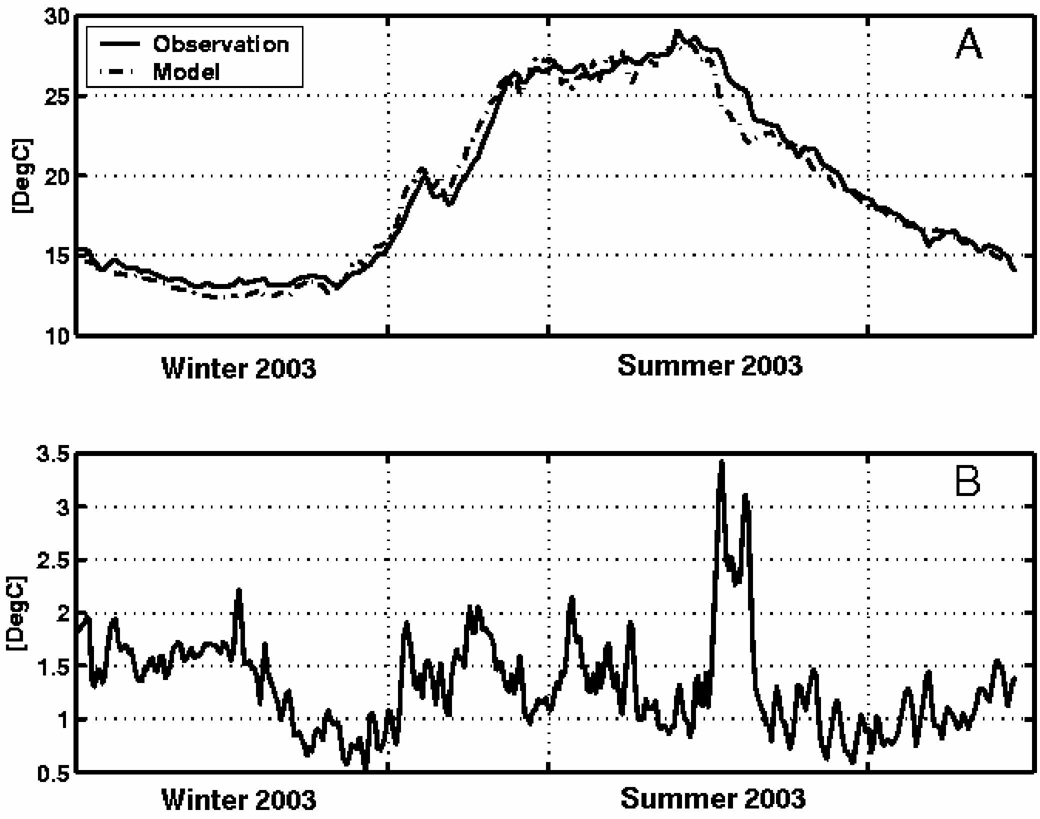

Figure 3.6 A: 2003 annual cycle of the basin averaged SST. The dashed line indicates the model hindcast; the solid line, the mean of satellite SST observations. B: Time series of the basin averaged RMS difference computed using the observed SST.

The accuracy and quality of the hindcast and forecast results has been studied by using Root Mean Square (RMS) error indices. The model RMS error, $E_{(i,j)}$, is defined as the difference between the predicted, $P_{(i,j)}$, and the observed, $O_{(i,j)}$, value:

$E_{(i,j)}=P_{(i,j)}-O_{(i,j)}$

The correspondent RMS error is therefore:

$$RMS = \left[\left(\frac{1}{N}\right)\sum E^2\right]^{\frac{1}{2}}$$

Where N is the total number of available data.

The RMS errors of the AREG hindcast and forecast are shown as horizontal maps and as time series. The former have been obtained by averaging temporally the RMS error values for each grid point, the latter by averaging spatially the RMS error calculated for each day. For the quality assessment, the RMS error has been computed using hindcast and observations (so-called RMS hindcast error), while for the forecast accuracy the RMS error is computed as the difference between forecast and hindcast (so-called RMS forecast error). The time series of the RMS error is shown in order to obtain a time varying synthetic index of the model results, while the horizontal error maps highlight the areas where the major model deficiencies are located.

In Fig. 3.6b the time series of the horizontal averaged RMS hindcast error for SST using satellite data for all of 2003 is shown. The time series reaches the minima in late winter and summer, is characterized by a well marked maximum in summer and has a mean bias of about 1.3 °C. We argue that the main reason for the high values of RMS hindcast error is the misplacement of the spatial structures probably related to the horizontal resolution of the atmospheric forcing. The horizontal structure of the same RMS error is shown in Fig. 3.7. The distribution clearly indicates that the main model deficiency is located in the shallow water areas, in particular in the regions affected by river runoff (see Fig. 3.1). This might be due also to the fact that we do not consider temperature effects for entering Po river waters in addition to forcing inaccuracies.

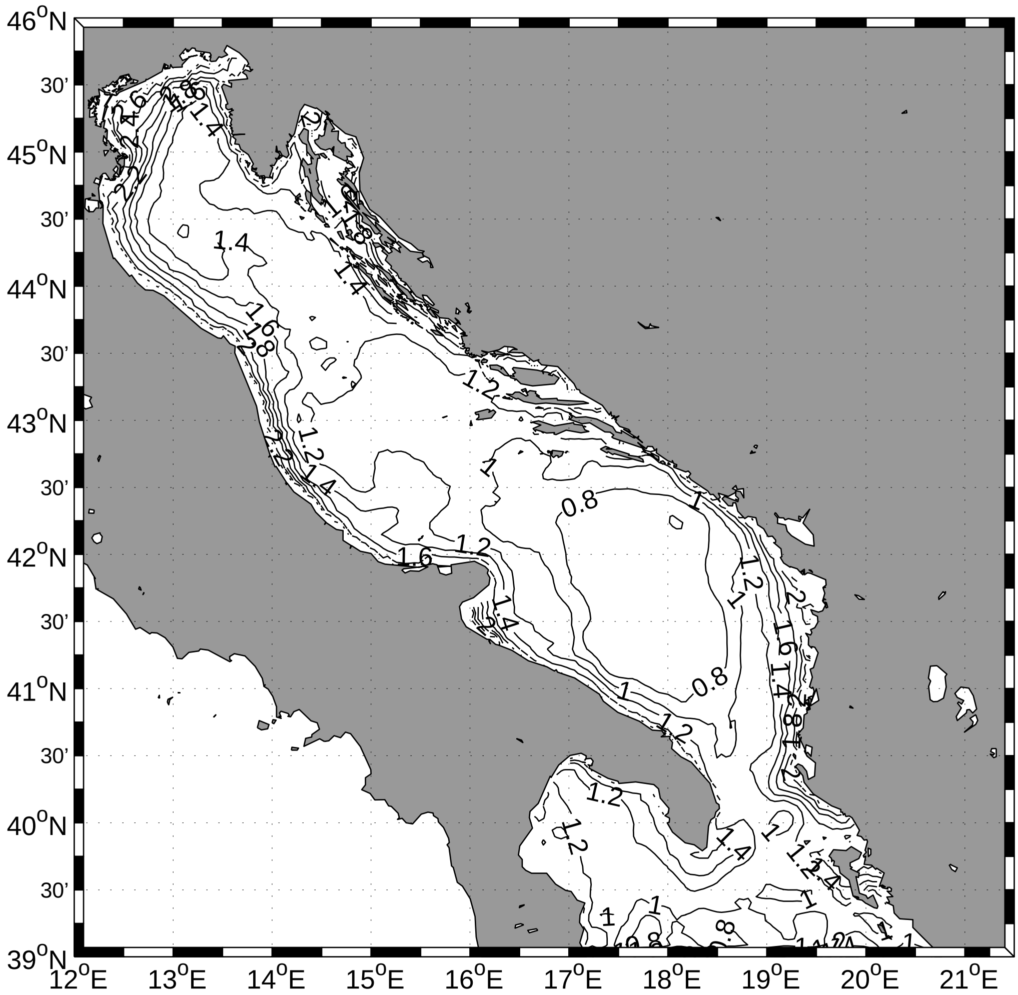

Figure 3.7 Spatial distribution of the annually averaged hindcast RMS error computed using the (remotely) observed and hindcasted SST. Units are °C.

During 2003 Expendable Bathythermograph (XBT) temperature profiles were collected as part of the ADRICOSM monitoring program for the open ocean areas of the southern Adriatic by means of Voluntary Observing Ships (VOS). Temperature data have been collected monthly along a track joining Bari and Dubrovnik and crossing the whole Southern Adriatic (see Fig. 3.1). These data also allowed the computation of the hindcast error for subsurface water properties. The RMS hindcast error computed between model results and XBT data is presented as a scatter plot and as vertical profiles in Fig. 3.8. The time evolution of the hindcast error (Fig. 3.8a) confirms that higher values are achieved in the summer period. The seasonal averaged vertical profiles of the hindcast temperature error reported in Fig. 3.8b indicate a good agreement between predicted and observed values under a depth of 150m for all seasons (autumn is missing because the VOS monitoring stopped). The winter profiles are characterized by a relative maximum at a depth of 400 m, probably related to an inexact vertical location of the Levantine Intermediate Water (LIW) intruding in the Adriatic through the Otranto Channel. In spring and summer the high values at the surface and the subsurface maxima confirm the problems in the vertical mixing affecting the upper layers.

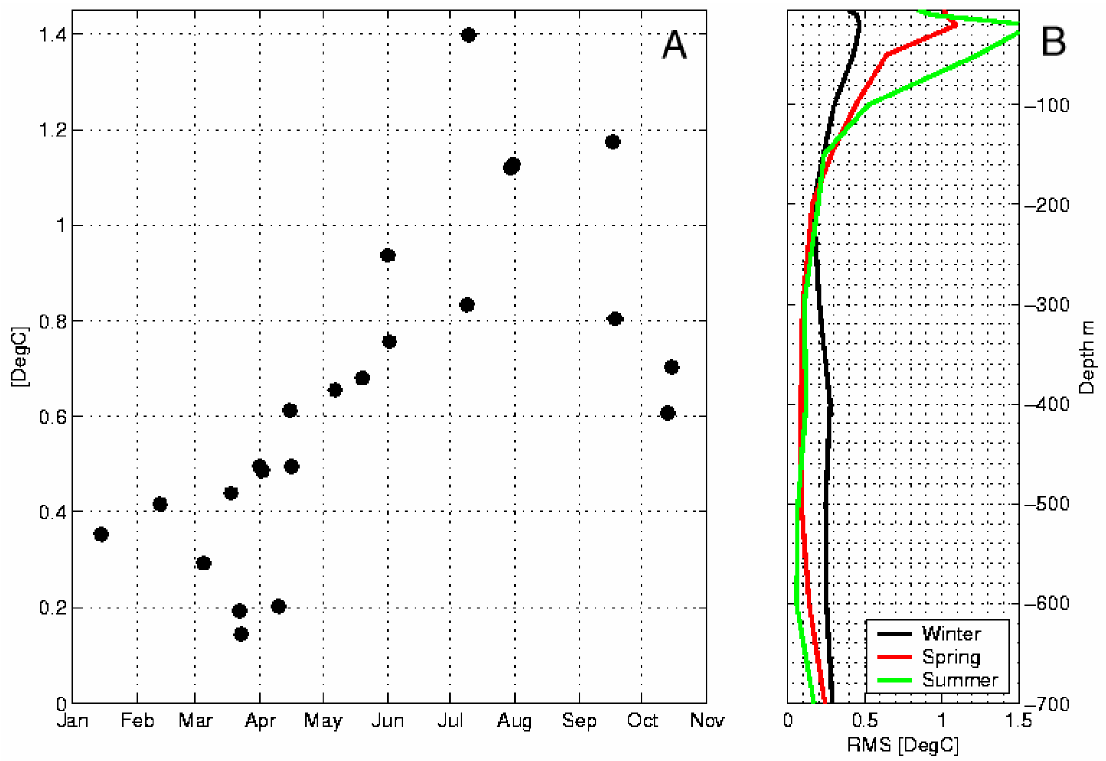

Figure 3.8 RMS errors computed using the VOS XBT data collected along the track indicated in figure 3.1 and the corresponding hindcasted temperature. A: Vertically averaged RMS error. B: Seasonally averaged vertical profiles of RMS error.

3.4.2 Forecast accuracy

In Fig. 3.9 we show a comparison between the hindcast and forecast 2m temperatures for the second, fourth and seventh day of the forecast together with the corresponding hindcast and their differences (hindcast - forecast). Fig. 3.9 indicates that the main differences are in the frontal regions of the WACC and in the PO plume. It is interesting to notice that the differences reach a maximum at day 4 and then decrease due to the non-linear dynamics of the regions, which amplify the errors in the forcing functions of the forecast (atmospheric forecast and Po runoff held constant) with a non-exponential law.

The first forecast accuracy index is given by the RMS forecast error for the surface temperature and salinity fields from April 1st to December 31st 2003. In addition we show the so-called RMS persistence error where the forecast is assumed to be made persisting the initial condition and then differences are computed with the hindcast. The RMS forecast and persistence errors are shown in Fig. 3.10.

The RMS forecast temperature error (Fig. 3.10a) is always significantly lower than the corresponding RMS persistence error and this gives a generic motivation for the necessity of a numerical forecast system. In terms of temperature the accuracy of the forecast decreases in spring and early summer, whilst being practically constant in autumn. On the other hand, the forecast error in the surface salinity (Fig. 3.10b) reaches the minimum values in summer and generally shows lower variability with respect to the error temperature time series. The summer minima are obviously a consequence of the low Po runoff variability.

The horizontal map of the time averaged RMS forecast error for surface temperature and salinity are shown in Fig. 3.11 and Fig. 3.12 respectively. The surface temperature RMS forecast error has an east-west gradient with the maxima along the east coast. The pattern of the salinity RMS forecast error has an extended maximum in front of the Po Delta, obviously related to the Po forecast errors, and other maxima closer to the east coast. We argue that the higher forecast error in temperature and salinity along the eastern Adriatic side is mainly due to atmospheric forcing inaccuracies, whilst the salinity forecast error is dominated by the Po runoff uncertainties.

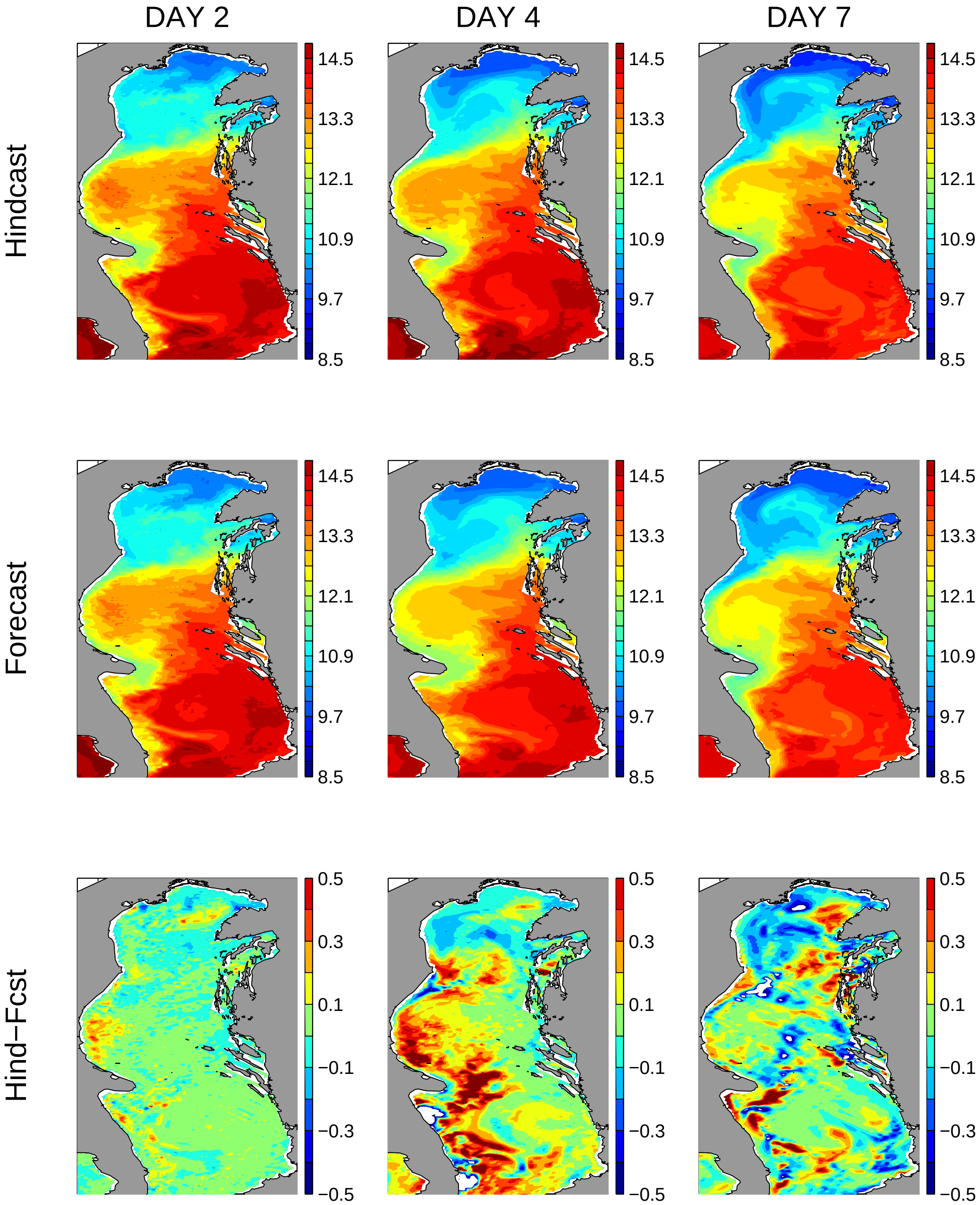

Figure 3.9 Horizontal maps of near surface (2m depth) hindcasted, forecasted temperature and differences. The second, fourth and seventh days of the simulations are shown.

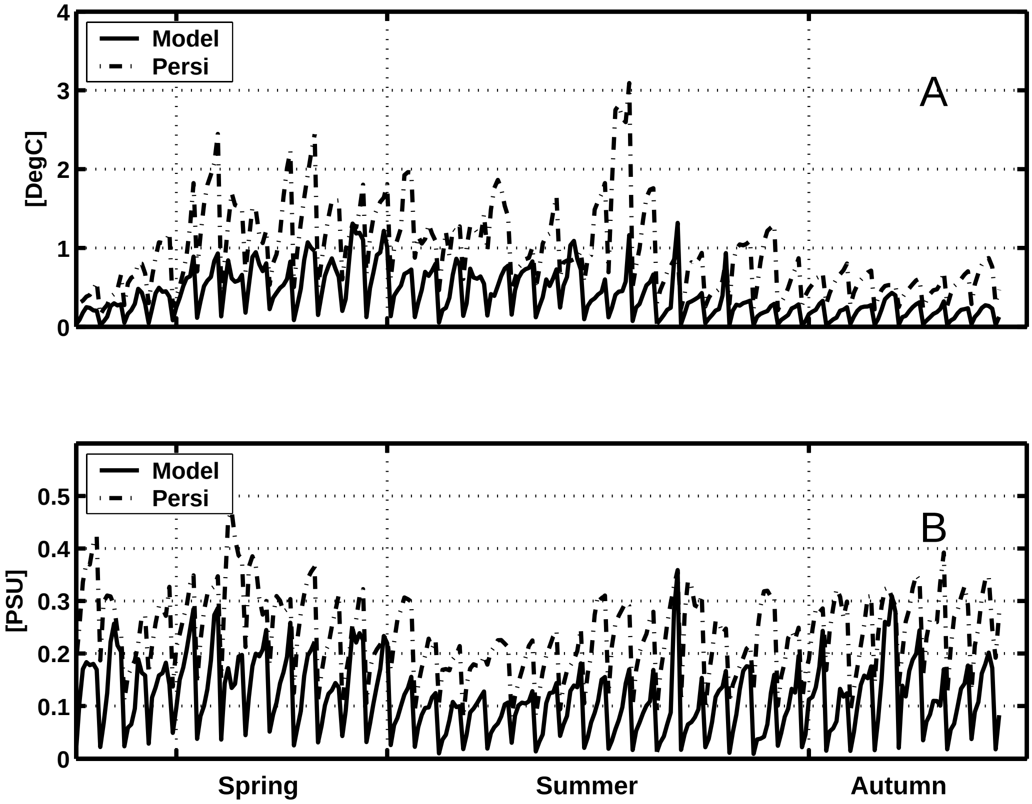

Figure 3.10 A: RMS time series between hindcasted, forecasted and persisted SST; B: RMS time series between hindcasted forecasted and persisted SSS.

3.5 Conclusions

The AREG forecasting system has been developed and tested to predict the hydrodynamic conditions of the Adriatic Sea. The choices made during the implementation phase make the system stable and robust, and allow long time integration without significant drift.

The model forecast accuracy, as well as hindcast quality, has been evaluated for the year 2003, the intensive data collection period for the ADRICOSM project.

The comparison between observed and predicted surface temperature suggests that errors in the forecast are mainly associated with atmospheric forcing inaccuracies and with the Po runoff forecast used in this system (the Po is held constant during the forecast). However, the RMS forecast error is always lower than the RMS persistence error and this justifies the usage of a numerical prediction system in the Adriatic Sea for short term forecasts.

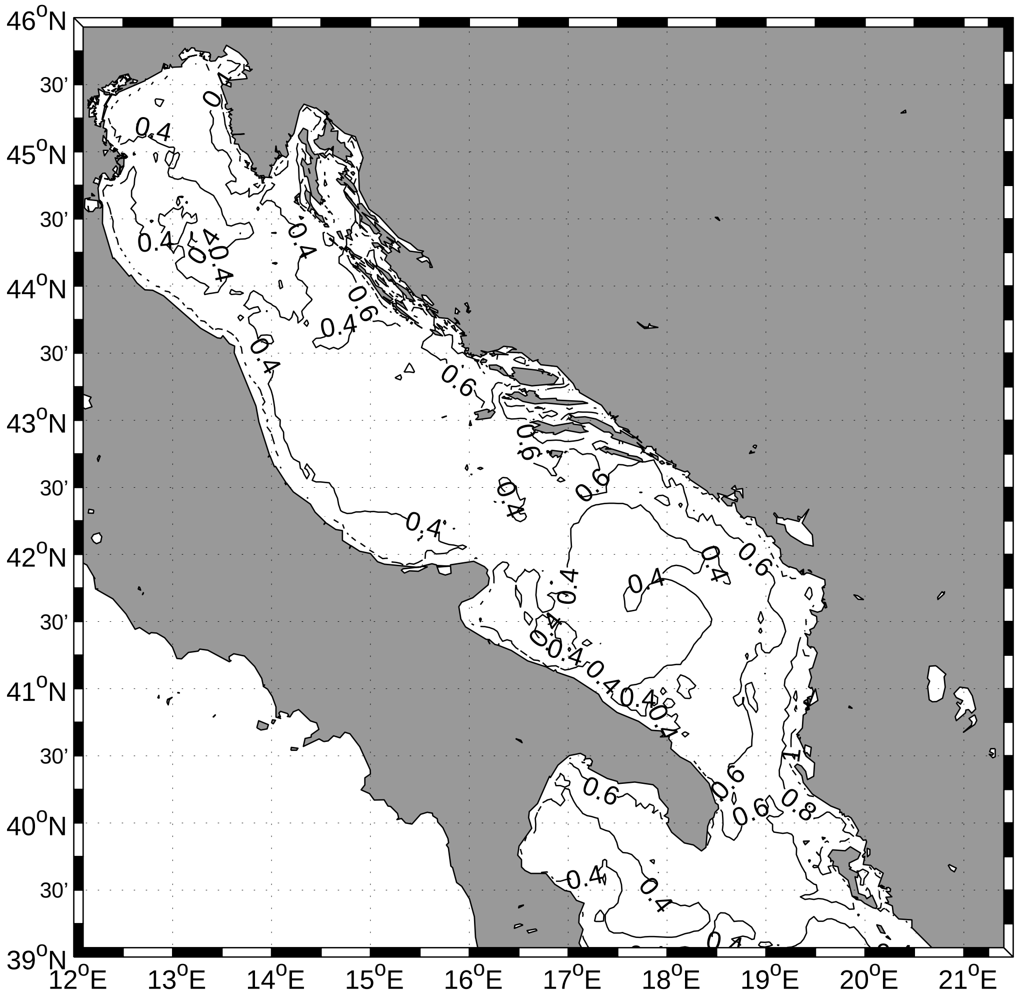

Figure 3.11 Horizontal map of the time averaged SST RMS error between hindcasted and forecasted SST. Units are °C.

The hindcast quality evaluation carried out using XBT data indicates a good agreement between observed and simulated temperature below a depth of 100m in all seasons. RMS hindcast error variability is particularly evident only in the upper layers reaching the maximum value in summer. Moreover the major hindcast deficiencies seem to be related to the inaccurate parameterization of the vertical mixing processes that mainly affect the hindcast quality during the stratified period. From an analysis of the horizontal distribution of the system

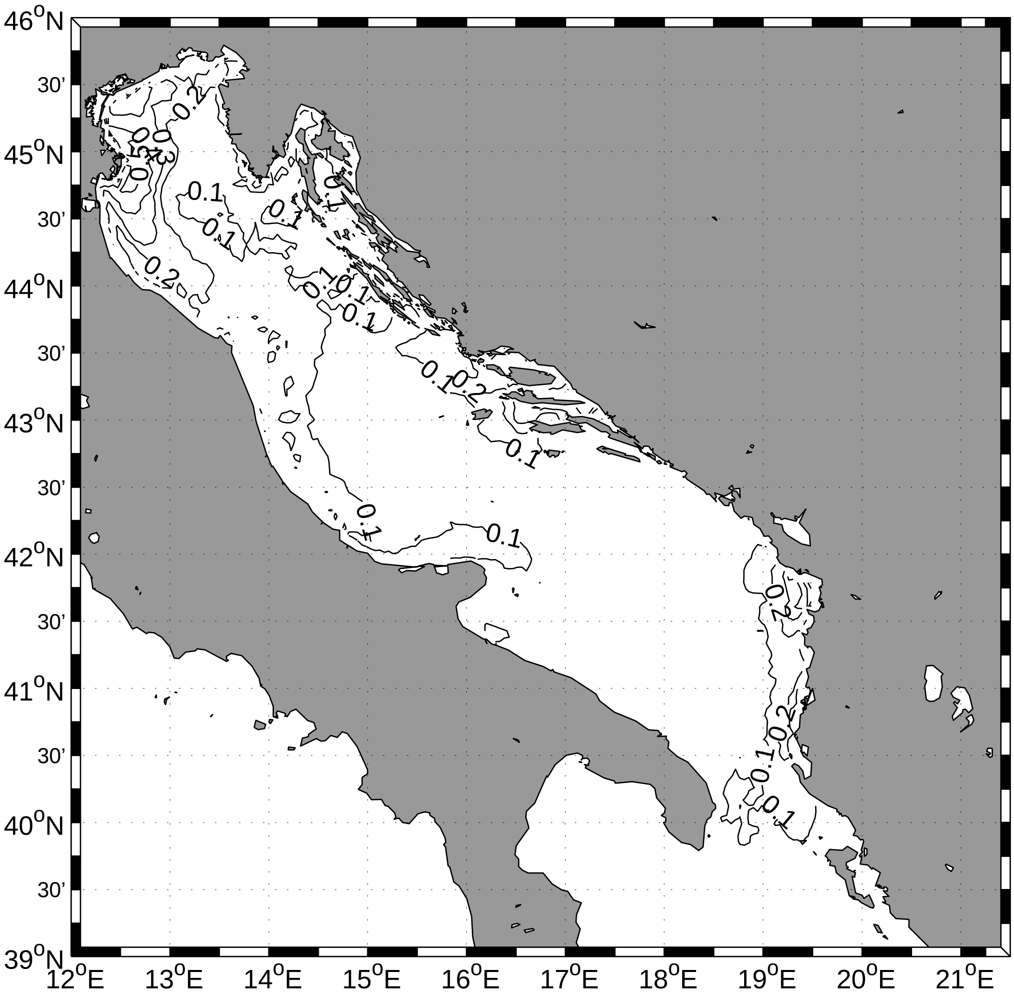

Figure 3.12 Horizontal map of the time averaged Sea Surface Salinity (SSS) RMS error between hindcasted and forecasted SSS. Units are PSU.

RMS error, and in agreement with the results of previous numerical studies in the Adriatic Sea (Zavatarelli and Pinardi, 2003), we can conclude that in the northernmost part of the basin, where the horizontal and vertical processes have smaller space-time scales, there is a need for higher horizontal resolution in the model.

The choice of a constant Po runoff value during the forecast obviously affects the forecast results in front of the Po Delta and along the WACC. It is found that the

Po runoff forecast and the inaccurate atmospheric forecast are the major source of errors in the northern Adriatic area as well as along the western and eastern sides of the Adriatic.

A data assimilation scheme suitable for the area is under development and will be soon implemented in the operational scheme (Grezio and Pinardi, 2005).

Chapter 4

Lateral Open Boundary Conditions for Nested Limited Area Model: Process selective approach

4.1 Introduction

This Chapter reviews the current approaches to the lateral open boundary conditions problem for nested regional circulation numerical models and proposes a new approach that considers temporal and spatial scales of the nested circulation structures.

The open boundary condition problem in numerical ocean and atmospheric modeling arises because it is practically unfeasible to model the global atmosphere/ocean with a spatial resolution capable to capture all types of circulation features. Global circulation models have coarse horizontal resolution and are used to simulate, predict and study the large scale dynamics using an appropriate parameterization for the subgrid-scale processes. Regional (Limited Area) models are, on the contrary, used in order to resolve smaller spatial and temporal scale processes. However, a modeling domain covering a limited area

must face the problem of an adequate representation of the influence of the dynamical processes occurring outside the modeled domain on its internal dynamics.
The treatment of the lateral open boundary conditions has been a difficult problem since the conception of regional models. Lacking an exact solution, practical implementations of open boundary conditions have been sought (Spall and Robinson, 1989). The effectiveness of the specification adopted has to be evaluated with respect to the characteristics of the studied problem and to the spatial and temporal scales of interest.
Even if the specification of prognostic variables on the open boundary is ill-posed in the mathematical sense, the effect of this ill-posedness could be irrelevant for the flow space and time scales of interest. Then, for any practical purpose, the boundary conditions specified can be considered viable. If, on the other hand, the boundary conditions generate or reflect waves that propagate inside the domain, or if they do not effectively transmit information into the interior, then they are not satisfactory (Spall and Robinson, 1989)
Since the problem is ill-posed, it is obvious that a unique solution for the open lateral boundary conditions problem cannot be sought and the adoption of a specific open boundary condition can be strongly dependent on the local implementation of the model. For this reason sensitivity experiments, investigating the role and the effect of different lateral open boundary conditions, play an important role in the choice of the open boundary solution.
This Chapter focuses on the definition of open boundary conditions for a regional circulation model nested into a wider and coarser model. The main aim is to achieve a solution that is as much as possible influenced by the assumptions done on the interacting time and space scales of the regional versus the coarser scale model.
In section 4.2 we provide an overview of the existing lateral boundary conditions and a derivation of a new process selective solution. This new solution is then implemented in a numerical model of the Adriatic Sea circulation that is described in section 4.3 and 4.4, along with the design of the sensitivity (to open boundary conditions) experiments Sections 4.5 and 4.6 offer the discussion and conclusions

respectively.

4.2 The lateral boundary condition formalism

A large number of open boundary conditions have been proposed in the scientific literature. Some of them are simple "relaxation" schemes that operate the nudging of the prognostic variables to a reference state within a specified region in the proximity of the open boundary with a return time arbitrarily fixed *a priori*. Others are based on the linearization of the primitive equations of motion, thereby providing a local solution based on a "reduced physics". A summary of these two kinds of boundary conditions is provided below together with the description of the new solution adopted here.

4.**2.1 Relaxation**

The relaxation scheme can be considered as the simplest solution to the lateral open boundary conditions problem. It consists of the addition of a Newtonian relaxation term to the model governing equations. With this technique, the model variables are driven towards a reference state originating from observations or from the results of a larger domain model. The most drastic way to do this is to impose:

$$\theta = \theta^{ext} \qquad \text{(eq. 4.1)}$$

on the boundary, i.e. to use a Dirichlet boundary condition. This approach is often used in the context of one-way nesting (Spall and Robinson, 1989), where the values of the model variables at the lateral open boundary are obtained trough a simple interpolation, in space and time, of the large scale model solutions. However, a major disadvantage of this method is that the outgoing information is totally determined by the external data irrespective of the internal solution. Therefore, due to possible inconsistencies between the external field and the interior model solution, part of the outgoing information could be reflected back into the domain.

To solve this inconsistency problem, often a space dependent relaxation term is applied to a portion of the domain in proximity of the open boundary. The return time is usually fast close to the boundary and progressively made slower proportionally to the distance from the open boundary. Trying to clarify the nomenclature we can define: a "*nudging term*", when the solution of the small domain is relaxed (or imposed, depending on the relaxation time) to the external data only along the boundary points; and a "*nudging layer*", when the relaxation is applied in a sub-region in proximity to the open boundary.

Another simple relaxation technique consists in artificially increasing the viscosity-diffusivity in the model interior area proximal to the lateral boundary. This region is often defined as a "*sponge layer*". The first obvious effect of this technique is to achieve a smoothed solution and suppress the reflection of disturbances from the boundary. A sponge layer can be implemented without the imposition of external data. If used together with a nudging layer the sponge layer has the interesting propriety to suppress the noise generated by the inconsistency between external and internal solutions (Palma and Matano, 1998).

4.2.2 Advective conditions

The advective conditions are also very simple conditions where the normal velocity at the boundary for the regional model velocity is used to advect out of the domain the θ field:

$$\frac{\partial \theta}{\partial t} + V_n \frac{\partial \theta}{\partial n} = 0 \qquad \text{(eq. 4.2)}$$

Where θ indicates a generic prognostic model variable, V_n is the normal velocity at the boundary and $\frac{\partial}{\partial n}$ the normal derivative to the boundary.

Thus, external data are advected inward at an inflow boundary and the interior data is advected outward at an outflow boundary. This simple solution have been often used (Palma and Matano, 2000, Zavatarelli and Pinardi, 2003 for example) in regional models for dynamical tracers (temperature and salinity).

4.2.3 Radiation Conditions

The most popular open boundary conditions are derived from the Sommerfield radiation equation (1949) that provides a simple and stable extrapolation of the interior solution on the open boundary. This condition is based on the assumption that the interior solutions approaching the open boundary propagate through it in a wave-like form according to:

$$\frac{\partial \theta}{\partial t} + C\frac{\partial \theta}{\partial x} = 0 \qquad \text{(eq. 4.3)}$$

Where θ indicates a generic prognostic model variable, C the phase speed and x the direction normal to the boundary. Here, the crucial issue is the proper formulation of the wave phase speed (C).

In special cases, it may be assumed that the dominant wave packet approaching the boundary originates from a distinct oceanic dynamics such as non-dispersive gravity waves (Chapman, 1985), but a more general approach was proposed by Orlansky (1976) who estimated the phase speed generically solving the eq. 4.3 by using interior values:

$$C = -\frac{\partial \theta}{\partial t}\left(\frac{\partial \theta}{\partial n}\right)^{-1}$$

With the requirement that $0 \le C \le \Delta x / \Delta t$. Then for limiting outflow conditions, maximum value of *C,* the interior value of the variable is imposed on the boundary point. Conversely, in the lower limit of *C* the value at the boundary can be prescribed using external information or simply persisting the previous time-step value. A two dimensional Sommerfield radiation was proposed by Raymond and Kuo (1984). The new derivation of the radiation condition takes into account both the normal and tangential component of the wave phase speed, giving:

$$\frac{\partial \theta}{\partial t} + C_x \frac{\partial \theta}{\partial x} + C_y \frac{\partial \theta}{\partial y} = 0 \qquad \text{(eq. 4.4)}$$

Where *x* and *y* are, respectively, the normal and the tangential direction to the boundary in local Cartesian coordinates. The two phase speeds are the projection of the oblique radiation, and as proposed by Orlansky for the 1D version, can be calculated from the surrounding interior grid point:

$$C_x = -\frac{\partial \theta}{\partial t} \frac{\partial \theta / \partial x}{(\partial \theta / \partial x)^2 + (\partial \theta / \partial y)^2}$$

$$C_y = -\frac{\partial \theta}{\partial t} \frac{\partial \theta / \partial y}{(\partial \theta / \partial x)^2 + (\partial \theta / \partial y)^2}$$

It has to be pointed out that the derivation of the two phase speeds makes sense only in a discrete form. The advantage resulting from this two dimensional calculation is the increased accuracy in the computation of the normal component of the phase speed, particularly when the direction of propagation has a significative tangential component.

The idea proposed by Orlansky (1976) also provides the basis for the dynamic open boundary algorithms accounting for and selectively treating inward and outward fluxes. Miyakoda and Rosati (1977) suggested to prescribe the external information at inflow points and use the wave equation in order to obtain the open boundary solution at outflow. The problem is that an inconsistency could be generated in a boundary point switching in time between the two regimes. A possible solution has been proposed by Marchesiello *et al* (2001) simply adding a nudging term to the eq. 4.4:

$$\frac{\partial \theta}{\partial t} + C_x \frac{\partial \theta}{\partial x} + C_y \frac{\partial \theta}{\partial y} = -\frac{1}{\tau}\left(\theta - \theta^{ext}\right) \qquad \text{(eq. 4.5)}$$

Where θ^{ext} represents the external data and τ is the time scale for the nudging. The authors suggest and test the idea to use different time scales for the nudging term depending on the inflow-outflow regime. According the authors the advantage obtained having a small relaxation also during the outflow regimes is to prevent possible model drift that can cause large differences between local model solution and external data.

4.2.4 Mass conservation equation: the Flather condition

An interesting and useful solution for the open boundary conditions has been proposed by Flather (1976). This condition can be classified as a special case of radiation condition. Here we discuss this solution separately from the other radiation conditions in order to emphasize its derivation and physical meaning.

The Flather (1976) condition originate from an attempt to simulate the principal semi-diurnal tide on the north-west European continental shelf using a limited area two dimensional numerical ocean model, The influence of different open boundary conditions on the internal solution was investigated. The more satisfactory results were obtained by prescribing a relationship between elevation and current at the open boundary arising from a combination of the continuity equation with a radiation condition. The problem proposed by Flather (1976) was not exactly a nesting problem but the solution proposed has been often applied also in this kind of problems. Here we derive the boundary condition equation used by Flather (1976) to introduce in the regional model the external model data from a nesting point of view. Equating the vertically integrated continuity equations of the nested (fine) and nesting (coarse) models we get:

$$\nabla \cdot \left[(H_c + \eta_c)\left(\vec{V}_{BTc}\right) \right] + \frac{\partial \eta_c}{\partial t} = \nabla \cdot \left[(H_f + \eta_f)\left(\vec{V}_{BTf}\right) \right] + \frac{\partial \eta_f}{\partial t} \qquad \text{(eq. 4.6)}$$

where H_c and H_f are the bottom topography of the coarse and fine resolution models respectively, $\vec{V}_{BTc}$ and $\vec{V}_{BTf}$ are the barotropic velocity for the coarse and fine resolution models and η_c and η_f are the surface elevations for coarse and fine model respectively. Assuming that the surface elevation tendency is only given by a gravity wave and using the dispersion relation to find the phase speed we can write:

$$\frac{\partial \eta}{\partial t} = -\nabla \cdot \left(\sqrt{gH}\eta\right)$$

Substituting in eq. 4.6 we obtain:

$$\nabla \cdot \left[(H_c + \eta_c)\left(\vec{V}_{BTc}\right) - \left(\sqrt{gH_c}\eta_c\right)\right] = \nabla \cdot \left[(H_f + \eta_f)\left(\vec{V}_{BTf}\right) - \left(\sqrt{gH_f}\eta_f\right)\right]$$

Integrating along the boundary and assuming $H_c = H_f = H$ and $\eta << H$ we can write:

$$\vec{V}_{BTf} = \vec{V}_{BTc} + \frac{\sqrt{gH}}{H}(\eta_f - \eta_c) \qquad \text{(eq. 4.7)}$$

Eq. 4.7 is the Flather (1976) lateral boundary condition equation. From a physical point of view the equation indicates that the differences between the two surface elevations are propagated out or in of the model domain with the speed of a gravity wave.

4.2.5 The scale selective lateral boundary condition

As discussed in the introductory section the use of Limited Area Models derive from the necessity to resolve effectively the small scale processes that are not adequately resolved in the coarser model based data-sets. This necessarily implies an inconsistency between the regional model solution and the external data. For a one-way nesting the inconsistence is amplified if the external data are averaged in time and supplied with a given frequency that is defined a priori.

For instance, in a time averaged field all the processes with a frequency higher than the time window, used in computing the mean, are filtered out. As a consequence the implementation of an open boundary condition based on physical processes, such as that proposed by Flather (1976) should take into account that the limited area model solution and the external data (model or observation based) do not represent the same physics.

This could generate numerical instability or at least the insurgence of numerical noise in the area closest to the boundary. In order to avoid this we suggest a simple solution based on the splitting of the nested model internal solution into two different parts: the first containing the physics represented in the external and/or coarser model, the second containing the processes characterized by small scales. For the diagnostic variables involved in eq. 4.6 we can apply this decomposition writing:

$$\eta_f = \eta_f^{'} + \eta_f^{''}$$

and

$$\vec{V}_{BTf} = \vec{V}_{BTf}^{'} + \vec{V}_{BTf}^{''}$$

Where $\eta_f^{'}$ and $\vec{V}_{BTf}^{'}$ indicate the part of the regional model surface elevation and barotropic velocity resolved in the external fields and $\eta_f^{''}$ and $\vec{V}_{BTf}^{''}$ indicate the part of the surface elevation and of the barotropic velocity not resolved in the external data. For instance we can think to $\eta_f^{'}$ and $\vec{V}_{BTf}^{'}$ as low time frequency components and $\eta_f^{''}$ and $\vec{V}_{BTf}^{''}$ as the high frequency-small scale components. The definition of the frequency discrimination between large and small scales can be based on a simple spectral analysis of the external data used for the specification of the open boundary condition or on wavelets.

To simplify the following treatment we will refer to the low-frequency-large scale component as the "global" field and to the high frequency-small scale component as the "regional" field. Splitting eq. 4.6 in left hand side (*l.h.s*) and right hand side *(r.h.s)* and rewriting the *r.h.s* taking into account the decomposition we obtain:

$$l.h.s = \nabla \cdot \left[(H_f + \eta_f^{'} + \eta_f^{''}) \left(\vec{V}_{BTf}^{'} + \vec{V}_{BTf}^{''} \right) \right] + \frac{\partial \eta_f^{'}}{\partial t} + \frac{\partial \eta_f^{''}}{\partial t} \qquad \text{(eq. 4.8)}$$

Following the idea suggested before only the global component of the *r.h.s* of eq. 4.8 should be forced to be equal to the *l.h.s*. obtaining:

$$\nabla \cdot \left[(H_c + \eta_c) \left(\vec{V}_{BTc} \right) \right] + \frac{\partial \eta_c}{\partial t} = \nabla \cdot \left[(H_f + \eta_f^{'}) \vec{V}_{BTf}^{'} \right] + \frac{\partial \eta_f^{'}}{\partial t} \qquad \text{(eq. 4.9)}$$

Partially following the procedure suggested by Flather (1976) we can find a general solution assuming

$$\frac{\partial \eta_f^{'}}{\partial t} = -\nabla \left(\vec{C}^{'} \eta_f^{'} \right)$$

$$\frac{\partial \eta_C}{\partial t} = -\nabla \left(\vec{C}^{'} \eta_C \right)$$

Where $\vec{C}^{'}$ is the phase speeds for the global field that is equal between the coarse scale and the global component of the nested model field. The phase speed can be obtained by assuming the dispersion relationship or, as suggested by Orlansky (1976), solving the wave equation using the interior values. Assuming $H_c = H_f = H$ and substituting the general formulation done for the tendency of the global components of the surface elevation in eq. 4.9 we obtain:

$$\nabla \cdot \left[(H + \eta_c)\left(\vec{V}_{BTc}\right) \right] - \nabla \cdot \left(\vec{C}^{'} \eta_c \right) = \nabla \cdot \left[(H + \eta_f^{'}) \vec{V}_{BTf}^{'} \right] - \nabla \cdot \left(\vec{C}^{'} \eta_f^{'} \right)$$

Solving for $\vec{V}_{BTf}^{'}$ we obtain the solution for the low frequency part of the nested model barotropic velocity:

$$\vec{V}_{BTf}^{'} = \frac{H + \eta_c}{H + \eta_f^{'}} \vec{V}_{BTc} - \frac{\vec{C}^{'}}{H + \eta_f^{'}} \left(\eta_c - \eta_f^{'} \right) \qquad \text{(eq. 4.10)}$$

That is a generalization of the Flather (1976) condition. Assuming $H_c = H_f = H$ and η<< H we obtain also:

$$\vec{V}_{BTf} = \vec{V}_{BTc} + \frac{\vec{C}^{'}}{H} (\eta_f^{'} - \eta_c) \qquad \text{(eq. 4.11)}$$

That is exactly the Flather equation with the only difference that here the phase speed is not fixed a priori.

Once obtained the open boundary condition for the global component of the nested model, it is possible to decide which open boundary condition for the regional component should be applied. The simplest solution can be obtained forcing to zero all the terms in eq. 4.8 that are not used to derive the global component solution:

$$\nabla \cdot \left[\left(H + \eta_f \right) \vec{V}_{BTf}^{''} + \eta_f^{''} \vec{V}_{BTf}^{'} \right] - \nabla \left(\vec{C}^{''} \eta_f^{''} \right) = 0 \qquad \text{(eq. 4.11)}$$

In equation 4.11 we assumed again, that wave motion is dominant in order to explain the tendency of the regional component of the surface elevation. Solving for $\vec{V}_{BTf}^{''}$ we obtain the solution for the high frequency part of the barotropic velocity:

$$\vec{V}''_{BTf} = \vec{C}'' \frac{\eta''_f}{H+\eta_f} - \vec{V}'_{BTf} \frac{\eta''_f}{H+\eta_f} \qquad \text{(eq. 4.12)}$$

The problem related to this relationship is a consequence of the simplification done eliminating the divergence in eq. 4.6. In this case the value for the regional component of the barotropic velocity at the boundary does not depend on horizontal gradient but only on local values. In the Flather condition this problem is, in same way, mitigated by the last term in the equation that is the difference between the two surface elevations and can be seen as a horizontal gradient obtained using internal and external solutions. As a consequence the physical mean of the relationship reported in eq. 4.12 is not clear.

Another solution can be obtained using a radiation condition for the regional component of the barotropic velocity normal to the boundary with a priori fixed phase speed or interactively computed using the interior solution.

4.2.6 A special case: Rigid lid-free surface nesting (tested)

A reasonable approximation at mid- and high-latitudes for general circulation models is the rigid lid approximation. This approximation filters out the fast barotropic gravity waves by setting the time variation of the free surface elevation equal to zero. This is obviously not acceptable in the area where this filtered waves play an important role in determining the local dynamics. For a free surface model nested within a rigid lid coarser model eq. 4.6 becomes:

$$\nabla \cdot \left(H\vec{V}_{BTc}\right) = \nabla \cdot \left[(H+\eta_f)\vec{V}_{BTf}\right] + \frac{\partial \eta_f}{\partial t} \qquad \text{(eq. 4.13)}$$

note that the *l.h.s* of eq. 4.6 is now the vertically integrated continuity equation for a rigid lid model. For this special case the Flather (1976) equation assumes the form:

$$\vec{V}_{BTf} = \vec{V}_{BTc} + \frac{\sqrt{gH}}{H}\eta_f \qquad \text{(eq. 4.14)}$$

For the eq. 4.14 there is always the problem pointed out before for eq. 4.12, i.e., the bartropic velocities are changes simply by the free surface height sign and not by the gradient.
Considering again the scale decomposition described above we obtain the solution for the global component of the barotropic velocity normal to the boundary:

$$\vec{V}'_{BTf} = \frac{H}{H+\eta'_f}\vec{V}_{BTc} - \frac{\vec{C}'}{H+\eta'_f}\eta'_f \qquad \text{(eq. 4.15)}$$

or

$$\vec{V}_{BTf} = \vec{V}_{BTc} - \frac{\vec{C}'}{H}\eta'_f \qquad \text{(eq. 4.16)}$$

Eq. 4.16 is obtained using the Flather (1976) assumption on H and η. For the regional component of the barotropic velocity the boundary condition is the same of the previous case (eq. 4.12) and the considerations done above remain valid.
Eq. 4.15 has been used in Zavatarelli *et al.* (2002) and Zavatarelli and Pinardi (2003) but with another simplification: C is considered to be zero, i.e., the fast barotropic gravity waves of the nested model are filtered out by considering their tendency equal to zero at the boundary.

4.3 Model configuration for lateral boundary conditions nesting

The numerical model used to test the different boundary conditions performance is based on the Princeton Ocean Model (POM, Blumberg and Mellor, 1987) as described in Chapter 2.
Fig. 4.1 illustrates the modeling domain together with a schematic of the main

circulation patterns. At the open boundary (green line in Fig. 4.1) the model is off-line one way nested with the operational 1/8° resolution model of the entire Mediterranean (Demirov *et al*. 2003), witch provides the daily averaged temperature, salinity and velocities fields used for open boundary specification. Data from the nesting models have been interpolated on the open boundary of the nested one.

For the velocities fields an interpolation constraint has been used (Pinardi *et al*, 2003). This constraint allows the total transport to be maintained after interpolation. The two models resolve different processes having different horizontal resolution but also different physics, for instance the nesting model is a rigid lid model while the nested one is a free-surface model. Both the models interactively compute the surface fluxes using the atmospheric fields provided by ECMWF (European Centre for Medium range Weather Forecast) analysis (Zavatarelli and Pinardi, 2003, Chapter 2). In the regional model the water flux is parameterized as salt flux, as a consequence no volume (freshwater) flux is imposed in the model.

A nudging layer has been implemented adding a term to the right-hand side (r.h.s.) of the prognostic equations for tracers, as follows:

$$\frac{\partial \gamma}{\partial t} = r.h.s. - \frac{1}{\Gamma}\left(\gamma - \gamma^{OGCM}\right) \qquad \text{(eq. 4.17)}$$

Where γ indicates either temperature or salinity. Γ varies linearly from 30 days at the boundary to 10 years at a normal distance from the open boundary of approximately 90 km. Also a sponge layer has been used in an area extending for approximately 50 km north of the open boundary where the viscosity/diffusivity coefficients resulting from the Smagorinsky (1993) algorithm are linearly increased arriving to be double at the boundary.

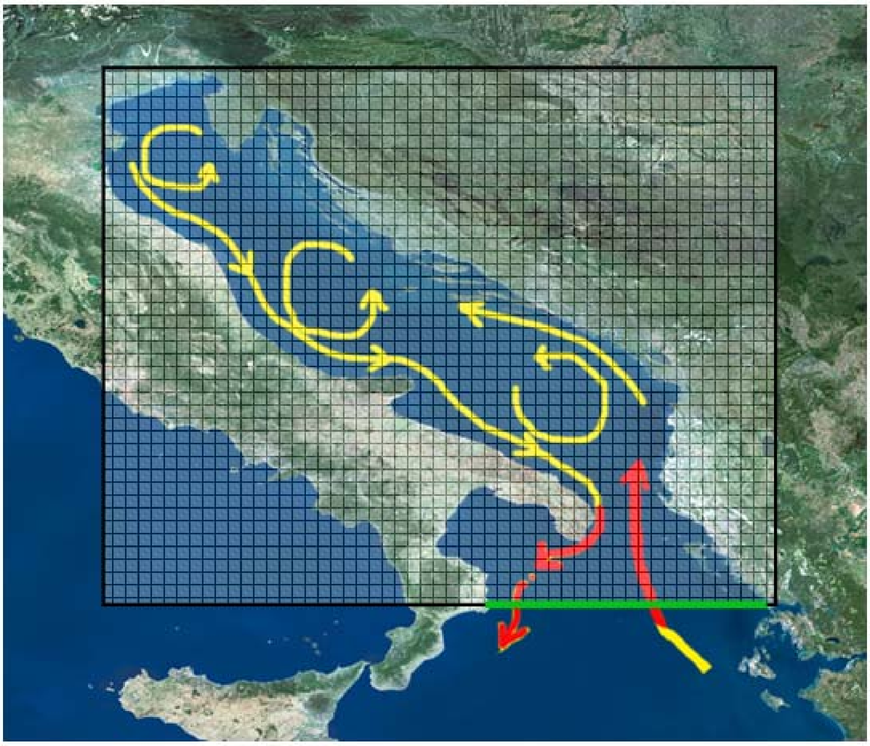

Figure 4.1 Schematic map of the Adriatic Sea circulation. The green line indicates the model southern boundary. The yellow lines indicate the permanent (with seasonally variability) circulation pattern. The red lines indicate the current directly affected by the lateral boundary conditions implementation.

The simulations spans the period from January 1999 to the end of 2001. As initial conditions the results of a climatological implementation have been used (Zavatarelli and Pinardi, 2003) Simulation for year 1999 has been performed using a single set of boundary conditions. Year 2000 is considered as a spin up period for the different boundary condition sets and the results of the simulation for year 2001 are analyzed.

4.4 Experiments design

Three different sets of boundary conditions have been tested and the results compared between models and with available observations.

In all the experiments we used a zero gradient boundary conditions for the surface elevation. The first experiment has been carried out by imposing barotropic and total velocities from the coarse resolution model (eq. 4.1) and using the advection scheme in eq. 4.2 for temperature and salinity. The second experiment has been carried out using for all the prognostic variables the 2D version of the radiation condition as suggested by Marchesiello *et al.* (2001) (eq. 4.5). The nudging term time scale in eq. 4.5 was chosen to be 30 days in the outflow regime and the external field imposed at inflow.

The third experiment has been carried out using the same boundary conditions set of the first experiment with the only exception of the barotropic velocity where we tested the process decomposition described in the previous section. In order to obtain the global and regional fields separation for the surface elevation, the global component is set equal to the η_g derived from the sea surface pressure formulation of rigid lid models (Pinardi *et al*. 1995). Thus the free surface decomposition is

$$\eta_f = \eta_f'' + \eta_g$$

Eq. 4.12 has then been used to solve the regional component by imposing zero tendency for the regional part of the surface elevation, i.e.:

$$\vec{V}_{BTf}'' = -\vec{V}_{BTf}' \frac{\eta_f''}{H + \eta_f} \qquad \text{(eq. 4.18)}$$

In Table 4.1 the different boundary conditions set-up are summarized.

The nested model has an explicit free-surface, therefore, in order to ensure volume conservation an additional constraint to the barotropic velocity has been added in the second and third experiments. For the first experiment, being the nesting model a rigid-lid model, zero transport in ensured along a boundary by the interpolation constraint.

For experiments 2 and 3 in Table 4.1 a correction factor for the barotropic velocities normal to the lateral boundary has been defined as follows:

$$\vec{V}_{tr} = \frac{1}{S}\int_{L} \vec{V}_{BTf}\left(H+\eta\right)dL \qquad \text{(eq. 4.19)}$$

Where S is the total surface of the lateral boundary and L the perimeter. The barotropic velocity has been corrected after the computation of the boundary values as follows:

$$\vec{V}_{BTfnew} = \vec{V}_{BTf} - \vec{V}_{tr} \qquad \text{(eq. 4.20)}$$

	Exp1	**Exp2**	**Exp3**
U,V	*Imp.*	*2D rad. + nud.*	*Freq. decomp.*
u,v	*Imp.*	*2D rad. + nud.*	*Imp.*
T,S	*Adv. Sche,*	*2D rad. + nud.*	*Adv.Sche,*
Nudging layer	*90 km with τ linearly varying from 10 years to 1 month*		
Sponge layer	*50 km τ linearly varying from 1 to 2.4*		

Table 4.1 The boundary conditions set-up used in the three experiments. U and V indicate the barotropic velocity, u and v the total velocity and T and S indicate Temperature and Salinity respectively.

4.5 Results and discussion

In this section we present the assessment of the results obtained by using the different boundary conditions.

The difference between the experiments has been studied by means of the root mean square (RMS) difference values. Two different sets of observations have been used to compute the RMS error: XBT (Expendable Bathythermograph) data from the MFS (Mediterranean Forecasting system) project (Pinardi *et al.*, 2003); and CTD (Conductivity-Temperature-Depth) data from NATO-SACLANT ADRIA01 cruise.

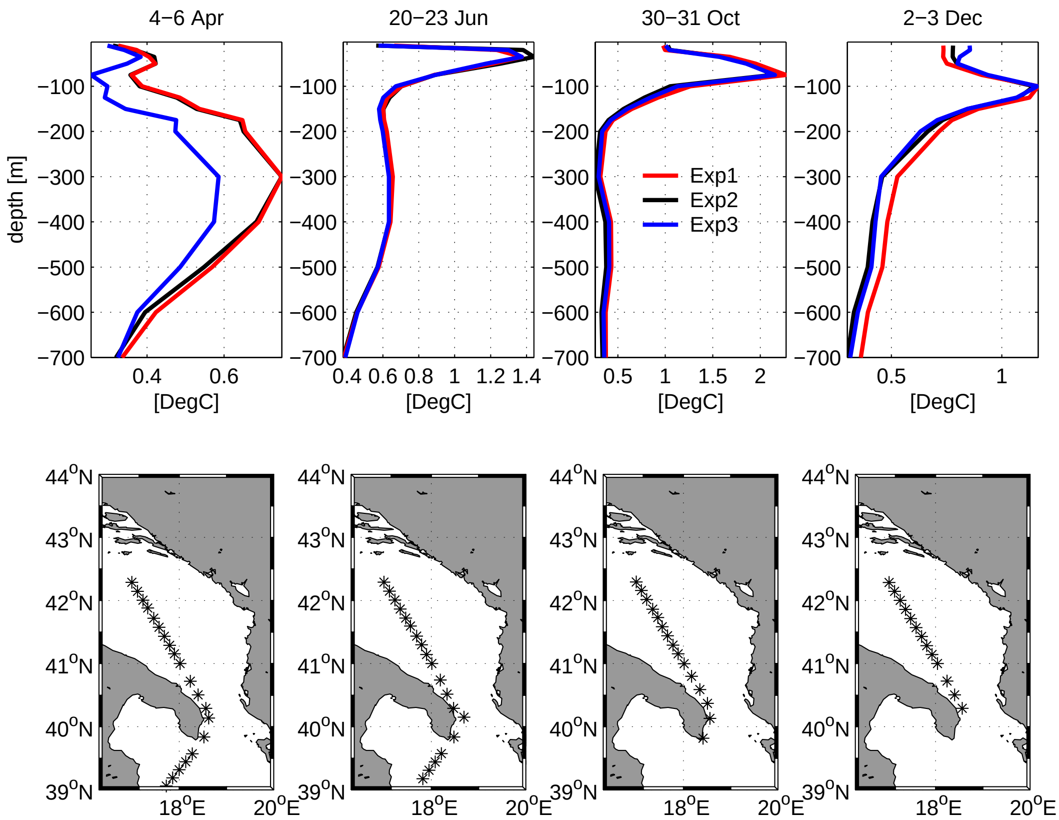

Figure 4.2 Vertical profiles of RMS error and XBT cruises tracks are given. Each upper subplots show the vertical profiles of RMS error for the different sampling date. Red lines indicate Exp1, dark lines indicate Exp2 and blue lines indicate the Exp3. The lower subplots show the position of the sampling for each cruise.

Four different XBT cruises have been performed in year 2001: 4-6 April; 20-23 Jun; 30-31 October and 2-3 December. In Fig. 4.2 the temperature RMS error vertical profiles of the different experiments for each cruise are shown together with the corresponding sampling positions. The major difference between the three experiments appears in April all along the water column and during December near the surface and in the bottom layers. In June and October the different boundary conditions tested seem to have similar behavior in terms of

RMS error. During April a remarkable improvement derives from the process-selective boundary condition while the other two lateral conditions schemes give the same error.

To show the difference between fields in the three experiments we show the barotropic velocity and the surface elevation. This variables have been averaged over the period spanned by the cruises and are shown as explained in Fig. 4.3. For this comparison only the Southern part of the Adriatic basin is shown being the area where the observations have been collected and the major differences between the three experiments can be traced.

A	D
B	E
C	F

Figure 4.3 Schematic layout of the maps reported in Fig. 4.4 Fig. 4.5 Fig. 4.6 and Fig. 4.8. Panels A B and C barotropic velocity for the Exp1 Exp2 and Exp3 respectively. Panels D E and F surface elevation field for Exp1 Exp2 Exp3 respectively.

In Fig. 4.4 the experiment results corresponding to the April cruise are shown. The barotropic velocity fields for the Exp1 and Exp2 along the XBT track have similar patterns, while the major differences are in the small structures developing in the Otranto Channel and at the borders of the Southern Adriatic cyclonic gyre.

This gyre is a permanent feature of the Adriatic circulation (Artegiani at al. 1997 a and b). In both experiments the circulation near the open boundary has a cyclonic character and is affected by numerical noise in areas where outflow occurs. The Exp3 barotropic velocity differs from the other two. In the outflow area close to the open boundary, there is no numerical noise. The SAd gyre is closer to the coast with respect to the other two experiments. The different spatial configuration of the circulation close to the open boundary is emphasized when comparing the surface elevation fields. In Exp1 and Exp2 the cyclonic structure is totally asymmetric extending in a SW-NE direction, while in Exp3 its centre position is characterized by the westernmost position.

Analyzing the model results for the June and October periods, we reach the same conclusions that we did by looking at the RMS error. For this reason only the October fields are reported in Fig. 4.5. The major differences between the three experiments along the XBT track are in the position and intensity of the SAd gyre. In Exp1 this structure has a large spatial extension and, close to its northern margin, a well defined small anticyclonic gyre appears. In Exp2 and Exp3 results the SAd gyre has a reduced spatial extension, but a stronger intensity and the anticyclonic gyre is absent. Interesting differences are observed in the inflow area at the open boundary, where the process decomposition boundary condition (Exp3) seems to allow a stronger propagation of the inflow into the model interior. A strong horizontal gradient characterizes the western side of the SAd gyre in the sea surface elevation. In Exp2 and Exp3 the gradient is less intense than in Exp 1. The spatial configuration reproduced in Exp1 probably allows the formation of the small anticyclonic gyre not present in the two other experiments.

In Fig. 4.6 the results of the different experiments for the December period are

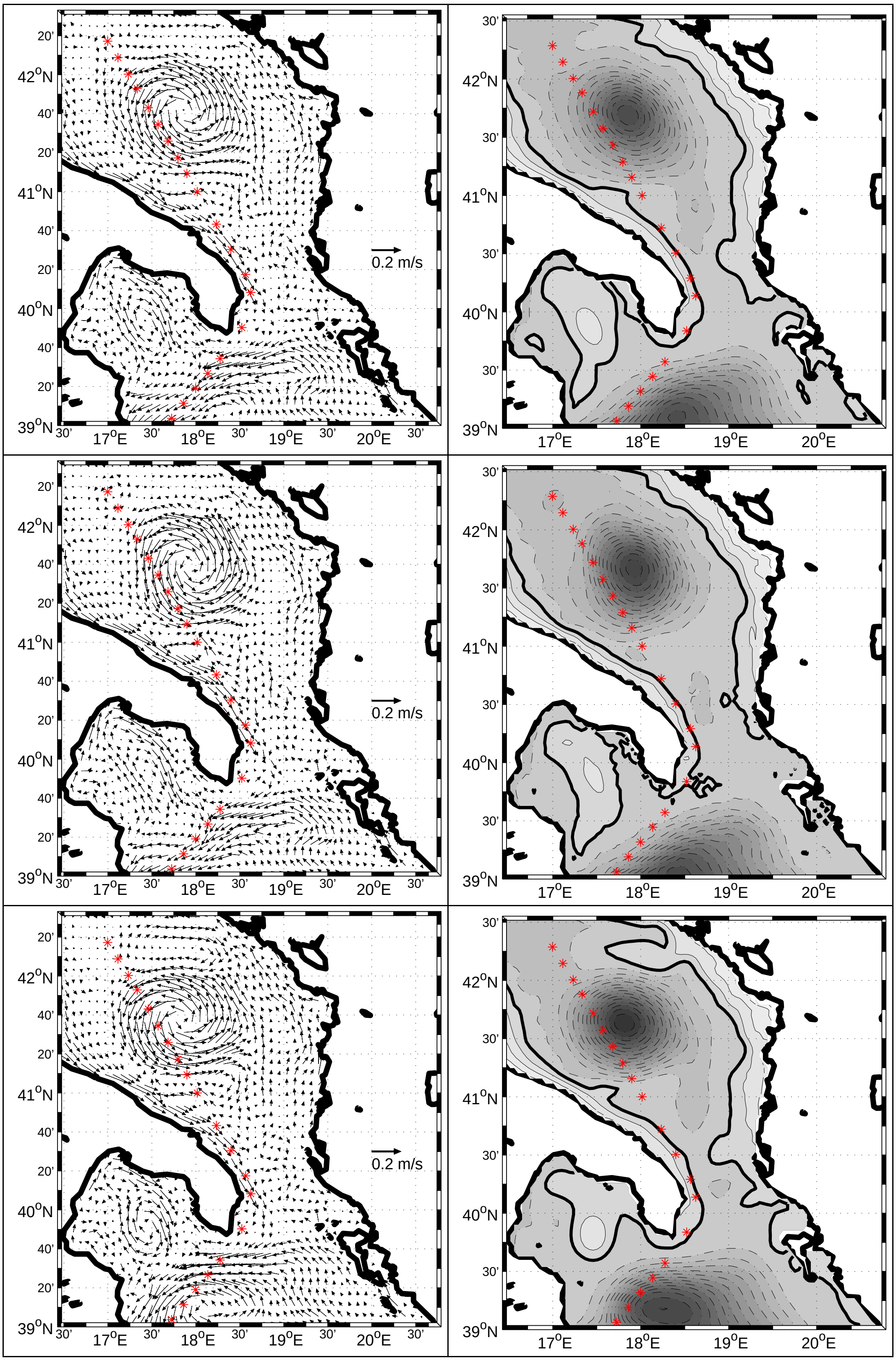

Figure 4.4 Horizontal maps of barotropic velocity and surface elevation for the three experiments. The fields have been obtained averaging the model results from 4 to 6 April.

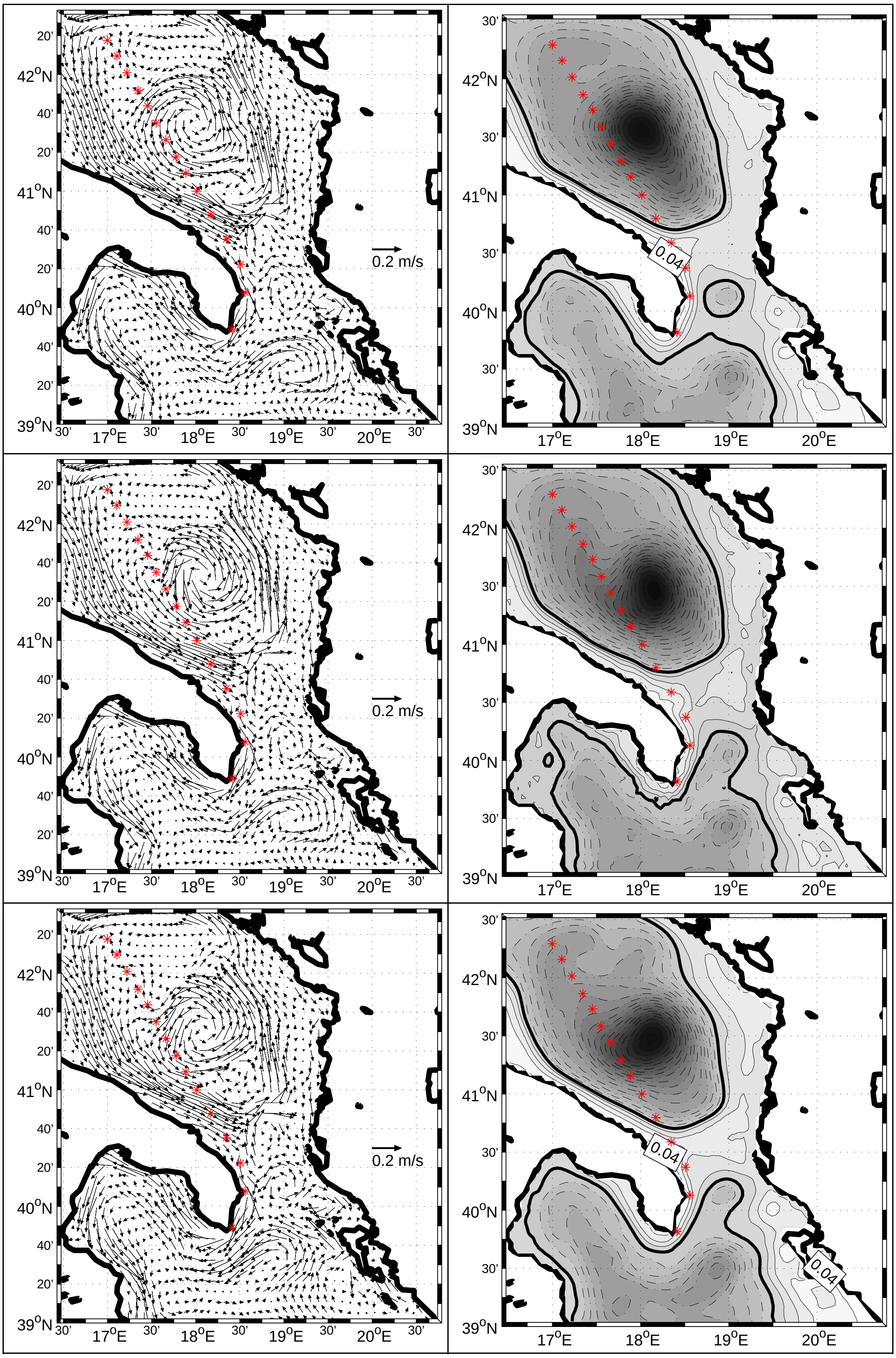

Figure 4.5 Horizontal maps of barotropic velocity and surface elevation for the three experiments. The fields have been obtained averaging the model results from 30 to 31 October.

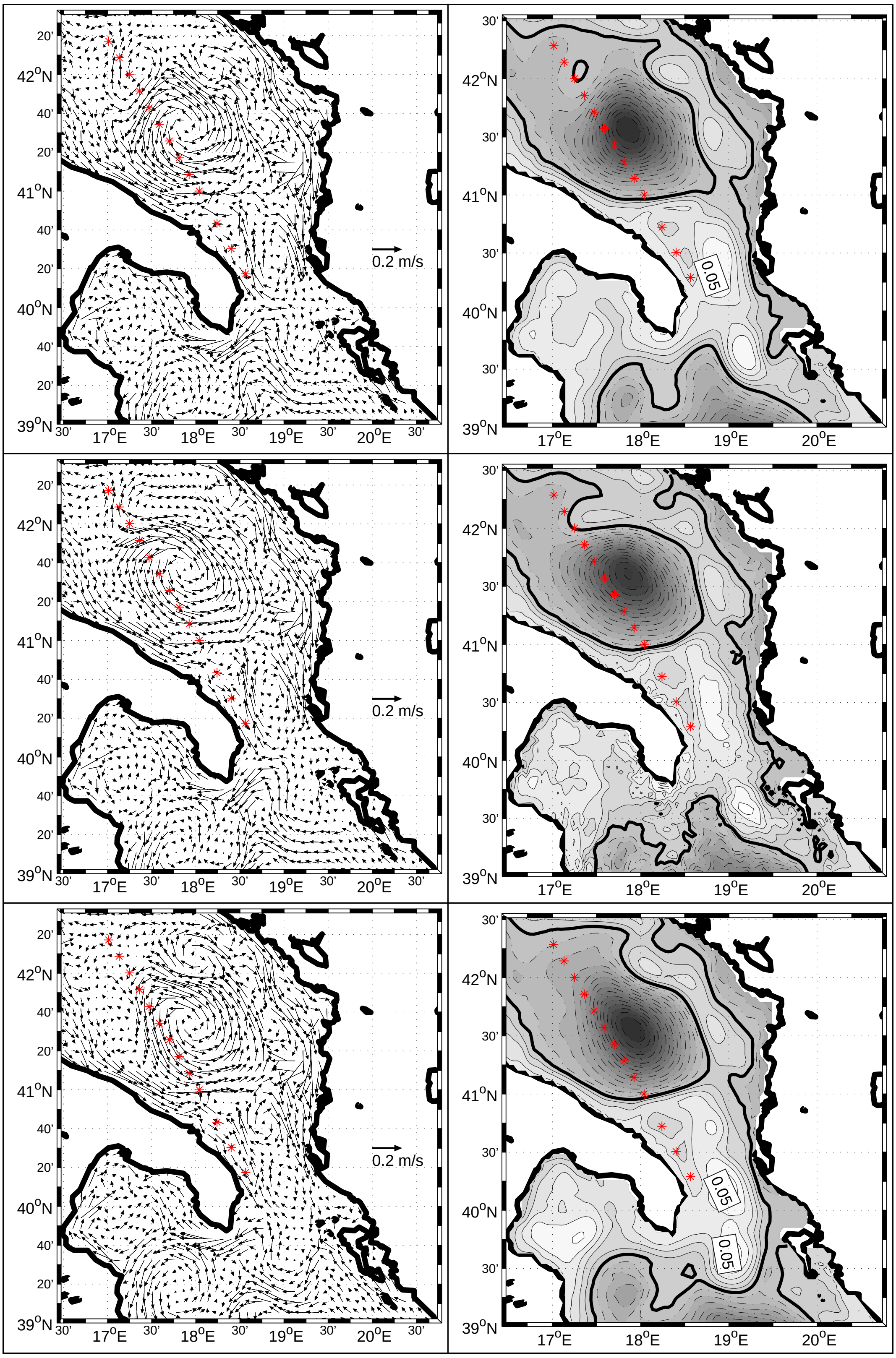

Figure 4.6 Horizontal maps of barotropic velocity and surface elevation for the three experiments. The fields have been obtained averaging the model results from 2 to 3 December.

shown. Also during December differences are evident in the position and intensity of the SAd gyre. In this period and in all experiments many small cyclonic and anticyclonic structures encircle the SAd gyre. Their number and intensity, however, are strongly affected by the boundary conditions. In Exp1 two anticyclonic gyres are on the eastern side of the SAd. In Exp2 the same two structures are almost connected forming a unique large feature, while in Exp3 the two anticyclones are smaller and almost three.
Strong differences are evident comparing in Fig. 4.6 the three surface elevation fields South of the Otranto Strait. A strong noise characterize Exp2 (2D radiation) results, even if this noise does not seem to affect the circulation in the Southern Adriatic cyclonic circulation. This is confirmed also by the RMS error profile reported in Fig. 4.2 which is not very different between Exp2 and Exp3
In Fig. 4.7 the temperature and salinity RMS error vertical profiles of the different experiments for a CTD cruise are shown together with the corresponding sampling positions. Along this section the boundary conditions set-up does not affect the structure of the RMS vertical profiles that seems determined by other model parameterizations. The major differences in terms of RMS error are evident in the temperature error profiles. Exp3 gives better results in the upper layers, with respect to the two others experiments, but worse results from 300 to 600 m depth.
The barotropic circulation, Fig. 4.8, for Exp1 is characterized by a SAd gyre having an N-S extension and a small cyclonic gyre on the northern side. In Exp2 the SAd mainly extends in the W-E direction, enhanced in the surface and the small cyclonic gyre almost disappears. The SAd gyre reproduced by Exp3 is the most symmetric of all of them. The surface elevation fields again show evidence that in the Exp2 the numerical noise is largest.

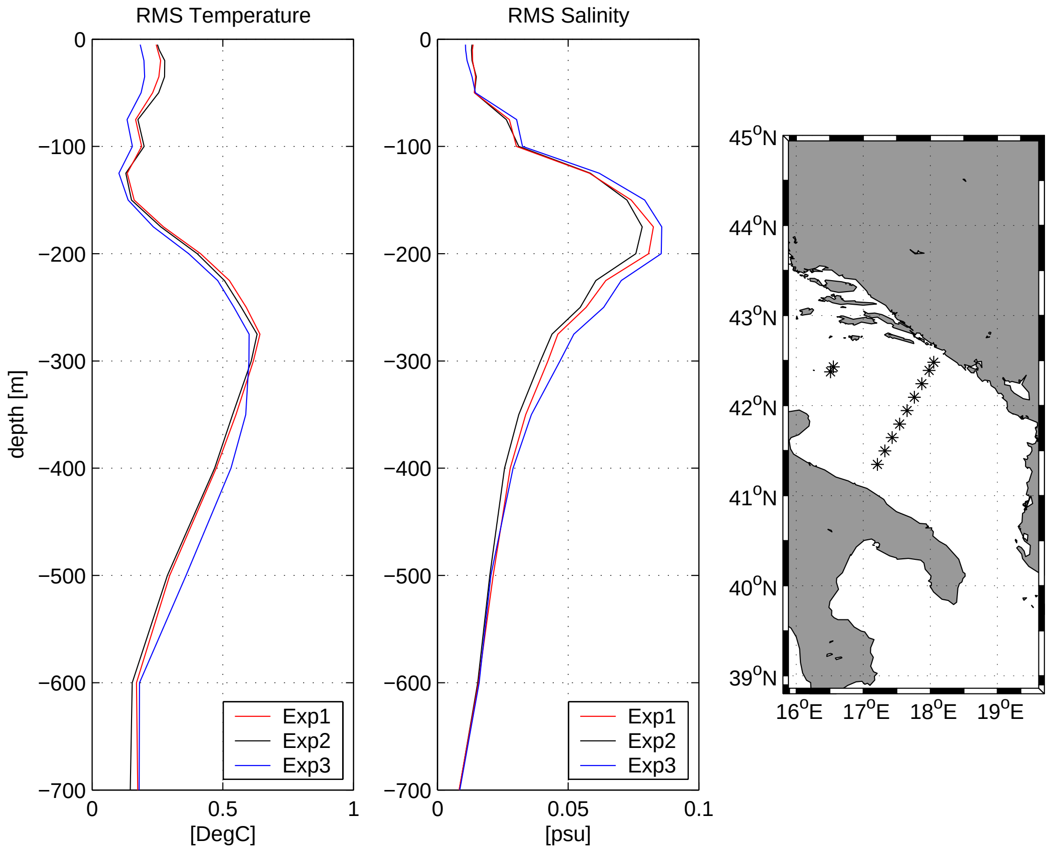

Figure 4.7 Vertical profiles of RMS error and CTD sampling positions are given. The left panel shows the vertical profiles of temperature RMS error for the different experiments. The central panel shows the vertical profiles of salinity RMS error for the different experiments. The right panel shows the samplings positions. Blue lines indicate Exp1, red line indicate Exp2 and dark line indicate the Exp3.

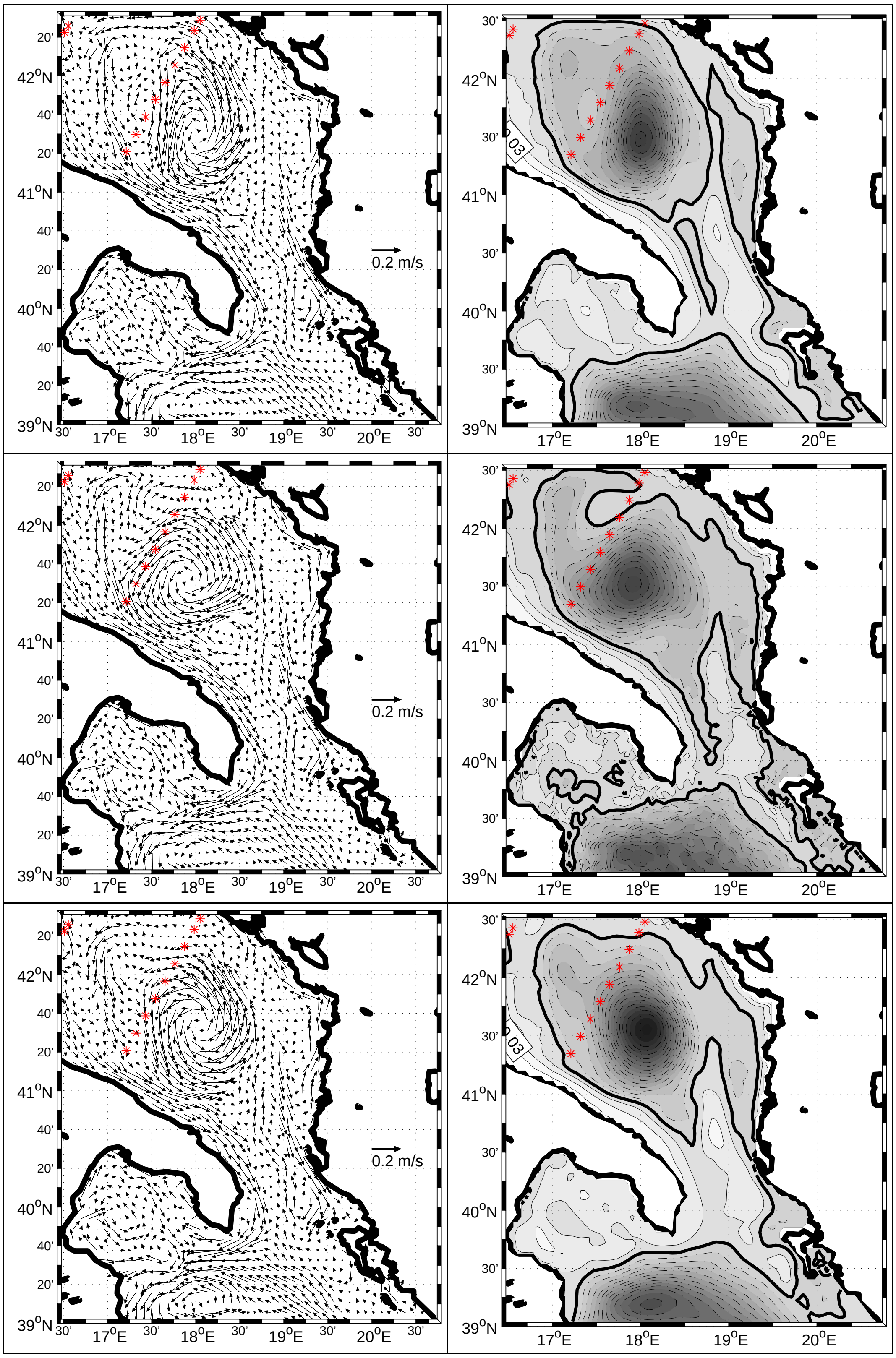

Figure 4.8 Horizontal maps of barotropic velocity and surface elevation for the three experiments. The fields have been obtained averaging the model results from 5 to 6 February.

4.7 Summary and Conclusions

The most commonly used lateral open boundary conditions were presented in Section 4.2 together with the derivation of a new scale selective lateral boundary condition.

We derived the Flather (1976) solution in order to use the derivation for the application of the process decomposition approach proposed. One of the main conceptual problems in the Flather (1976) lateral boundary conditions is the simplification done in its derivation. This problem is emphasized in all the cases where no external data are available for the surface elevation.

A system composed by a coarse rigid lid, covering the entire Mediterranean Sea, and a fine resolution free surface model, reproducing the Adriatic Sea, has been used in order to evaluate the different boundary condition performance. Different boundary conditions have been implemented but only the ones that give stable solutions have been considered in this work. The simple 1D version of the radiation and the Flather (1976) conditions cause the insurgence of numerical instability close to the open boundary.

Three test cases have been presented in Section 4.4 and the results discussed in Section 4.5. The simple condition for barotropic and total velocity with an advection scheme for the tracers (Exp1), the two-dimensional version of the radiation condition as proposed by Marchesiello *et al*. (2001) for all the model variables (Exp2), and the scale decomposition approach for the barotropic velocity, the imposition of the total velocity and an advection scheme for the tracers (Exp3).

The boundary conditions parameterization affects the model solution also in the interior domain in terms of position and intensity of the reproduced structures. These differences are amplified during specific periods. The Exp2 (2D radiation) solution appears affected by numerical noise in the area close to the open boundary also if this numerical disturbance seem not affect the interior solutions. Especially during April the process decomposition approach, applied to the Flather (1976) equations, gives better results in terms of RMS error between model results and observations. The future work will be directed toward the testing of the process decomposition for other sets of boundary conditions.

Chapter 5

Interannual variability hindcast experiments of the Adriatic Sea circulation (2000-2002)

5.1 Introduction

Motion in the ocean occurs at a variety of temporal and spatial scales, from molecular diffusion processes (10^{-6} m) to large scale oceanic gyres and currents (10^{7} m). A fundamental horizontal length scale in fluids that are affected by both gravity and rotation is the Roosby radius of deformation. It is the length scale at which rotation effects become as important as buoyancy effects, and in a baroclinic stratified fluid is given by the ratio between the wave speed of the n^{th} baroclinic mode and the Coriolis parameter. The baroclinic Roosby radius is a natural scale in the ocean associated with boundary phenomena such as boundary currents, fronts and mesoscale eddies.

In numerical oceanographic modeling is practically unfeasible to model the global atmosphere/ocean with a spatial resolution capable to capture all types of motion in order to examine their dynamical interactions and time evolution. A time-space diagram indicating the processes resolved by different classes of ocean models is reported in Fig. 5.1.

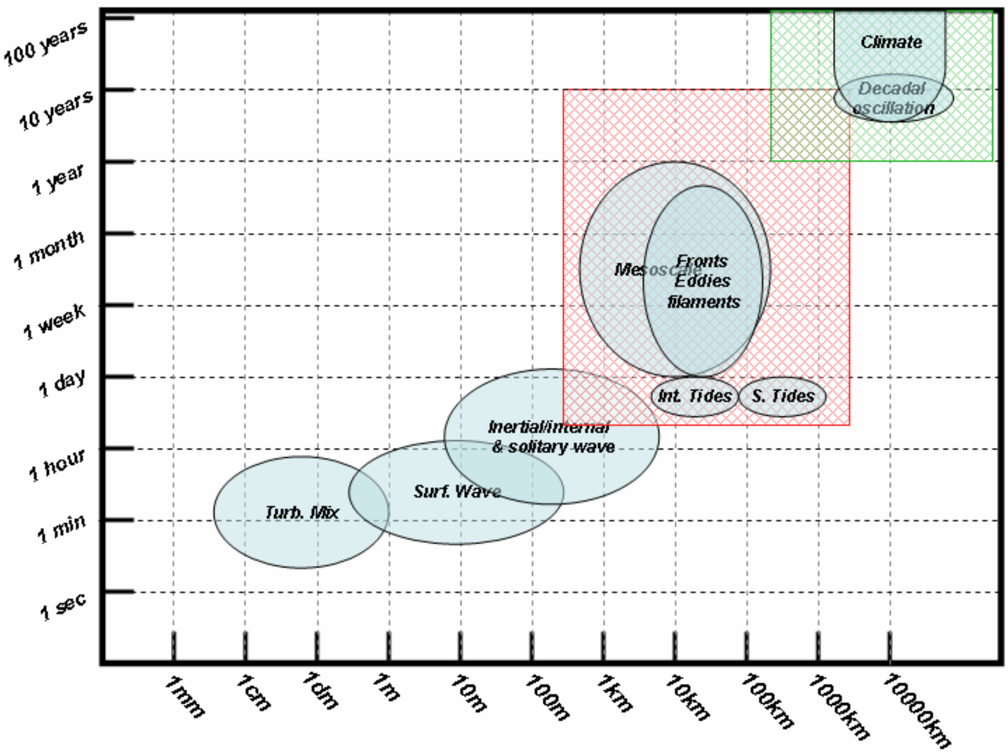

Figure 5.1 Space-Time diagram showing some physical processes. The rectangular areas indicate the scales resolved by the ocean circulation models (Red the Regional model, Green the Global Models).

In a numerical model of the ocean general circulation the primitive equations of motion and tracer conservation are integrated over a given three dimensional grid. The chosen spatial resolution of the grid determines the spatial scales that are explicitly resolved by the model.

It is known that a numerical model captures the processes having a spatial scale 3 or 4 times greater that the adopted grid increment. It turns out that an adequate parameterization of the processes not resolved by the grid is needed in order to achieve a satisfactory simulation of the ocean dynamics. The role played by the parameterization of such processes on the model solution is obviously depending on the grid resolution.

In numerical models using a σ vertical coordinate system, the dependency of the solution on the horizontal resolution is amplified as a consequence of the numerical interactions between the horizontal grid scale increment and the bottom following vertical discretization. The problem lies in the calculation of the pressure gradient terms in the momentum equations or generally in the computation of all the horizontal derivatives. This problem can be mitigated by subtraction of horizontal averaged fields before computing the derivative and can be also reduced by smoothing the horizontal topographic gradients. It is generally wise to process the bottom topography with a filter that caps the ratio of bottom depths of adjacent grid points before using them in the model. However care must be exercised to ensure that the topography is not severely corrupted by this smoothing, especially over the shallow coastal regions.

In this chapter the effect of small changes in horizontal resolution on the model capability to reproduce the Adriatic Sea dynamics interannual variability is investigated comparing the results obtained using different horizontal grid sizes in order to understand the needed resolution capable to capture the scales of interest. Our scales of interest are the mesoscale which are characterized by the first Rossby radius of deformation that in the Adriatic Sea is about 3-5 km in Summer (Masina and Pinardi, 1993) and almost zero during Winter.

Since, as described in Chapter 2, no observations are available for river runoff, except the Po, climatological values (Raicich, 1994) have been used in order to represent the river fresh water input into the basin. In this chapter we try also to validate the hypothesis made in Chapter 2, concerning a possible overestimation of these climatological values, reducing the prescribed data by an arbitrary factor.

We compare directly the results obtained applying both changes, horizontal resolution and rivers runoff, with the previous model implementation results.

5.2 Methodology

The model used in this experiments is based on the Princeton Ocean Model (POM, Blumberg and Mellor, 1987) described in Chapter 2. The hindcast numerical experiment of the Adriatic Sea circulation described in Chapter 2 has been repeated by using an horizontal grid having an higher and constant horizontal resolution (3 km) and reducing all the climatological rivers runoff from Adriatic rivers other than the Po by a factor of 0.5.

The climatological river runoff has been reduced in order to mitigate the underestimation in the predicted salinity found comparing the previous model results (see Chapter 2) with available observations. Beside the grid and the rivers runoff, the two models are identical.

Obviously the initial condition definition required the interpolation of the fields arising from the Zavatarelli and Pinardi (2003) climatological simulation on the 3 km grid.

The simulations span the period from January 1999 to December 2002, results for year 1999 are not shown as the relative simulations are considered to represent the models spin up period.

We compare the results from the two simulations beginning with the analysis of the volume integrated scalar properties and ending with the comparison between models results and observations. Being the surface fluxes computation carried out interactively (see Chapter 2), also these diagnosed proprieties are compared. To simplify the following discussion we will refer to the model described in Chapter 2 as 5KAM (5 km Adriatic Model) and to the model with increased horizontal resolution and reduced climatological rivers runoff as 3KAM (3km Adriatic Model).

5.3 Results and Discussion

In this section the results of the two experiments are compared and the impact of the horizontal resolution and reduced climatological rivers runoff evaluated.

The time series of the total heat flux and the wind stress curl for the two models are shown in Fig. 5.2. The time series show an almost identical trend, confirming the considerations on the interannual variability done in Chapter 2. The reason for these similarities can be traced back to the time series of the mean surface temperatures predicted by the models (Fig. 5.3 B). For this diagnosed property the two time series practically overlap and differences can not be detected.

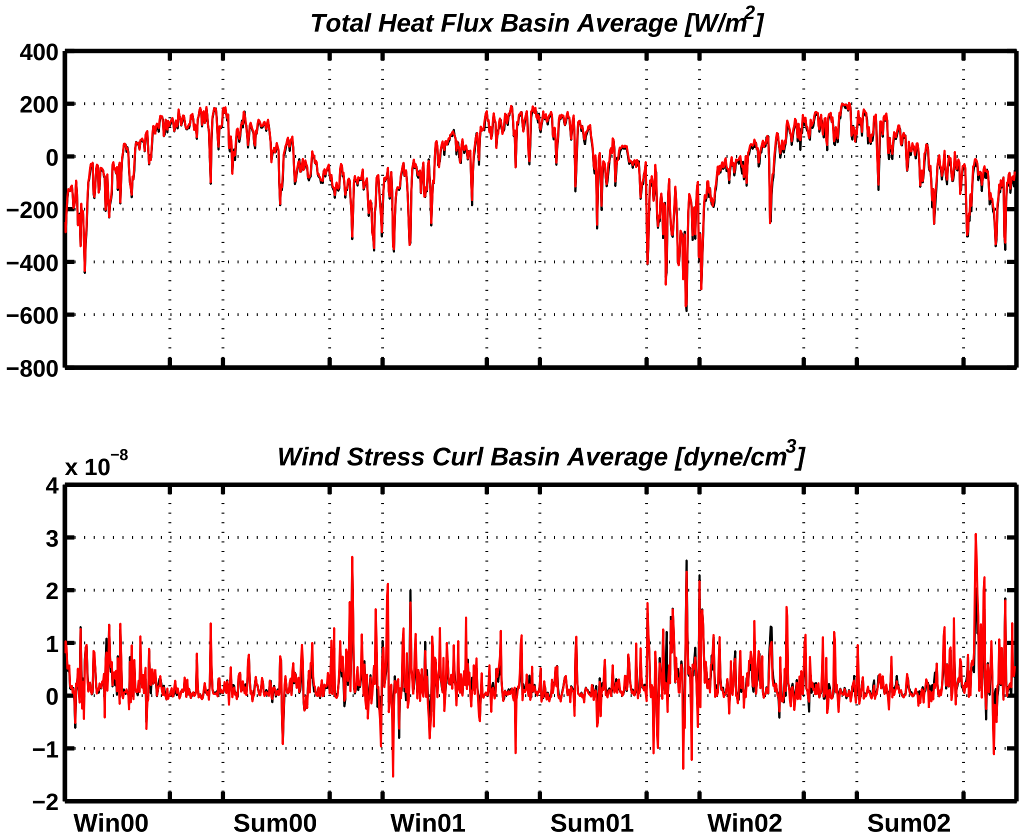

Figure 5.2 Temporal evolution of the basin averaged (a) total heat fluxes (W m^{-2}), (b) wind stress curl (dynes cm^{-3}) for the model simulation period (2000-2002). The red line indicates the 5KAM results, the dark line indicates the 3KAM results.

A small difference is instead notable in the volume averaged temperature time series (Fig. 5.3 A) as the 3KAM has higher values in summer 2002. The reduced climatological rivers runoff strongly affects the volume and surface averaged salinity (Fig. 5.3 C and D). The interannual variability in 5KAM and 3KAM is the same, but the freshening trend affecting 5KAM is considerably reduced in 3KAM. This is mainly due to the reduced river runoff imposed.

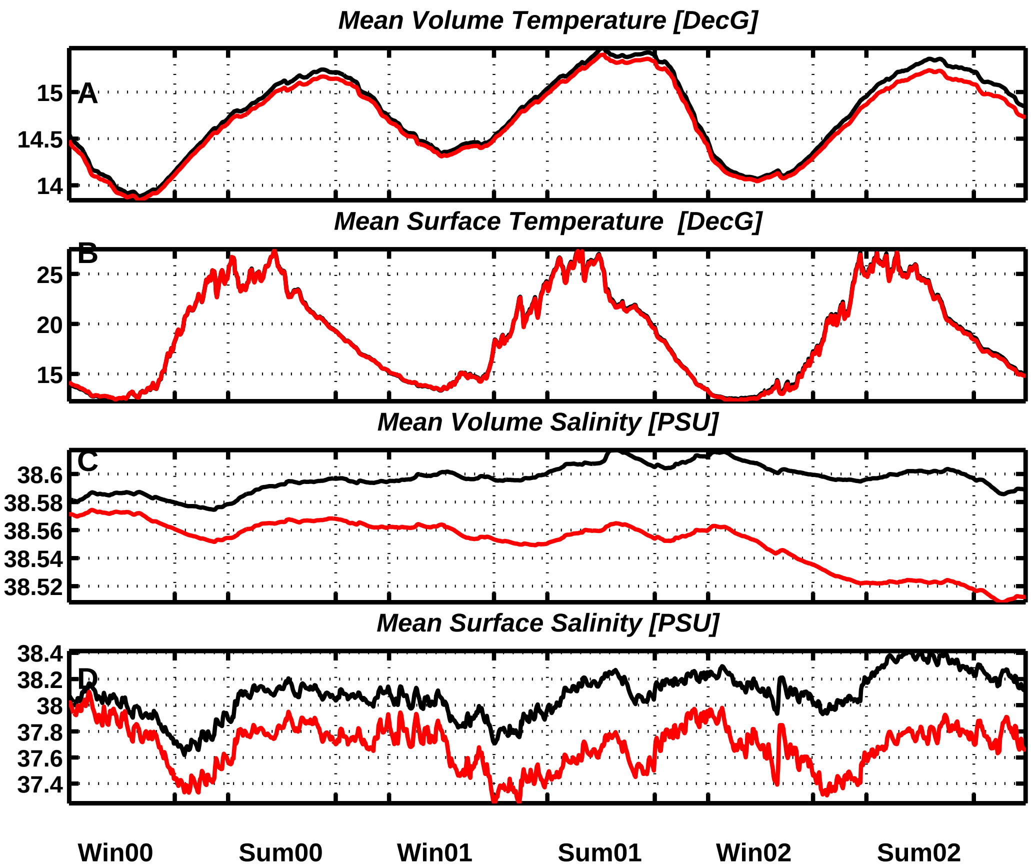

Figure 5.3 Temporal evolution of the basin and surface averaged scalar proprieties. The dark line indicates the 3KAM results, the red line indicated the 5KAM results. A) Mean volume temperature (°C). B) Mean surface temperature (°C). C) Mean volume salinity (psu). D) Mean surface salinity (psu).

In Fig. 5.4 and 5.5 the winter and summer temperature and velocity near surface (2m depth) fields predicted by 3KAM are shown. The three simulated winters (Fig. 5.4) appear similar to the 5KAM results (See Fig. 2.6 in Chapter 2). Moreover the increased horizontal resolution produces stronger gradients and better resolved circulation features. The 5KAM predicted WACC is wider (See Fig. 2.6 A B and C in Chapter 2) especially along the Emilia-Romagna coast, while in 3KAM this circulation feature is confined in the Italian coastal strip.

In front of the Monte Conero (Latitude 43° 30’ Longitude 44° 33’) the 3KAM results are characterized by a reduced detachment of the WACC from the coasts with respect to the 5KAM.

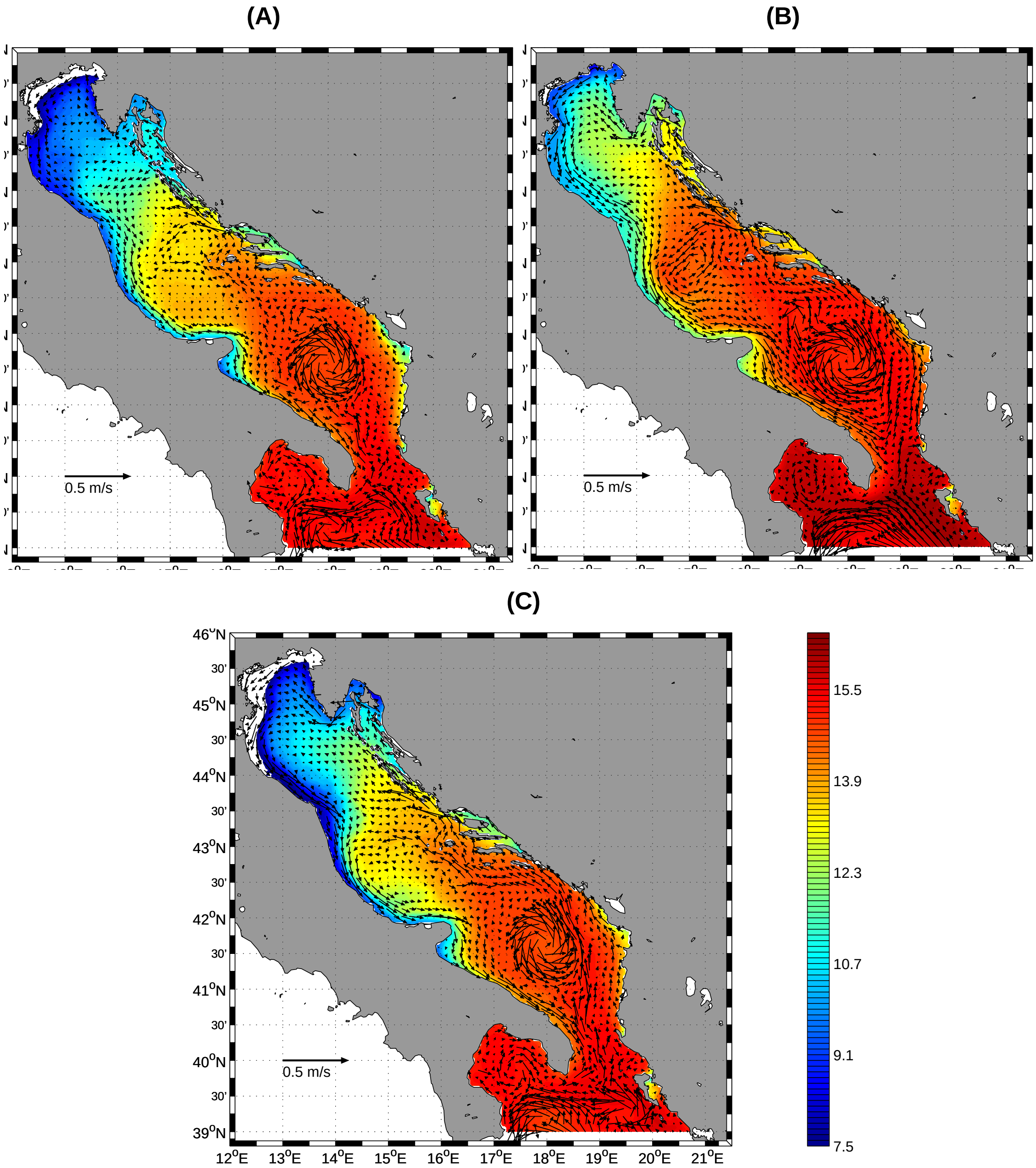

Figure 5.4 3KAM near surface (2m depth) temperature (°C) and velocity (m/s) fields for: winter 2000 (A); winter 2001 (B); winter 2002 (C).

In summer 2000 (Fig. 5.5 A for the 3KAM, Fig. 2.7 A in Chapter 2 for the 5KAM) interesting differences between the two models solutions can be noted in the Southern Adriatic. The SAd gyre of 5KAM is a unique large structure while in 3KAM there is a multitude of smaller gyres, one of them being large and anticyclonic.

(A) (B)

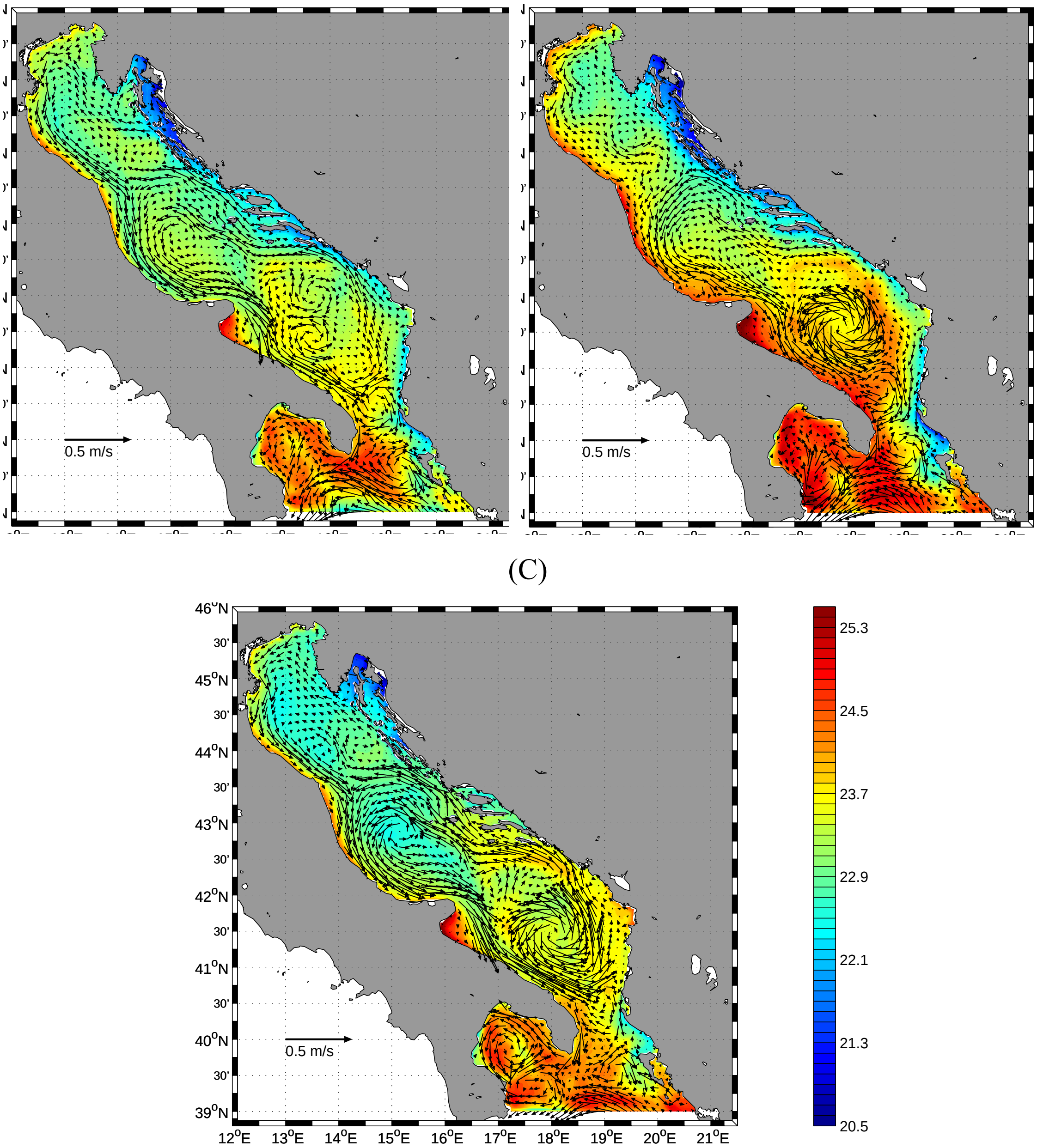

Figure 5.5 3KAM model near surface (2m depth) temperature (°C) and velocity (m/s) fields for: summer 2000 (A); summer 2001 (B); summer 2002 (C).

The summer 2001 Northern Adriatic is cooler in the 3KAM with respect to the 5KAM and the ESAC penetrates in the northern Adriatic. Strong differences between 3KAM and 5KAM appear in the Otranto Strait circulation. 3KAM produces a well defined anticyclonic gyre that controls the exchanges with the Ionian Sea. The same structure appears in 5KAM but is weaker.

The dense water formation process is strongly affected by the increased horizontal resolution and by the reduced climatological river runoff. In Fig. 5.6 the daily averaged time series of water volume having σ_θ > 29.20 kg m^{-3} for the three sub-basins in the two models are compared. Both time series in the Northern Adriatic are characterized by the absence of dense water formation during 2001.

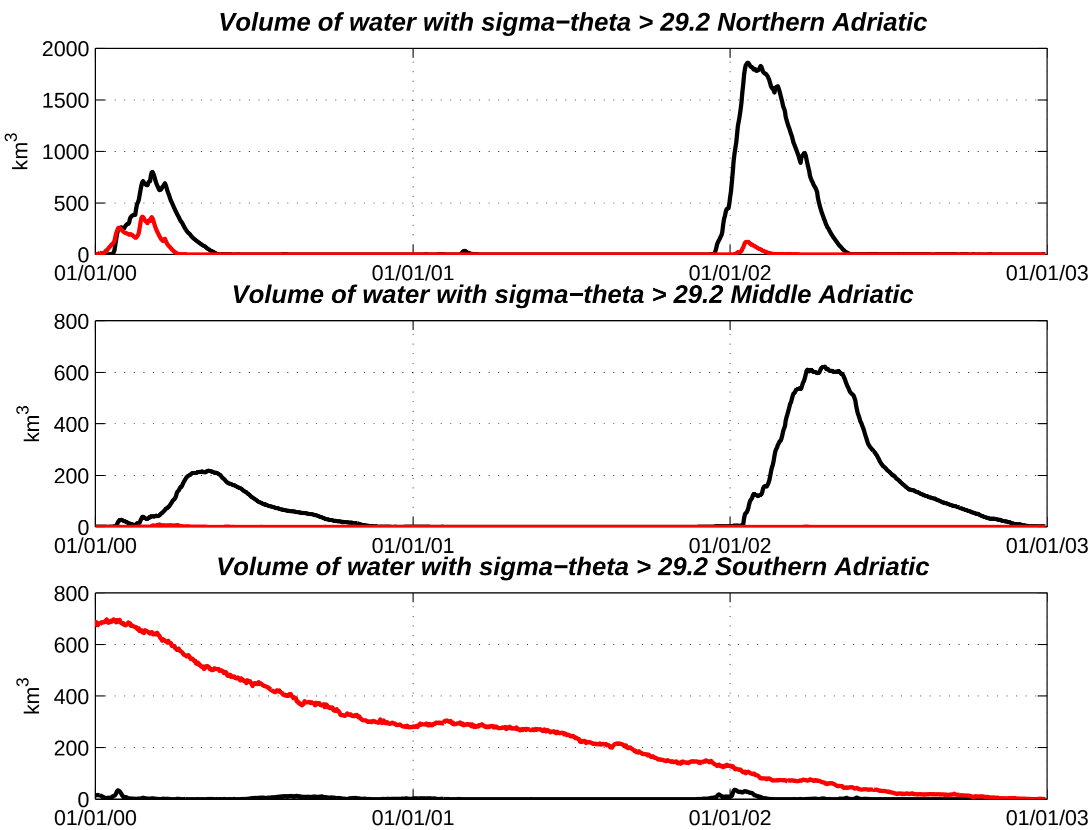

Figure 5.6 Temporal evolution of the total amount of waters having sigma-theta >29.2 kg m^{-3} in the three sub-basins (m^3). The dark lines indicate the 3KAM results, the red lines indicate the 5KAM results.

This result confirms the peculiar characteristics of this year as discussed in Chapter 2 and indicates that the dense water formation process in the Northern Adriatic strongly depends on the Po river discharge and atmospheric forcing, as in the two experiments these forcings are the same. Moreover the increased horizontal resolution and, mostly, the reduced runoff influence the amount of dense water formed. The amount of dense waters in the Middle Adriatic, as discussed in Chapter 2, is directly related to the dynamics occurring in the Northern sub-basin and the differences between the two time series have to be traced back to the different values predicted by the two models in the Northern sub-basin. The Southern Adriatic time series predicted by the two models are instead strongly different. The progressive decrease of the amount of dense water observed in the 5KAM is not confirmed by the 3KAM simulation. The time series obtained with the 3KAM show constant (and small) values with two relative maxima occurring in the beginning of 2000 and 2002 winter. It is known that a certain amount of dense water is always present in the Southern Adriatic (as results by the climatological simulation show, Zavatarelli *et al*, 2002) and our results are not capable to capture this feature. Since the 3KAM implementation does not improve the Southern Adriatic dense water simulation, probably this deficiency depends on a common (3KAM and 5KAM) parameterization as the data used to prescribe the boundary conditions or the vertical level resolution of this area. Increasing the horizontal resolution of the Adriatic model, the ratio between nested and nesting model grids increase, in the northern Ionian, and the problems examined in Chapter 4 for the open boundary conditions could be amplified.

In Fig. 5.7 the winter mean meridional transport streamfunction, indicating the thermohaline circulation, predicted by 3KAM is shown. This confirms the main characteristic predicted by the 5KAM, but differences can be traced in intensity and position of the structures. In winter 2000 (Fig. 5.7 A) the antiestuarine cell A2 (the classification of the cells is given in Chapter 2) has a larger extension with respect to the 5KAM results (Fig. 2.9 Chapter 2) and the branch of the cell A1 that intrudes in the Middle Adriatic is better defined.

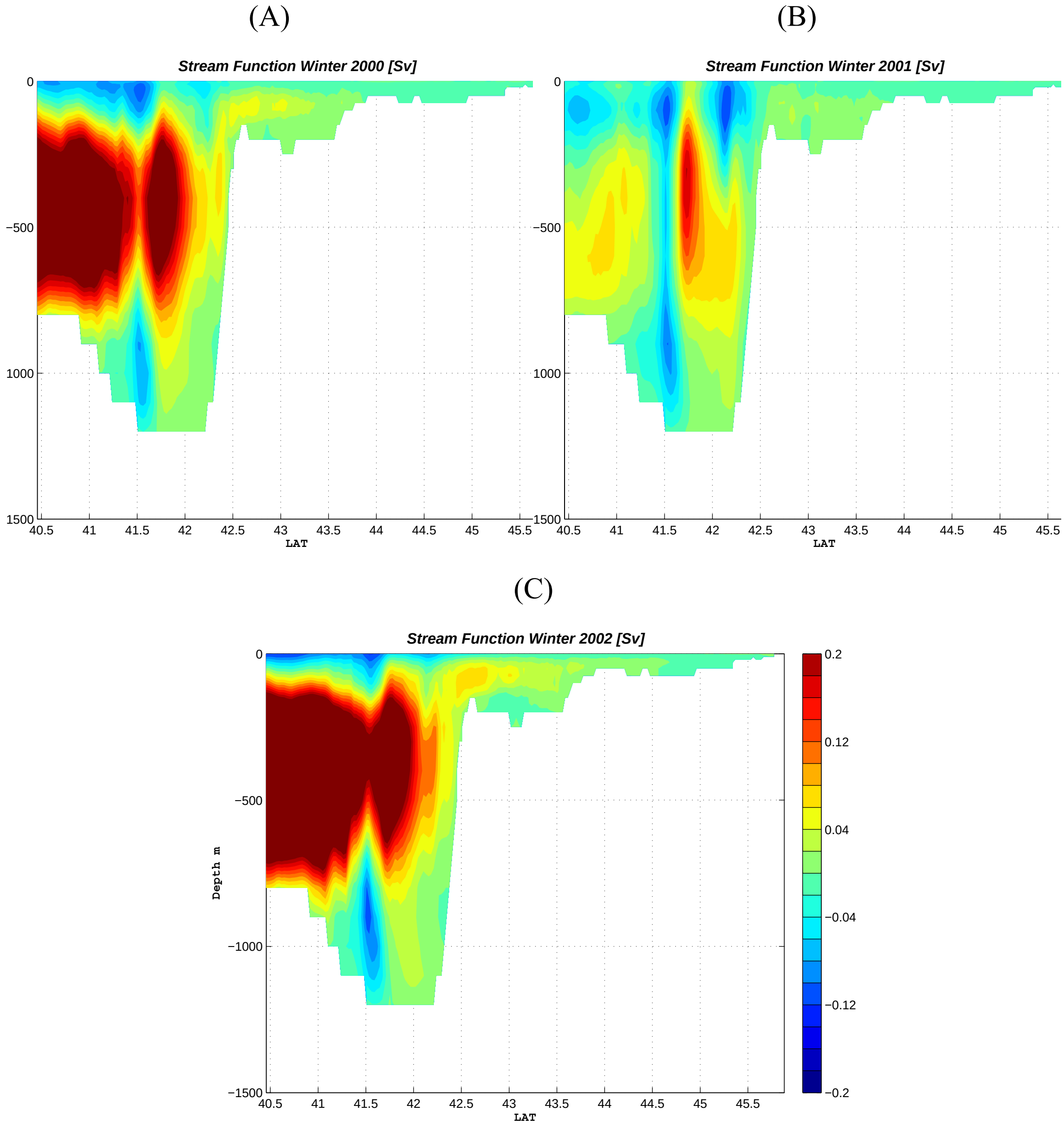

Figure 5.7 3KAM meridional transport stream function (Sv) winter mean for: (a) year 2000; (b) year 2001; (c) year 2002.

In winter 2001 (Fig. 5.7 B) the surface estuarine cell is less intense in the Southern part of the basin. In winter 2002 (Fig. 5.7 C) the two antiestuarine cells almost connect and the branch intruding in the Middle Adriatic is enhanced and well defined. In the same year the surface intensified estuarine cell E1 is confined to the surface layers with respect to the 5KAM results (Fig. 2.9 C in Chapter 2). Moreover the predicted thermohaline circulation pattern is helpful in understanding the possible reasons for the lack of dense water in the Southern sub-basin.

It was largely documented (see Robinson *et al*, 2001 for a complete review) that the intrusion of Levantine Intermediate Waters (LIW), occurring at 200-300m depth, plays an important role in the Adriatic deep water formation process and more specifically in 'preconditioning' this process. It was shown that the existence of the LIW layer greatly influences the depth of the winter convection penetration in this area.

In the models, the position and the intensity of the A2 cell that is mostly determined by the prescribed open boundary values determine the kind and the amount of water that intrudes in the Adriatic concurring to the dense water formation process. Both models and in particular the 3KAM, underestimate the depth of the interface between the cell E1 and the antiestuarine cells determining a mild preconditioning phase.

5.3.1 Comparison between model results and observations

In order to verify and quantify the improvement deriving from the increased resolution and the reduced climatological rivers runoff a comparison between the 3KAM results with the MAT data (details on the MAT data and on the comparison is are given in Chapter 2) has been performed. The only remarkable difference between 3KAM and 5KAM results can be noted in winter 2000 (Fig. 5.8 D for the 3KAM and Fig. 2.10 D for the 5KAM). In this period the 3KAM better reproduces the observed stratification in the western part of the section but the bottom water are characterized by lower temperatures in the eastern part that do not match the observed values. For the other two simulated winters no significant differences can be noted.

The problem pointed out in Chapter 2 regarding the low salinity values is mitigated mainly by the reduced climatological rivers runoff. The observed and

3KAM predicted salinity sections for the winter season are shown in Fig. 5.9. Especially in 2001 and 2002 the predicted values are closer to the observations than the 5KAM results (Fig. 2.11 in Chapter 2). These results partially confirm the hypothesis done on the overestimation of the climatological rivers runoff and justify the idea to apply a reducing factor.

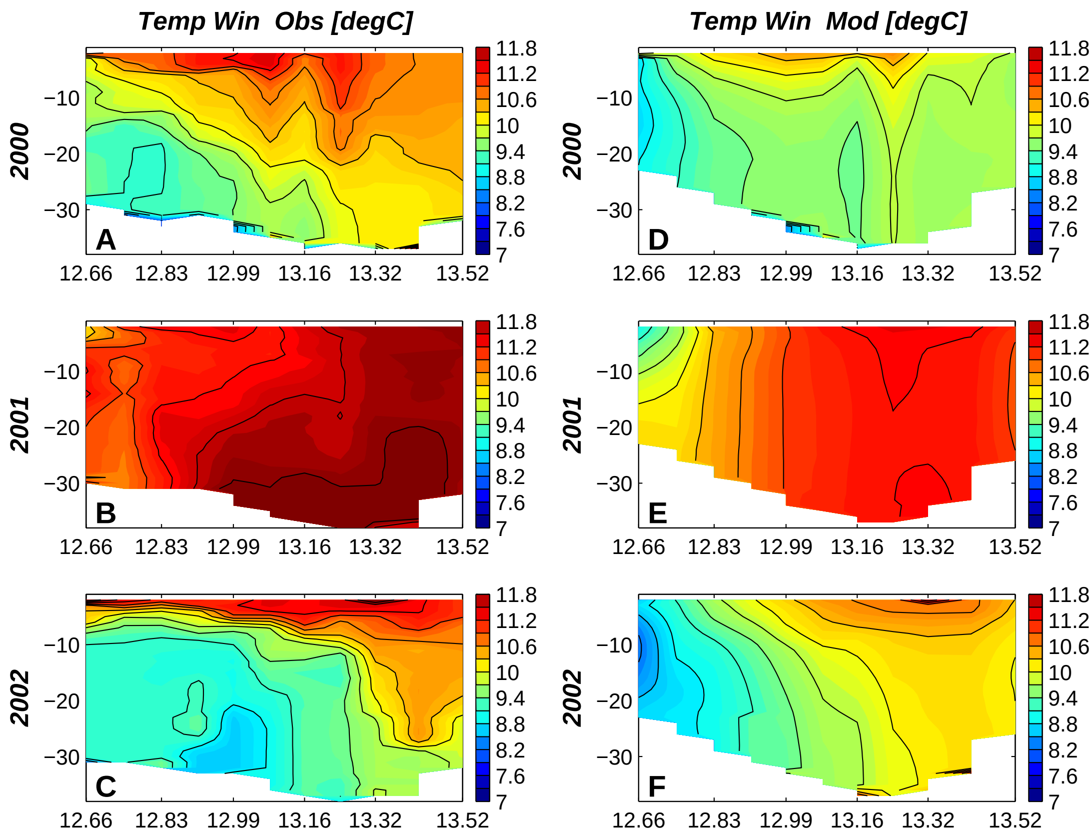

Figure 5.8 Vertical temperature distributions (°C) along the transect A for the simulated winters. (A-B-C) 2000, 2001 and 2002 winters means from observations. (D-E-F) 2000, 2001 and 2002 winters means from 3KAM results. The position of the transect is reported in Figure 2.1.

For the spring and summer (not shown) simulations no significant improvements can be seen from the new model. This indicates that during these seasons the differences between models results and observations derive from a parameterization that has been used in both the models as perhaps the atmospheric forcing or the vertical mixing.

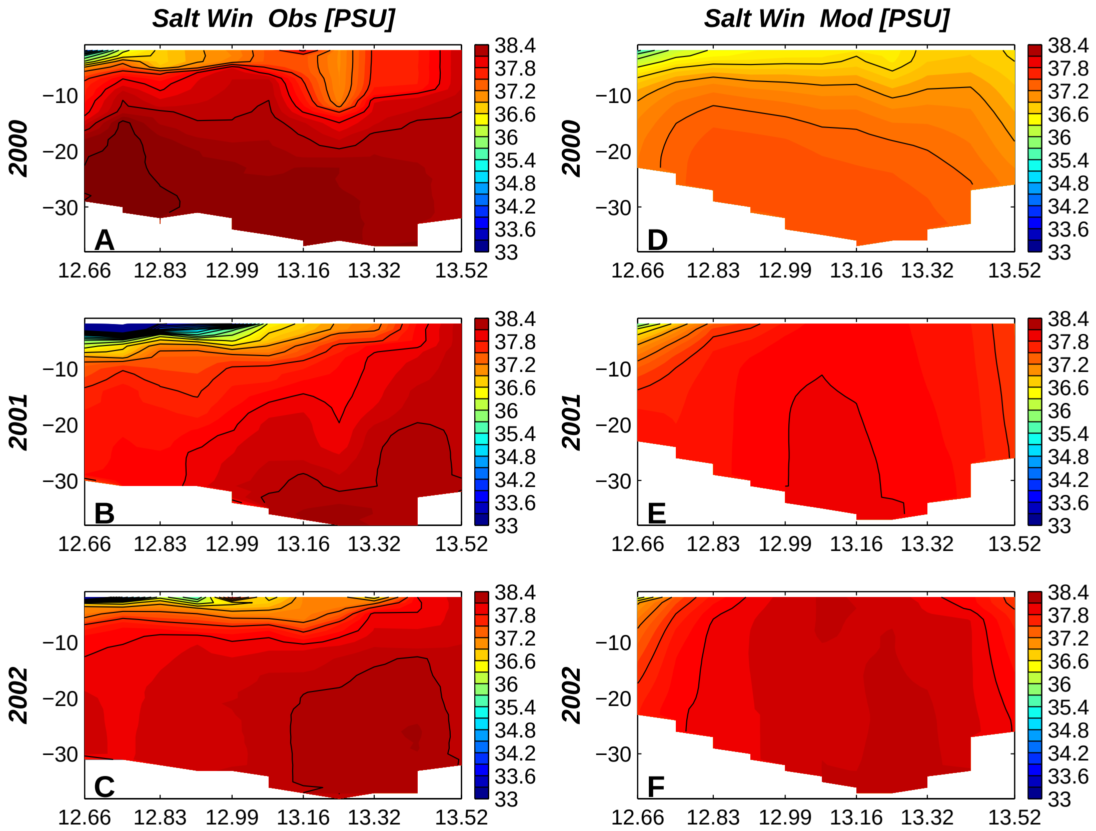

Figure 5.9 Vertical salinity distributions (psu) along the transect A for the simulated winters. (A-B-C) 2000, 2001 and 2002 winters means from observations. (D-E-F) 2000, 2001 and 2002 winters means from 3KAM results.

The Autumn 2000 temperature values, along transect A (Fig. 5.10 C), are characterized by strong vertical mixing that totally destroy the correct stratification observed in the 5KAM results (Fig. 2.15 C in Chapter 2). Moreover the surface and eastern predicted value are closer to the observations. In 2001 the simulated temperatures (Fig. 5.10 D) are better with respect to the 5KAM results, with the exception of the easternmost part of the section where the 3KAM seems to underestimate the cooling process,

As performed for the 5KAM results in Chapter 2 a comparison with ADRIA01 data for February 2001 monthly mean surface temperature is shown in Fig. 5.11. The 3KAM results better match the WACC extension especially in the Middle and Southern Adriatic and the predicted temperature is closer to the observation. Moreover the Northern sub-basin is still affected by an excessive diffusivity suggesting the necessity to have e dedicated model for this sub-basin.

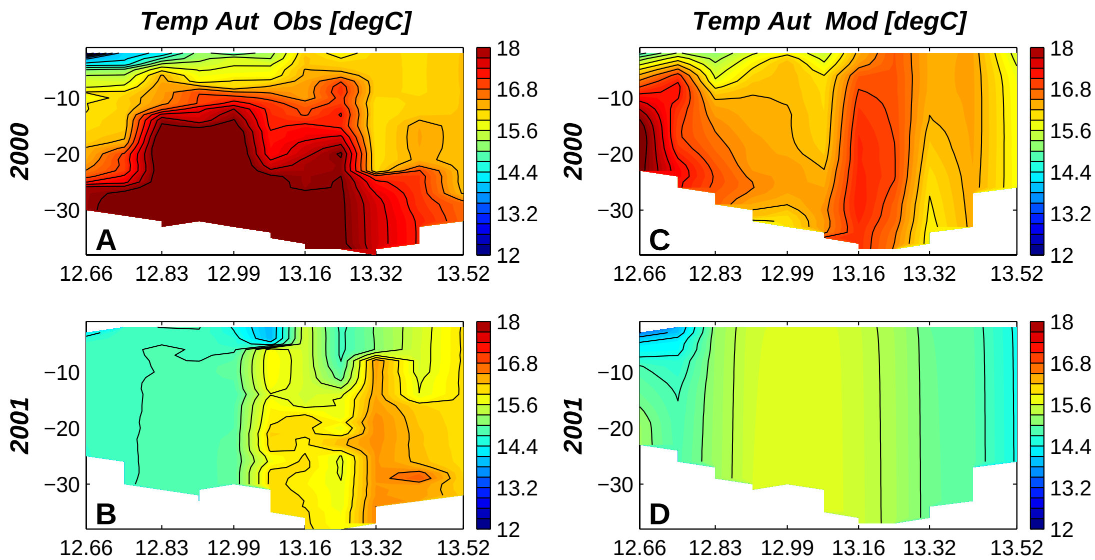

Figure 5.10 Vertical temperature distributions (°C) along the transect A for the 2000 and 2001 autumns. (A-B) 2000 and 2001 autumns means from observations. (C-D) 2000 and 2001 autumns means from 3KAM results.

5.4 Summary and Conclusions

In this Chapter the sensitivity of the model hidncasts to the horizontal resolution and a reduced river runoff has been investigated. The results obtained with the new model configuration have been compared with the results of a previous implementation and with available observations. The experiment results suggest that both the 3KAM and 5KAM models adequately resolve the Adriatic circulation in terms of seasonal mean and interannual trend. Moreover the 3KAM better resolve some specific structures as the WACC and the SAd gyre.

As the two models predict similar seasonal mean circulation patterns it turns out that the smaller scale features reproduced by the 3KAM give a minor contribution to the mean field in a large percentage of the studied areas. During summer 2000 the results of the 3KAM (Fig. 5.5 A) indicate a complex configuration of the SAd gyre, that, maintaining the overall cyclonic character, result in a complex ensemble of cyclonic and anticyclonic gyres.

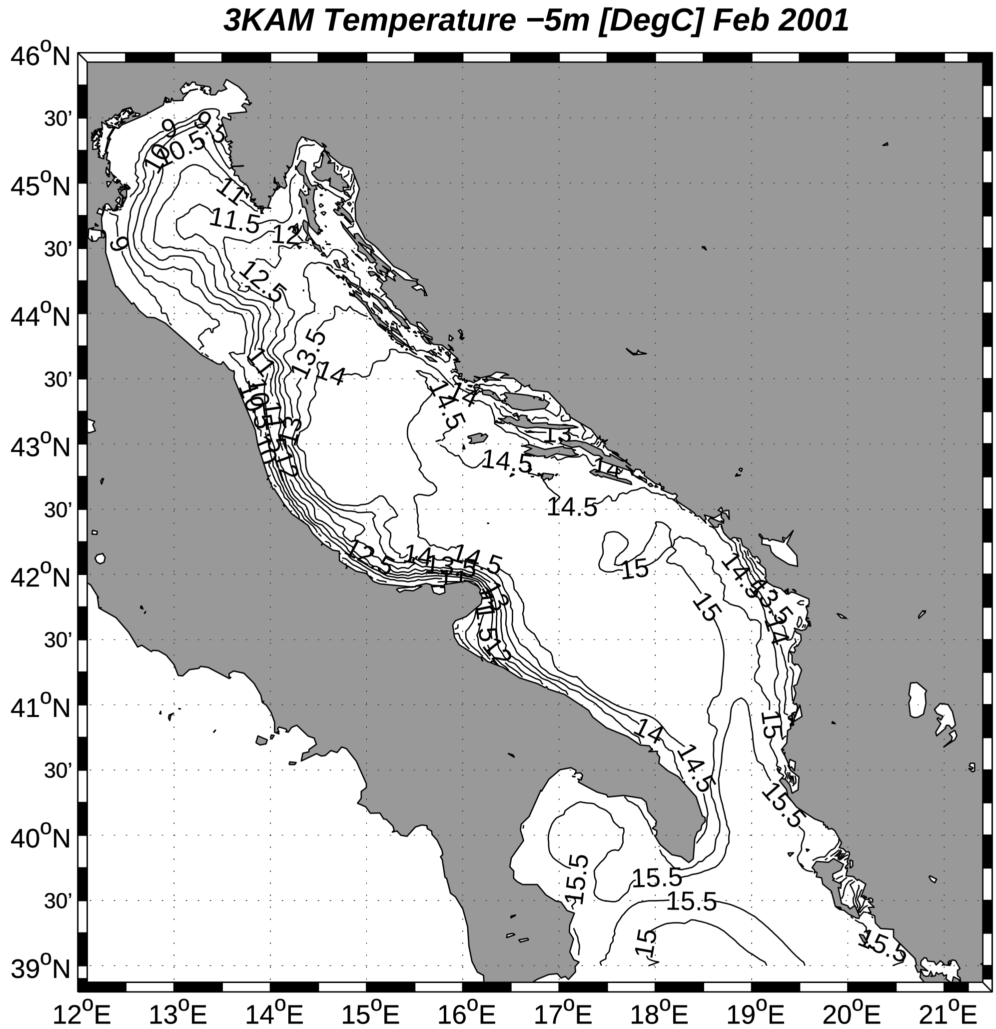

Figure 5.11 February 2001 monthly mean near surface (5m depth) temperature (°C) from 3KAM.

The major differences between the two models simulations seem related to the reduced climatological river runoff that strongly affects the amount of dense water formed. The results relative to the dense water in the Southern Adriatic indicate that this model deficiency is not related to the horizontal resolution or to the overestimation in the climatological rivers runoff but probably to an inaccuracy on the data used to prescribe the boundary values.

The comparison with the MAT transects indicates that also for the 3KAM the major model deficiency is related to the overestimation of the vertical mixing processes even if the reduced river runoff has mitigated the large discrepancy between observed and predicted salinities along the sections.

Future improvements involve the sensitivity to vertical resolution and the change of the nesting model.

Chapter 6

A High Resolution Multi-Model Comparison Study:

The Northern Adriatic Sea Experiment

6.1 Introduction

Sub-basin scale circulation features in the Northern Adriatic are mainly associated with the Po River run-off and wind forcing (Hendershott and Rizzoli, 1976; Malanotte-Rizzoli and Bergamasco, 1983; Gacic *et al*., 1992).

The spreading of the Po River waters display a seasonal signal depending on the vertical density stratification related to heating and wind regimes. Analysis of in situ data (Orlic, 1989, Artegiani *et al*., 1997) and Coastal Zone Color Scanner (CZCS) images (Sturm *et al.*, 1992) show that during the winter the Po River water is trapped is the Italian coastal strip, whereas during the summer significant offshore spreading of less saline waters is observed. During winter the interaction of topography and the density field plays an crucial role and conservation of potential vorticity prevents the Po River water injected in the coastal area to cross isobaths that run parallel to the Italian coast (Shaw and Csanady, 1983, Woods and Beardsley, 1988) confining the fresh waters to a narrow coastal strip about 10 km wide (Franco, 1983).

During summer, strong pycnocline is present due to the surface heating and lack of strong winds. The Po River water flows above the pycnocline without interaction with the bottom and spreads not only along the western coast, but toward the northern and eastern coasts as well.

Strong Bora wind episodes or strong impulses of the Po River runoff can, however, cause the transient freshwater spreading in the basin interior during the winter season (Zore-Armanda and Gacic, 1987, Barale *et al*., 1986; Sturm *et al*., 1992).

The northern Adriatic is a site of dense water formation (see Malanotte-Rizzoli, 1991, for a review). The dense water mass ($\sigma_\theta > 29.2$ Artegiani *et al*., 1989) flows southward along the bottom, entering the Pomo pits and possibly prosecuting toward the southern Adriatic (Artegiani *et al*., 1989).

Numerical modeling of the northern Adriatic due to the complexity of the forcing functions is a challenging task. The choices of the horizontal-vertical resolution and of the physical assumptions that can be done are crucial for a correct simulation of the circulation features and variability. The internal Rossby radius of deformation, in the Northern Adriatic, is expected to be of the order of 3-5 km (Masina and Pinardi, 1994, Bergamasco *et al*., 1994). Therefore a horizontal resolution at least three times lower should be needed to explicitly resolve the mesoscales. An adequate parameterization of all the boundary, surface and lateral, exchanges is indispensable to allow the sub-basin dynamics to correctly evolve in space and time. Since under calm forcings regime the conversion of internal potential energy into kinetic energy (baroclinic instability) is the engine of the circulation also an accurate numerical representation of this process is needed.

The study reported in this Chapter is a first attempt at understanding the physical parameterizations needed in order to reproduce adequately the Northern Adriatic dynamics. We focalize on the ocean model given that the role of the atmospheric

forcings has been already largely investigated (see Paklar *et al.*, 2001 for a review).
Two strongly different ocean models have been implemented and 30 days simulations performed, the results are compared between models and with available observations.

6.2 Methodology

6.2.1 Models

Two different models have been used in order to evaluate their performance in reproducing the Northern Adriatic Sea dynamics: the Princeton Ocean Model (POM, Blumberg and Mellor, 1987) and the Harvard Ocean Prediction System (HOPS, Robinson, 1999). The models differ for some basic physical assumptions and for the numerical discretisation techniques. The main difference between the physical assumptions in the two models regards the sea surface elevation: in HOPS the rigid-lid approximation has been considered, while POM has an explicit formulation for the sea surface elevation. The basic HOPS equations are written in spherical coordinates (λ, θ, z), that is, the longitude, latitude and the local normal to the earth surface, and are reported in Table 6.1. The POM basic equations are instead written in rectangular coordinates and have been discussed in Chapter 2. Moreover, HOPS assumes that the eddy viscosity-diffusivity coefficients can be considered constant, while in POM the same coefficients are provided by the Smagorinsky (1993) parameterization for viscosity and using the Prandle number for the diffusivity. The vertical mixing coefficients for momentum and tracers in POM are calculated using the Mellor and Yamada (1982) turbulence closure scheme, while in HOPS are derived from the Pacanowsky and Philander (1981) parameterization. The HOPS model contains also the so called “convective adjustment” that in case of instable conditions forces the model to use high mixing coefficients in order to restore a stable vertical density profile. In the temperature equation, POM, considers also the heat penetration in the water column (Pinardi *et al.*, 2003).

$\frac{\partial u}{\partial t} + \vec{u} \cdot \vec{\nabla} u - tg\theta \frac{uv}{r} - 2\Omega \sin\theta \, v = -\frac{1}{\rho_o} \frac{1}{r\cos\theta} \frac{\partial p}{\partial \lambda} - A_h \nabla^4 u + A_v \frac{\partial^2 u}{\partial z^2}$
$\frac{\partial v}{\partial t} + \vec{u} \cdot \vec{\nabla} v + tg\theta \frac{u^2}{r} + 2\Omega \sin\theta \, u = -\frac{1}{\rho_o} \frac{1}{r} \frac{\partial p}{\partial \theta} - A_h \nabla^4 v + A_v \frac{\partial^2 v}{\partial z^2}$
$\frac{\partial p}{\partial z} = -\rho(x, y, z, t)\, g$
$\frac{1}{r\cos\theta} \left\{ \frac{\partial u}{\partial \lambda} + \frac{\partial}{\partial \theta}(v \cos\theta) \right\} + \frac{\partial w}{\partial z} = 0$
$\rho = f(T, S, p)$
$\frac{\partial T}{\partial t} + \vec{u} \cdot \vec{\nabla} T = -K_h \nabla^4 T + (\delta + K_v) \frac{\partial^2 T}{\partial z^2}$
$\frac{\partial S}{\partial t} + \vec{u} \cdot \vec{\nabla} S = -K_h \nabla^4 S + (\delta + K_v) \frac{\partial^2 S}{\partial z^2}$

Table 6.1. Basic equations for the HOPS model. Where r is the earth's radius, Ω the earth' rotation rate, ρ_0 is a constant density value, A_h , A_v the constant eddy viscosity coefficients, K_h , K_v the constant eddy diffusivity coefficients, δ the parameterization of convective adjustment and $\vec{u} = (u, v, w)$ the three dimensional velocity vector.

The two models differ also in the numerical techniques used. For instance in POM the diffusive terms in the primitive equations are explicitly discretised while in HOPS are parameterized using the Shapiro (1970) filter.

The models have been implemented on the same regular horizontal grid with 1.5 km resolution covering the North Adriatic, while different vertical discretization have been used: in POM 21 σ-layers (see Chapter 2) define the vertical system; in HOPS the same number of layers has been used in a double σ system. The bathymetry has been obtained from U.S. Navy data (horizontal resolution: 1/60°) and the minimum depth has been set to 5 m. In Fig. 6.1 the models domain and the bathymetry are reported. The rivers discharges have been implemented as a salt flux in both cases, but different surface boundary conditions have been used for the salinity. For the POM based model the same surface boundary condition described in Chapter 2 has been used, while for the HOPS a simple relaxation scheme has been adopted to represent the river runoff:

$$K_H \left.\frac{\partial S}{\partial z}\right|_{z=\eta} = S_{z=\eta}(E-P)+\frac{\Delta t}{\tau}\left(S^*-S\right)$$

Where S* is the river water salinity and τ the relaxation time that has been implemented as a function of the instantaneous river runoff. For both models a pure Orlansky (1976) open boundary condition has been used for all the diagnosed variables (details on the boundary conditions are given in Chapter 4), For the POM based model also a zero transport constraint has been adopted in order to ensure the volume conservation (see Chapter 4).

6.2.2 Experiments set-up

During September-October 2002, a hydrographic campaign in the northern Adriatic was carried out by the NATO SACLANT centre of La Spezia. Temperature and salinity data were collected with high temporal and spatial resolution. This data have been used to obtain the initialization field and for models calibration-validation.

The initialization field has been obtained using an objective analysis (OA) scheme with small space and time correlation factors. The OA utilizes the Gauss-Markov or minimum error variance criterion to map the sparse available data to regular horizontal grids (Carter and Robinson, 1987; Robinson, 1996).

In both models the fluxes are interactively computed using realistic atmospheric fields having 0.5° horizontal resolution from the European Centre for Medium range Weather Forecast (ECMWF) analysis (details on the surface boundary conditions are given in Chapter 2).

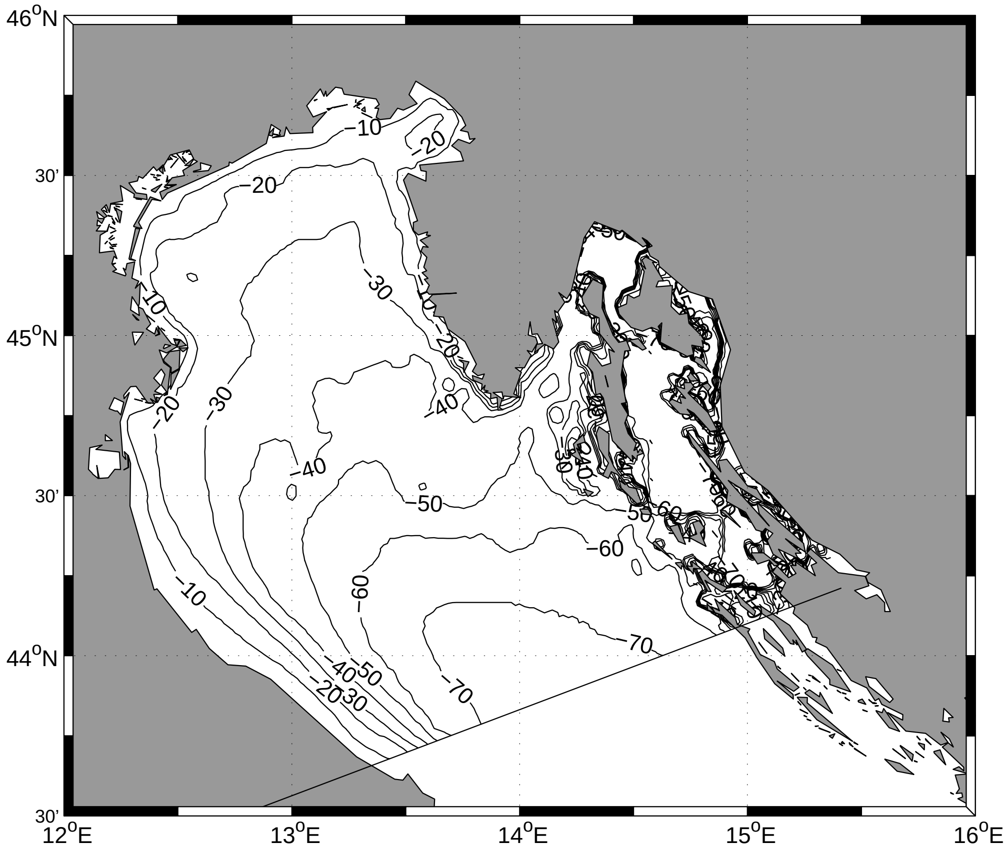

Figure 6.1 Model domain and bathymetry are shown. The depth is given in meters.

The river runoff data for the Northern Adriatic Rivers, Po excluded, were obtained from the Raicich (1994) monthly climatology. Po river runoff values are daily averages for the simulation period as measured by the Po River Authority at the closing section of the drainage basin. The Po runoff is distributed over 6 grid points representing the mouths of the delta (Provini *et al.*, 1992). The simulations span 30 days starting from September 16th 2002

6.3 Results and Discussion

In this section, after a brief overview of the surface forcings, the results are compared between models and with available observations.

In Fig. 6.2 the domain averaged daily wind stress vector time series and the Po River runoff are shown. The wind stress vector time series is characterized by a Bora event (N-NE direction) occurring on September 26th, while during the remaining time it is dominated by calm wind regime having mostly Northward direction. The time series of the Po river runoff reach the maximum values at the beginning and at the end of the simulation and a relative maximum occurs in correspondence of the Bora event.

The sea surface temperature (SST) and salinity (SSS) initialization fields are shown in Fig. 6.3 A and B respectively. The surface temperature ranges between 21.5 °C and 23°C, with small cyclonic and anticyclonic structures in front of the Po delta; the northernmost and the westernmost areas are characterized by cooler temperatures probably as a consequence of the missing data in those regions. The surface salinity distribution is characterized by a Po plume that mostly extends in the westward direction that is a typical configuration for calm and stratified period.

After 10 days (Fig. 6.4 A and B) the two models solutions differ in values but similar structures appear in both simulations. During the first 10 days of integration the Northern Adriatic system is forced by weak winds and the models develop small mesoscale features being the internal dynamics the major energy redistribution mechanism. Moreover the HOPS solution appears warmer respect to POM probably as a consequence of a stronger stratification and of the different surface boundary conditions used for the temperature. Also the mesoscale structures predicted by the two models have different position and intensity.

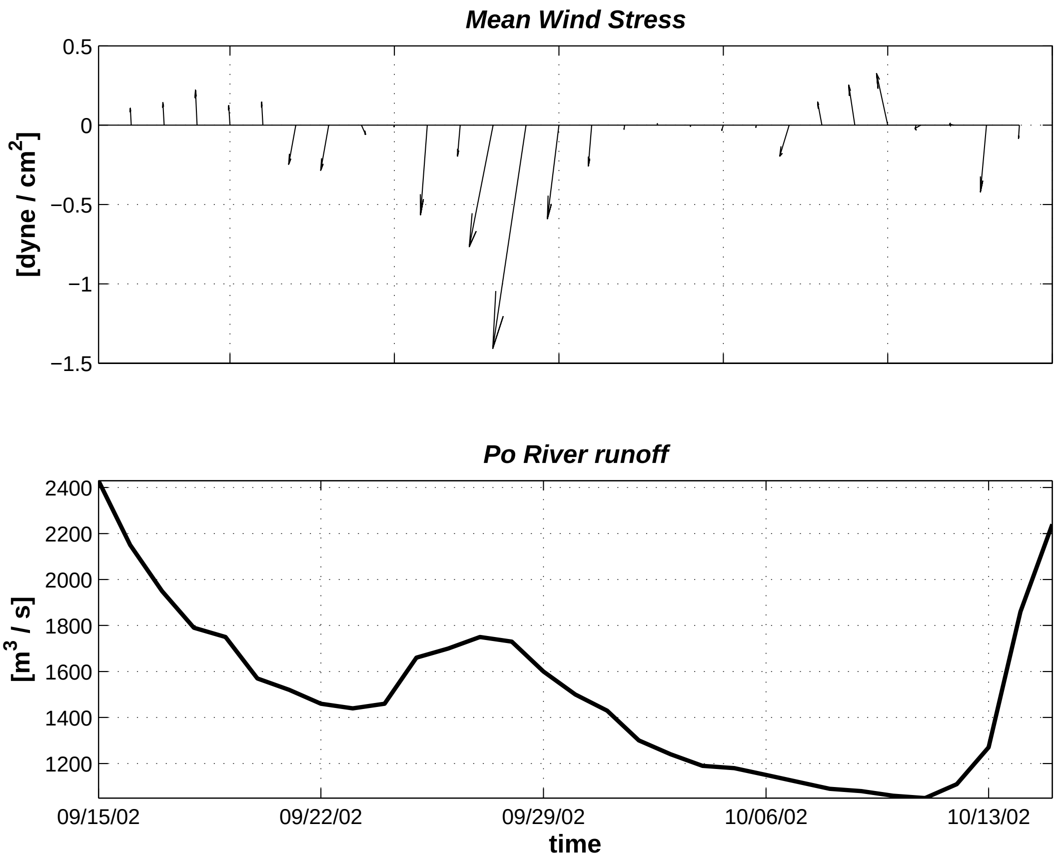

Figure 6.2 Time series of wind stress [dynes/cm^2] and Po River runoff [m^3/s].

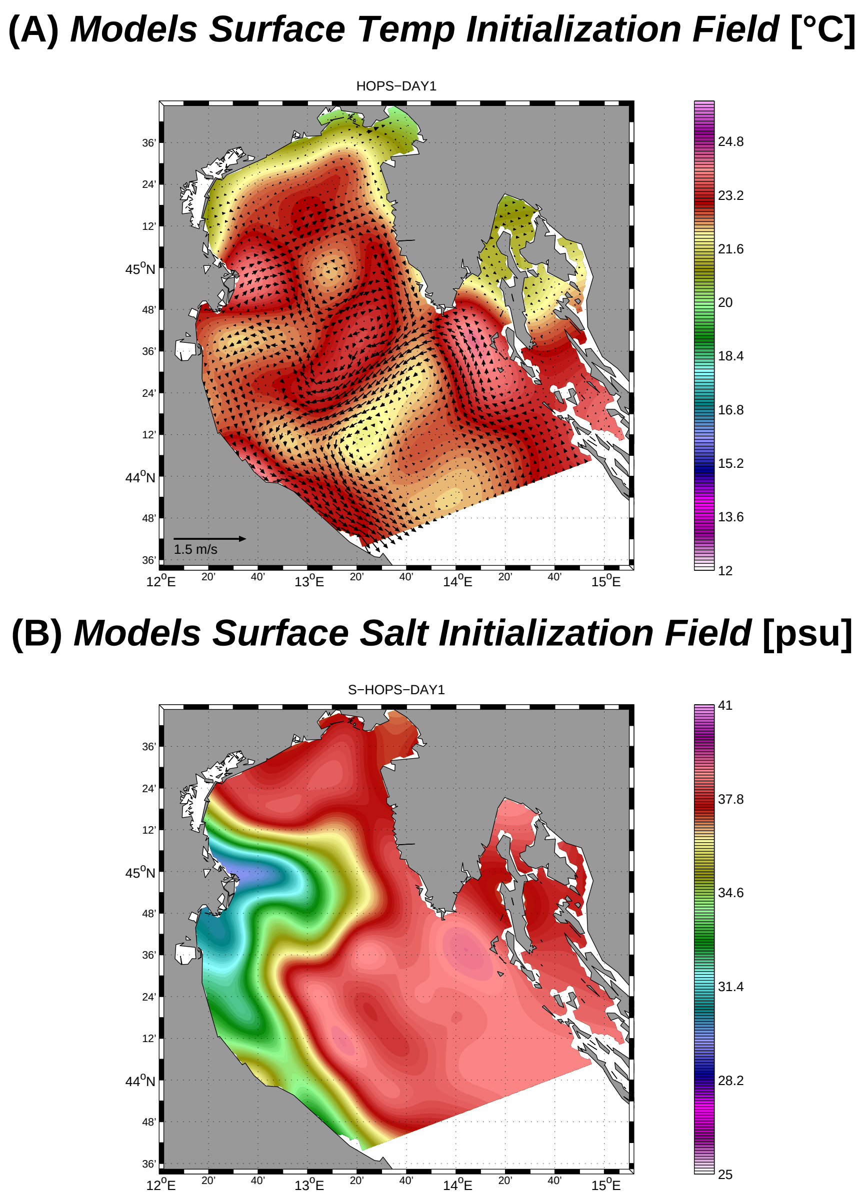

Figure 6.3 (A) Sea surface Temperature [°C] and velocity initialization fields. (B) Surface salinity [psu] initialization field.

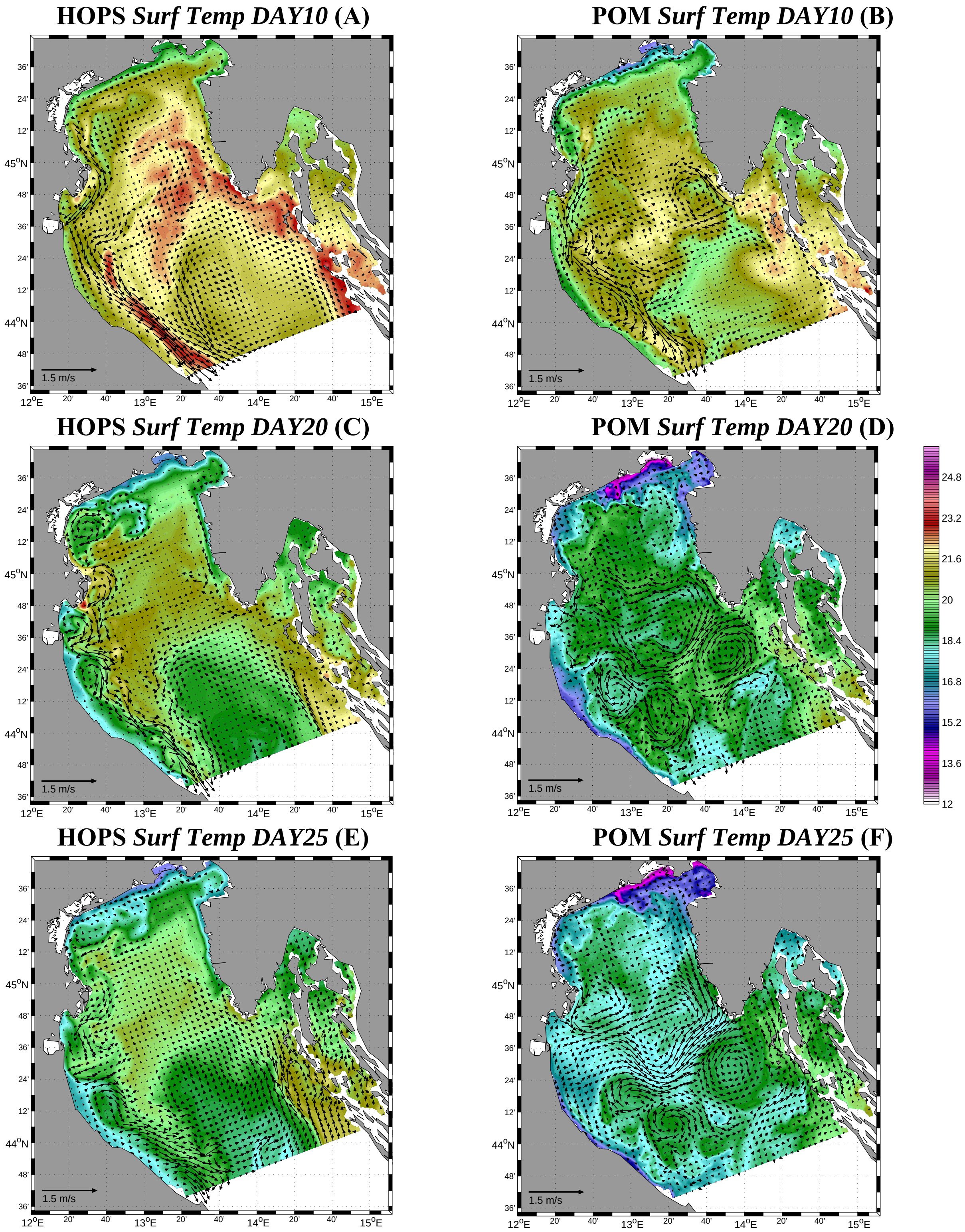

Figure 6.4 Sea surface Temperature [°C] and velocity fields [m/s]. (A) HOPS day 10; (B) POM day 10; (C) HOPS day 20; (D) POM day 20; (E) HOPS day 25; (F) POM day 25.

After the Bora event, 20^{th} day of integration (Fig. 6.4 C and D), strong differences between the models solution appear. Both models predict cooler temperature as a consequence of the overturning caused by the strong wind that allows the cold bottom water to reach the surface. Moreover HOPS model produces small mesoscale eddies only close to the Italian coast, along the Western Adriatic Coastal Current (WACC), while in the eastern part of the basin predicts large scale features. The strong wind forcing, causing a vertical mixing and strong horizontal currents, has the final effect to dump down the potential energy build-up.

The POM solution is characterized by small structures also in the eastern domain. We can argue that in POM the surface gravity waves, permitted by the free-surface formulation, faster re-establish horizontal and vertical gradients that cause the observed circulation pattern.

The differences pointed out above are amplified after 25 days of integration (Fig. 6.4 E and F). The cooling process occurs in both models, but the POM solution appears more diffusive allowing the WACC to detach from the Italian coast reaching the middle part of the basin.

In Fig. 6.5 the surface salinity fields for the 10^{th} 20^{th} and 25^{th} days are shown.

After 10 days of integration (Fig. 6.5 A and B) both model solutions are characterized by two branches of the Po plume: one extending in N-NE direction, the second, smaller, in the Eastern direction. The models produce a different WACC as the HOPS predicts a well defined coastal current with a strong horizontal gradient while the POM model appears more diffusive and the WACC is wider.

On the 20^{th} day of integration the northern branch of the Po plume in the HOPS solution (Fig. 6.5 C) has been moved against the Venice Lagoon while in the POM (Fig. 6.5 D) simulation this structure totally vanishes. The other branch disappears in both simulations as a consequence of the Bora that forced the motion in S-SW direction. Along the WACC the mesoscale eddies produced by the models have different dimensions, and the POM solution is characterized by larger scales.

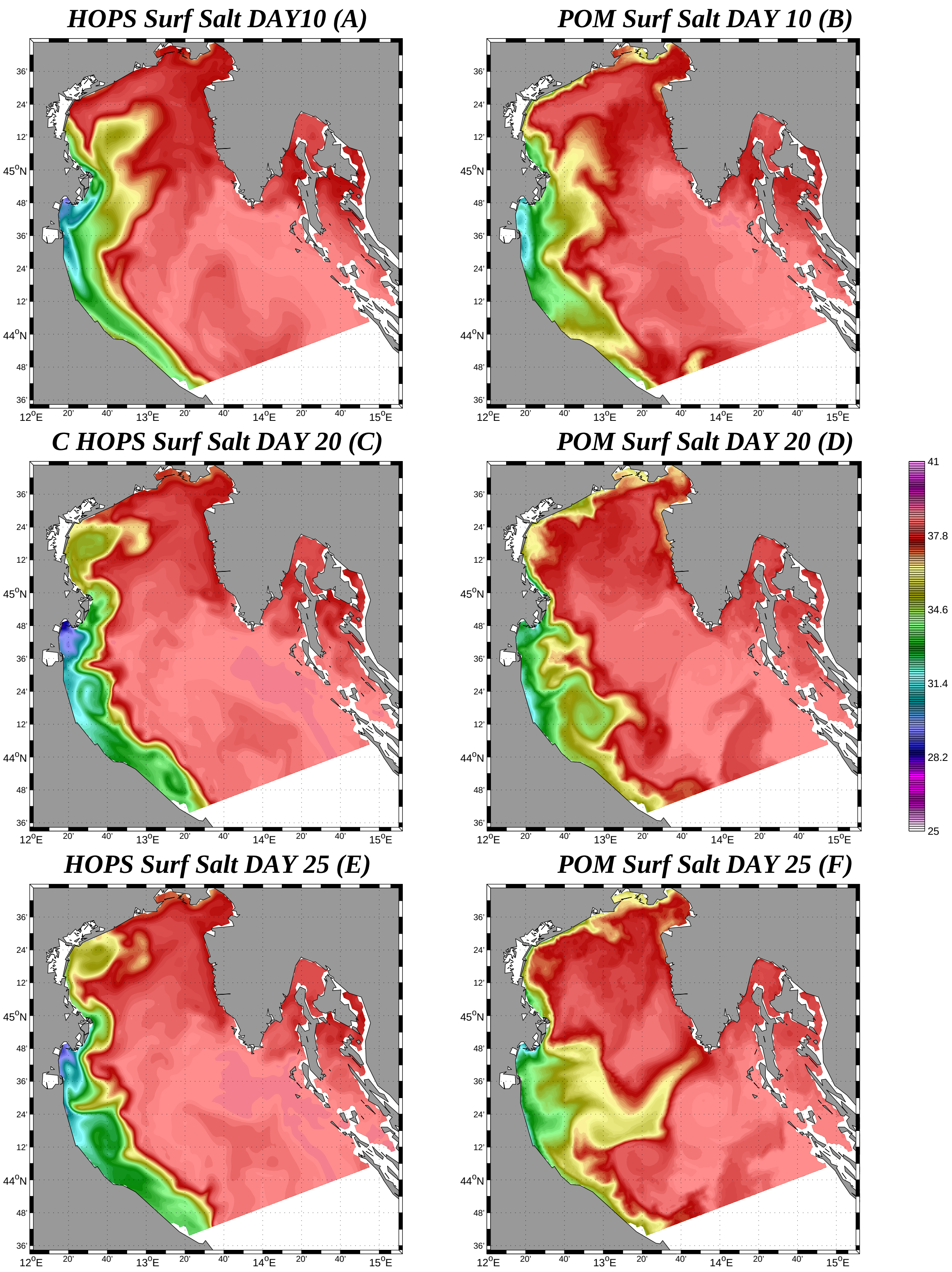

Figure 6.5 Sea surface Salinity [psu]. (A) HOPS day 10; (B) POM day 10; (C) HOPS day 20; (D) POM day 20; (E) HOPS day 25; (F) POM day 25.

Five days later the diffusive processes in POM (Fig. 6.5 F) totally destroy the small eddies along the WACC producing a larger branch extending in N-NE direction and reaching the Istrian Peninsula. HOPS (Fig. 6.5 E) simulates instead a well defined WACC.

Is interesting to note as during all the simulation the POM solution is characterized by lower salinity along the Northern coast probably, due to the different formulation used in the salinity surface boundary condition in order to parameterize the river fresh water discharge.

Once ascertained that the two models produce different solutions in terms of dynamics and values, we proceed now to a models-observation comparison and root mean square error estimation in order to establish and quantify which model is doing better.

In Fig. 6.6 temperature transects for three different days of the simulation are compared with the corresponding observations. In the first line the values of the first day are shown. The small differences between the two models are given by the different vertical discretization as the same horizontal field has been used. After 7 days of integration the two solutions are already different in values and structures. Comparing the models results with observations we note that the HOPS solution is closest to the observed values but the vertical-horizontal structure is better reproduced in the POM solution. For instance the HOPS model produces a strong gradient at the base of the WACC that is not present in both POM results and observations. On the 23rd day both model solutions seem to be affected by an excessive cooling, especially marked in POM, but the HOPS model better resolves the thermocline position with the remarkable exception on the WACC base.

In Fig. 6.7 salinity transects for four days of the simulation from models results are compared with the corresponding observations. After 3 days the observed salinity transect is characterized by a well defined WACC signal and a salinity surface maximum in the centre of the section. To have a surface salinity maximum a compensation effect from the temperature is needed otherwise an unstable density profile generates fast vertical motion restoring a stable condition. Both models capture the WACC signal but totally miss the observed salinity stratification in the middle of the section probably as a consequence of wrong predicted temperature.

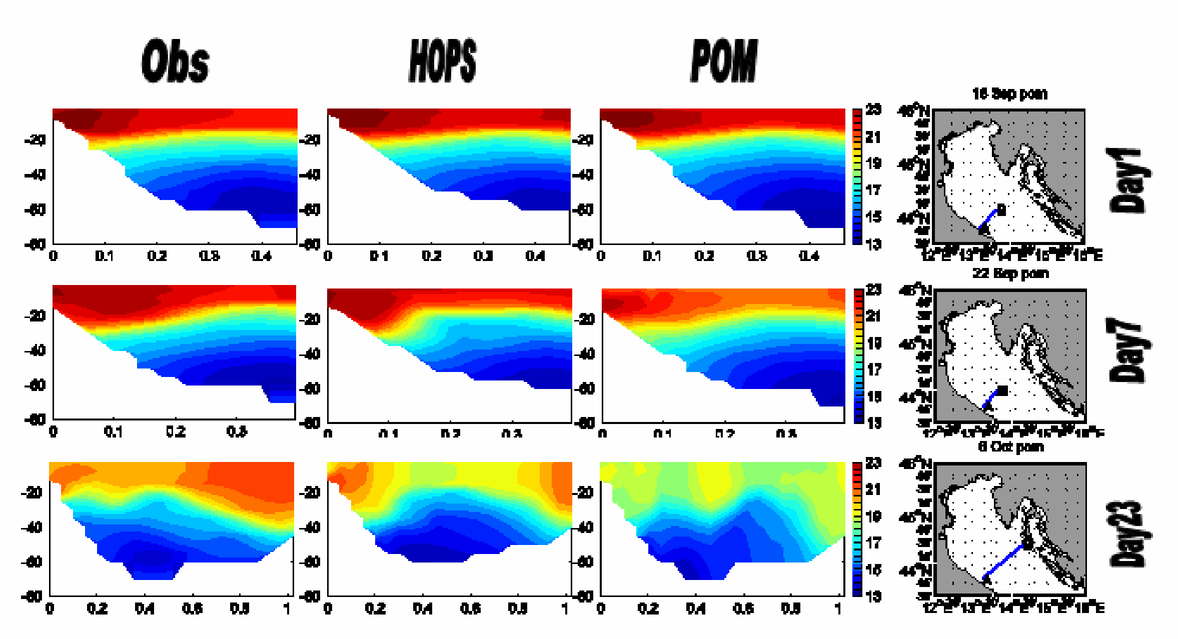

Figure 6.6 Temperature [°C] transects for the 1st, the 7th, and 23rd day of integrations. In the abscissa the distance from the first station is reported in degree, the Y axis indicates the depth in meters. The first column indicates the observation; the second column indicated the HOPS results and in the third column the POM results are reported. The location of the transects are reported in the last column.

During the others days the observations indicate a progressive freshening with an high horizontal and vertical mixing, as a consequence of the Bora event, with the only exception of a bottom salty wedge observed off-shore of the Italian coast. Both model solutions indicate an overestimation of the vertical mixing process and an underestimation of the freshening process particularly marked in the HOPS solutions.

The large differences between the predicted and observed salinity values can be traced back to the parameterization of the open boundary conditions and to the horizontal resolution of the atmospheric forcing. Using a simple Orlansky scheme no external information is used to drive the model solution also during an inflow regime and it is well known that the salinity dynamics, more than the temperature, depends on the waters that along the eastern coast are advected from the South into the area.

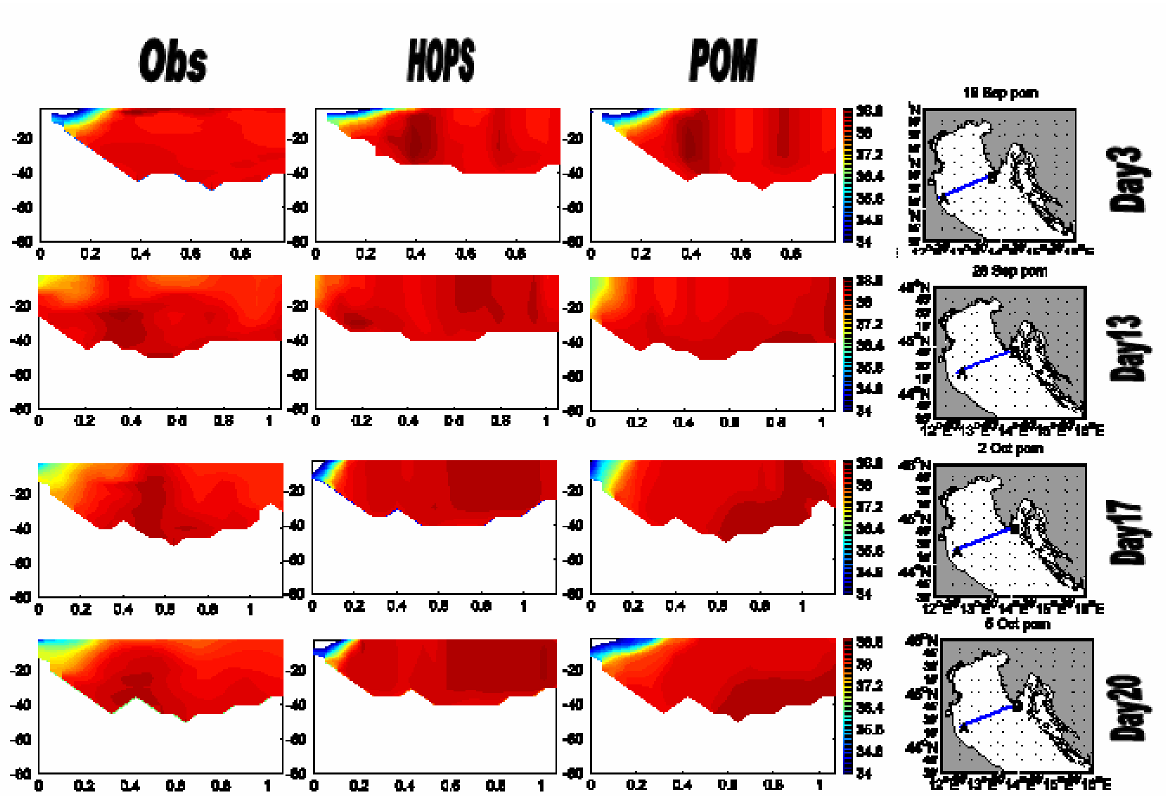

Figure 6.7 Salinity [psu] transects for the 3rd, the 13th, the 17th and 20th day of integrations. In the abscissa the distance from the first station is reported in degree, the Y axis indicates the depth in meters. The first column indicates the observation; the second column indicated the HOPS results and in the third column the POM results are reported. The location of the transects are reported in the last column.

The problem related to the coarse resolution of the atmospheric forcing derives to an inexact representation of the multiple jets structure of the Bora wind. This structure, strongly influenced by the eastern Adriatic land margin orography, produces positive and negative wind curl over the basin inducing cyclonic and

anticyclonic circulations. This peculiar circulation allows the Po plume to detach from the Italian coast reaching the interior of the basin. In the Bora field represented in the ECMWF data this horizontal variability is not well represented and the effect of the Bora is only to produce strong vertical mixing, due to the wind speed, and push the Po plume over the Italian coast.
In Fig. 6.8 the time series of the daily averaged RMS errors for temperature and salinity are shown. The temperature RMS errors (Fig. 6.8 A) show similar values for the first 10 integration days. From day 11 to day 25 the two RMS have similar trend but the POM model produces larger error probably as a consequence of the excessive cooling. The salinity errors (Fig. 6.8 B) are, instead, characterized by similar values during the whole period, with the exception of the first 10 days when the POM solution has a small RMS error.

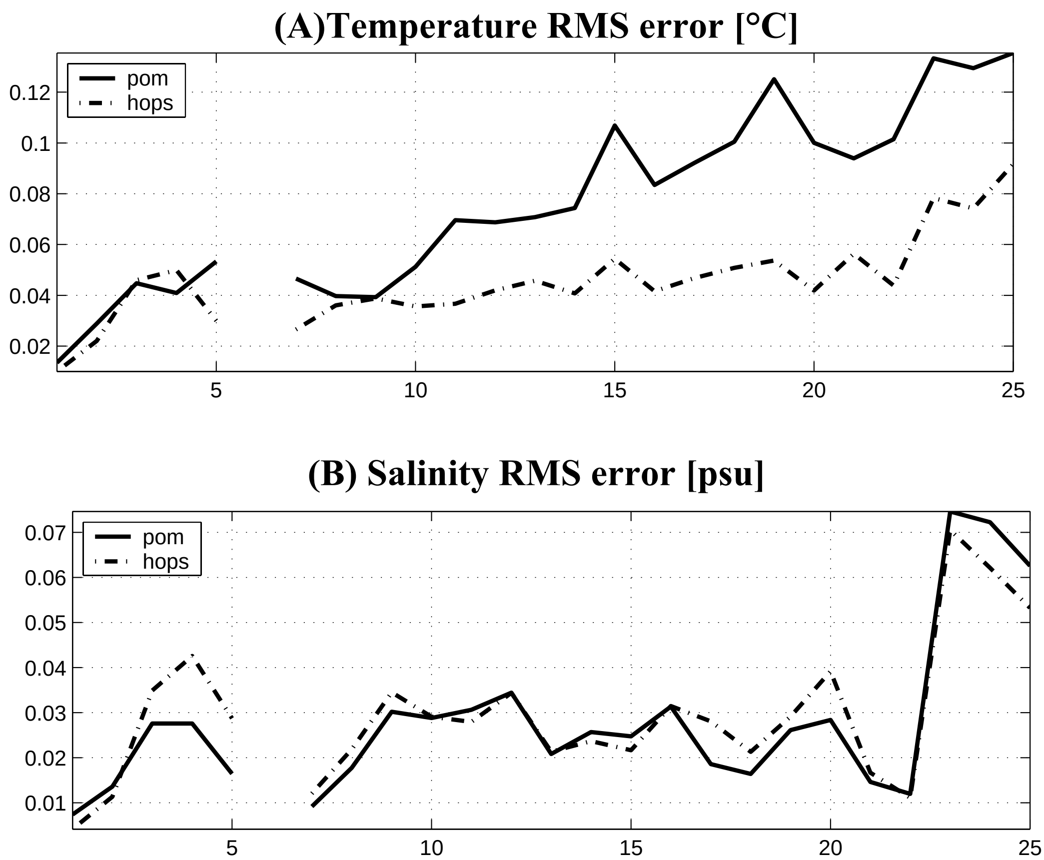

Figure 6.8 Daily averaged RMS error computed between models results and observation from CTD. The solid line indicates the POM model error, the dash line indicates the HOPS model error. In the x axis the days are reported, the y axis indicates the RMS error values. (A) RMS for temperature. (B) RMS error for salinity.

6.4 Summary and Conclusions

In this chapter the results deriving from two different high resolution models, implemented in the North Adriatic Sea, have been compared with available observations in order to understand the influence of different physical parameterizations and numerical discretization techniques on the final results.

The observed data, used for the comparison, have been collected during September-October 2002 comprising also a Bora event. This allows also the investigation of the models behavior related to strong external forcing. The major part of the simulated period was characterized by weak surface forcing and a modest Po river runoff allowing a comparison on how the total potential energy is converted to kinetic energy in the two models.

Strong differences have been traced in the models solution mostly deriving from horizontal diffusion process and vertical mixing.

The POM model is dominated by a faster motion, as a consequence of the explicit formulation of the free surface elevation, producing a large number of small mesoscale eddies. Moreover the Shapiro filter, present in the HOPS, allows a better representation of the WACC extension especially during calm forcing regimes, where the diffusion processes have a remarkable effect on the local dynamics.

It has been documented that similar surface boundary conditions produce different results. The parameterization of the heat penetration in the water column produces lower surface temperatures in the POM results respect to HOPS and observations. This is probably related to the transmission and absorption coefficients used (discussed in Chapter 2) and probably sensitivity experiments are needed.

The salinity surface boundary conditions used in POM produces better results with respect to the simple relaxation scheme adopted in HOPS, confirmed by the salinity RMS error and comparing transect along the Northern coast (not shown).

During the Bora event both model solutions are characterized by an overestimation of the vertical mixing in the interior of the basin as a consequence of the inadequate horizontal resolution of the atmospheric forcing. This indicates the necessity to use high resolution atmospheric fields as their spatial variability

more than their mean character is the main forcing for the local dynamics.
The adopted open boundary conditions adequately resolve the outflow regimes but the results confirm the necessity to use external information along the eastern coast where waters from the Southern-Middle Adriatic are advected in the area and contribute to the local dynamics.

Bibliography

Artegiani A, Azzolini R, Salusti E. On the dense water in the Adriatic Sea**.** Oceanol Acta 1989; 12: 151-160.

Artegiani A, Bregant D, Paschini E, Pinardi N, Raicich F, Russo A. The Adriatic Sea general circulation. Part I: Air sea interaction and water mass structure. J Phys Oceanogr 1997; 27: 1492-1514 a.

Artegiani A, Bregant D, Paschini E, Pinardi N, Raicich F, Russo A. The Adriatic Sea general circulation. Part II: Baroclinic circulation structure. J Phys Oceanogr 1997; 27: 1515-1532 b.

Barale V, McClain CR, Malanotte-Rizzoli P. Space and time variability of the surface color field in the Northern Adriatic Sea. J Geoph Res 1986: 91(CllI: 12957-12974.

Bergamasco A, Gacic M, Boscolo R, Umgiesser G. Winter oceanographic conditions and water mass balance in the Northern Adriatic (February 1993), J Mar Sys, 7, 67-94, 1996.

Blumberg AF, Mellor GL. A description of a three-dimensional coastal ocean circulation model. In: Heaps NS editor. Three-dimensional coastal ocean models, American Geophysical Union, Washington D.C., 1987; 208 pp.

Carter EF, Robinson AR. Analysis models for the estimation of oceanic fields. J Atmos Ocean Techn 1987; 4: 49-74.

Castellari S, Pinardi N, Leaman K. A model study of air-sea interactions in the Mediterranean Sea. J Mar Syst 1998; 18: 89-114.

Cardin V, Gacic M. Long Term heat flux variability and winter convection in the Adriatic Sea. J Geophys Res 2003; 108: NO C9.

Chapman DC. Numerical treatment of cross-shelf open boundaries in a barotropic coastal ocean model. Journal of Physical Oceanography 1985; 15: 1060-1075.

Chiggiato J, Zavatarelli M, Deserti M, Castellari S. Comparison of Adriatic Sea surface fluxes estimated from different operational models data sets and local observations (1998-2001). Sci Total Environ (in press).

Demirov E, Pinardi N. Simulation of the Mediterranean Sea circulation from 1979 to 1993: Part I. The interannual variability. J Mar Syst 2002; 33-34: 23-50.

Demirov E, Pinardi N, Fratianni C, Tonani M, Giacomelli L, De Mey P. Assimilation scheme of the Mediterranean Forecasting system: operational implementation. Ann Geophysicae 2003; 21: 189-204.

Flather RA. A tidal model of the northwest European continental shelf. Memories de la Societe Royale des Sciences de Liege 1976; 6(10):141-164.

Franco P. L'Adriatico Settentrionale caratteri oceanografici e problemi. 5" Congresso della Associazione Italiana di oceanografia e limnologia, Stresa 1983: l-27 pp.

Gacic M, Hopkins TS, Lascaratos A. Aspects of the response of the Mediterranean Sea to long-term trends in atmospheric forcing. In: L. Jeftic, J.D. Milliman and G. Sestini (Editors), Climatic Change and the Mediterranean 1992: 233-244 pp.

Grezio A, Pinardi N. Data assimilation of CTD and XBT in the Adriatic

Regional Model. Acta Adriatica. submitted. 2005

Hellerman S, Rosenstein M. Normal monthly wind stress over the world ocean with error estimates. J Phys Oceanogr 1983; 13: 1093-1104.

Hendershott MC, Rizzoli P. The winter circulation of the Adriatic sea. Deep-Sea Res. 1976: 23: 353-373.

Jerlov NG. Marine Optics. Elsevier Sci, New York, 1976; 231 pp.

Klein B, Roether W, Manca BB, Bregnat D, Beitzel V, Kovacevic V, Luchetta A. The large deep water transient in the Eastern Mediterranean. Deep-Sea Res 1999; 1. 46: 371-414.

Kondo J. Air-sea bulk transfer coefficients in diabatic conditions. Boundary Layer Mteteorol 1975; 9: 91-112.

Kovacevic V, Gacic M, Paulain P. Eulerian current measurements in the Strait of Otranto and in the Southern Adriatic. J Mar Syst 1999; 20: 255-278.

Lascaratos A, Gacic M. Low-frequency sea level variability in the Northeastern Mediterranean. J Phys Oceanogr 1990; 20: 522-533.

Legates DR, Wilmott CJ. Mean seasonal and spatial variability in a gauge corrected global precipitation. Int J Climatol 1990; 10: 121-127.

Maggiore A, Zavatarelli M, Angelucci MG, Pinardi N. Surface Heat and water fluxes in the Adriatic Sea: Seasonal and interannual variability. Phys Chem Earth 1998; 23: 561-567.

Malanotte Rizzoli P. The northern Adriatic Sea as a prototype of convection and water mass formation on the continental shelf. In: Chu PC, Gascard JP, editors. Deep convection and deep water formation in the Oceans, Elsevier Oceanography Series 1991; 57: 229-239.

Malanotte-Rizzoli P, Bergamasco A. The dynamics of coastal region of the Northen Adriatic Sea. J. Phys. Oceanogr. 1983: 13: 1105-1130.

Manca BB, Kovacevic V, Gacic M, Viezzoli D. Dense water formation in the Southern Adriatic Sea and spreading into the Ionian Sea in the period 1997-1999. J Mar Syst 2002; 33-34: 133-154.

Marchesiello P, McWilliams JC, Shchepetkin A. Open boundary conditions for long term integration of regional oceanic models. Ocean Modelling 2001; 3: 1-20.

Masina S, Pinardi N. Mesoscale data assimilation studies in the middle Adriatic Sea. Continental Shelf Research 1994: 14, No. 12: 1293-1310,

May PW. A brief explanation of Mediterranean heat and momentum flux calculations. NORDA Code 322, Nav Oceanogr Atmos Res Lab, Stennis Space Center, Miss, 1986; 5 pp.

Mellor GL. An equation of state for numerical models of ocean and estuaries. J Atmos Ocean Tech 1991; 8: 609-611.

Mellor GL, Yamada T. Development of a turbulence closure submodel for geophysical fluid problems. Rev Geophys Space Phys 1982; 20: 851-875.

Mellor GL, Blumberg AF. Modeling vertical and horizontal diffusivities with the sigma coordinate ocean models. Mon Weather Rev 1985; 113: 1379-1383.

Miyakoda K, Rosati A. One-way nested grid models: The interface conditions and the numerical accuracy. Monthly Weather Review 1977; 105(9): 1092-1107.

Oddo P, Pinardi N, Zavatarelli M. A numerical study of the interannual variability of the Adriatic Sea (2000-2002). Science of Total Environment, 2005 (in press)

Orlansky I. A simple boundary condition for unbounded hyperbolic flows. Journal of Computational Physics 1976; 21:251-269.

Orlic M. Salinity of the North Adriatic. A fresh look at some old data. Bollettino di oceanografia teorica ed applicata. 1989;7:219-228.

Orlic M, Kuzmic M, Pasaric Z. Response of the Adriatic Sea to the Bora and Sirocco forcing. Cont Shelf Res 1994; 14: 91-116.

Orlic M, Gacic M, La Violette P. The currents and circulation of the Adriatic Sea. Oceanol Acta 1992; 15: 109-124.

Ovchinnikov IM, Zats VI, Krivoskeya VG, Nemirosky MS, Udodov AI. Winter convection in the Adriatic and formation of deep eastern Mediterranean waters. Ann Geophysicae 1997; 5B: 89-92.

Pacanowsky RC, Philander SGH. Parameterization of vertical mixing in numerical models of tropical oceans. J Phys Oceanog 1981: 11, 1443-1451.

Beg Paklar G, Isakov V, Koracin D, Kourafalou V, Orlic M. A case study of bora-driven flow and density changes on the Adriatic Shelf (January 1987). Continental Shelf Research 2001; 21, 1751-1783.

Palma ED, Matano RP. On the implementation of passive open boundary conditions for a general circulation model: the barotropic mode. J Geophys Res

1998; 103: 1319-1341.

Palma ED, Matano RP. On the implementation of open boundary conditions for a general circulation model: the three-dimensional case. J Geophys Res 2000; 105: 8605-8628.

Peixoto JP, Oort AH. Physics of Climate. American Institute of Physics 1992; 520 pp.

Pinardi N, Rosati A, Pacanowski RC. The sea surface pressare formulation of rigid li d models. Implications for altimetric data assimilation studies. J Mar Sys 1995; 6: 109-119

Pinardi N, Auclair F, Cesarini C, Demirov E, Fonda Umani S, Giani M, Montanari G, Oddo P, Tonani M, Zavatarelli M. Toward Marine Environmental Predictions in the Mediterranean Sea Coastal Areas: A Monitoring Approach. Pinardi N, Woods J, editors. Ocean Forecasting, Springer-Verlag, 2002; 339-376 pp.

Pinardi N, Allen I, Demirov E, De Mey P, Korres G, Lascaratos A, Traon PY, Maillard C, Manzella G, Tziavos C. The Mediterranean ocean forecasting system: first phase of implementation (1998-2001). Ann Geophysicae 2003; 21: 3-20.

Poulain MP. Adriatic Sea surface circulation as derived from drifter data between 1990 and 1999. J Mar Syst 2001; 29: 3-32.

Provini A, Crosa G, Marchetti R. Nutrient export from the Po and Adige river basin over the last 20 years. Sci Total Environ 1992; suppl.: 291-313.

Pullen J, Doyle JD, Hodur R, Ogston A, Book WJ, Perkins H, Signell R.

Coupled ocean-atmosphere nested modeling of the Adriatic Sea during winter and spring 2001. J Geophys Res 2003; 108 (C10), 3320.

Raicich F. Note on flow rates of the Adriatic rivers, Istituto Talassografico Sperimentale Trieste. Technical Report 1994; RF02: 94, 8.

Raicich F. On fresh water balance of the Adriatic Sea. J Mar Syst 1996; 9: 305-319.

Raymond WH, Kuo HL. A radiation boundary condition for multidimensional flows. Quarterly Journal of the Royal Metereological Society 1984; 110: 535-551.

Reed RK. An evaluation of formulas for estimating clear sky insulation over the ocean. NOAA-ERL 352-PMEL Technical Report 1975; 26: 25.

Reed RK. On estimating insolation over the ocean. J Phys Oceanogr 1977; 1: 854-871.

Robinson AR. Physical Processes, Field Estimation and Interdisciplinary Ocean Modeling, Earth-Science Reviews 1996 :40, 3–54

Robinson AR. Forecasting and simulating coastal ocean processes and variabilities with the Harvard Ocean Prediction System. Coastal Ocean Prediction (C.N.K. Mooers, ed.) AGU Coastal and Estuarine Studies Series, American Geophysical Union 1999: 77-100,

Robinson AR, Theocharis A, Lascaratos A, Leslie WG. Mediterranean Sea Circulation. Encyclopedia of Ocean Sciences. Academic Press Ltd., London, 2001: 1689-1706

Roether W, Manca BB, Klein B, Bregant D, Georgopoulos D, Beitzel V, Kovacevic V, Luchetta A. Recent changes in Eastern Mediterranean deep waters. Science 1996; 271: 333-335.

Sannino GTM, Bargagli A, Artale V. Numerical Modelling of the mean exchange through the Strait of Gibraltar. J Geophys Res 2002; 107: (C8), 10 1029-2001JC000929.

Santoleri R, Marullo S, Bohm E. An objective analysis scheme for AVHRR imagery. Int J Remote Sensing 1991; 12, No 4: 681-693

Shapiro R. Smoothing, filtering, and boundary effects. *Rev. Geophys. Space Phys* (1970): 8, 359–387.

Shaw PT, Csanady GT. Self advection of density perturbations on a sloping continental shelf. J Phys Ocean 1983; 13: 769-782.

Smagorinsky J. Some historical remarks on the use of nonlinear viscosities. In: Galperin B, Orszag SA, editors. Large eddy simulations of complex engineering and geophysical flows. Cambrige Univ. Press, New York, 1993; 3-36

Smolarkiewicz PK. A fully multidimensional positive definite advection transport algorithm with small implicit diffusion. J Comput Phys 1984; 54: 325-362.

Sommerfield A. Partial differential equations. Lecture Notes on Theoretical Physics. Academic Press. San Diego CA 1949: vol 6.

Spall MA, Robinson AR. A new open ocean, hybrid coordinate primitive equations model. Mathematics and Computer in Simulations 1989; 31: 241-269

Sturm B, Kuzmic M, Orlic M. An evaluation and interpretaion of CZCS-derived patterns on the Adriatic shelf. Oceanol. Acta 1992: 15: 13-23.

Supic N, Orlic M, Degobbis D. Istrian Coastal Countercurrent and its Year-to-Year Variability. Estuar Coast Shelf S 2000; 51: 385-397.

Vilibic L. An analysis of dense water production on the North Adriatic shelf. Estuar Coast Shelf S 2003; 56: 697-707.

Woods AW, Beardsley RC. On the barotropic discharge of a homogeneous fluid onto a continental shelf. Continental Shelf Research (1988); 8: 307–327.

Zavatarelli M, Pinardi N, Kourafalou VH, Maggiore A. Diagnostic and prognostic model studies of the Adriatic Sea circulation. Seasonal variability. J Geophys Res 2002; 107(C1), art 3004.

Zavatarelli M, Pinardi N. The Adriatic Sea Modelling System: a nested Approach. Ann Geophysicae 2003; 21: 345-364.

Zore-Armanda M, Gacic M. Effects of bora on the circulation in the North Adriatic. Ann. Geophys. 1987: 5B: 93-102.